LA-SUB--93-207

[redacted]

Los Alamos National Laboratory

for the Project:
"Investigations of Large Area Electron Beam Diodes for Excimer Lasers"
(Subcontract No. 9-X60-E9581-1)

Project Director:
Professor Ronald M. Gilgenbach
Intense Energy Beam Interaction Laboratory
Nuclear Engineering Department
University of Michigan
Ann Arbor, MI 48109-2104

9-X60-E9581-1

DISCLAIMER

This report was prepared as an account of work sponsored by an agency of the United States Government. Neither the United States Government nor any agency thereof, nor any of their employees, makes any warranty, express or implied, or assumes any legal liability or responsibility for the accuracy, completeness, or usefulness of any information, apparatus, product, or process disclosed, or represents that its use would not infringe privately owned rights. Reference herein to any specific commercial product, process, or service by trade name, trademark, manufacturer, or otherwise does not necessarily constitute or imply its endorsement, recommendation, or favoring by the United States Government or any agency thereof. The views and opinions of authors expressed herein do not necessarily state or reflect those of the United States Government or any agency thereof.

RECEIVED
JAN 27 1994
OSTI

MASTER

DISTRIBUTION OF THIS DOCUMENT IS UNLIMITED

Table of Contents Page

1.0 Abstract 3

2.0 Experimental Research Objectives 4

3.0 Experimental Configuration and Diagnostics 5

4.0 Effects of Gradient and Uniform Magnetic Fields on Diode Closure 7

5.0 Cathode Research and Development 12

6.0 CO2 Laser and Helium Neon Laser Deflection as a Diagnostic of Microsecond Electron Beam Diode Closure 14

7.0 X-Ray Emission as a Voltage Diagnostic for Microsecond e-Beam Diodes 32

8.0 Electric Stress in Microsecond Electron Beam Diodes 34

Figures 36

Appendix A: Reprints of Publications Related to this Project A.1

A.1 Measurement of Long-Pulse Relativistic Electron Beam Perpendicular to Parallel Velocity Ratio by Cerenkov Emission and Radiation Darkening on a Glass Plate A.1

A.2 Dynamics of Excimer Laser Ablated Aluminum Neutral Atom Plume Measured by Dye Laser Resonance Absorption Photography A.24

Appendix B. Personnel Involved in This Project B.1

1.0 Abstract

This report summarizes the results of a one year research program at the University of Michigan to investigate the physics and technology of microsecond electron beam diodes. These experiments were performed on the Michigan Electron Long Beam Accelerator (MELBA) at parameters: Voltage = -0.65 to -0.9 MV, current = 1-50 kA, and pulselength=0.5- 5 microseconds.

Major accomplishments include:

1) the first two-wavelength (CO2 and HeNe) laser deflection measurements of diode plasma and neutrals,
2) Measurements of the effects on magnetic field gradient on microsecond diode closure,
3) demonstration of good fidelity of processed x-ray signals as a diagnostic of beam voltage,
4) Extended-pulselength scaling of electron beam diode arcing and diode closure, and
5) Innovative Cerenkov plate diagnostics of e-beam dynamics.

2.0 Experimental research objectives

The objectives of this research were to investigate crucial physics and technology issues concerning long-pulse electron beam diodes. This encompassed electron beam diode closure as well as new techniques for diagnosing and studying diode closure. These objectives are summarized in Table 2-1.

It should be noted that in a single year we accomplished nearly all the goals listed. We successfully demonstrated simultaneous CO2 and helium neon laser deflection measurements as an unambiguous diagnostic of both plasma and neutral particle dynamics in long-pulse electron beam diodes. We studied the effects of magnetic field gradients on long-pulse electron beam diode closure and compared to uniform magnetic fields. A new cathode was developed that generated 5 microsecond electron beams. A demonstration was made that X-rays from an e-beam diode are an effective means of measuring the cathode voltage. Electric stress criteria were extended by the multimicrosecond pulses from the MELBA machine. We demonstrated that Cerenkov plates are an effective diagnostic. These accomplishments are presented in this report.

Table 2-1. UM Experimental Research Objectives

diode plasma closure studies: direct measurements of diode plasma

- helium neon laser diagnostic measurements of cathode and anode plasma
- CO2 laser deflection system: development and MELBA measurements

diode diagnostic research, development, and analysis

- investigate X-ray diagnostics/ analysis for measurements of e-beam diode voltage
- electrical diagnostics: analysis of diode perveance data to obtain closure velocities
- explore new dye laser diagnostics of diodes

cathode development

- profiled velvet cathode
- large area toroidal cathode

electrical breakdown in μs e-beam diodes

- obtain scaling data on arcing/ shorting times to extend parameter range beyond McGeoch criterion

3.0 Experimental Configuration and Diagnostics

The experimental configuration for the MELBA diode closure experiments is presented in Figure 3-1. Three cathodes were employed in these experiments, as depicted in Figure 3-2. The first, a planar cathode "A" was used for most of the experiments reported here. An important feature of this cathode was the shielded guard ring which covered the edge of the velvet. A second cathode "B" was developed during this research, as shown in Figure 3-2. Cathode B was a quasi-Chang profile on the end of a hemispherical cathode stalk. The third cathode "C" was utilized briefly as a large area cathode which was designed to have minimal edge emission enhancement.

The MELBA machine was employed for these experiments with parameters as given in Table 3-1. LANL felt was employed for nearly all of these experiments.

Table 3-1. UM MELBA Experimental Parameters

Cathode voltage: -0.65 to -0.9 MV

e-beam pulselength: 0.5-5 μs

A-K gap spacing: 6-10.3 cm

Cathode electric field: ~ 70-110 kV/cm

diode current: 1 to 50 kA

apertured e-beam current: 20-40 A, (J=~15-30 A/cm2)

magnetic field = 600-800 G

A wide range of diagnostics were developed and utilized in these experiments. These diagnostics are summarized in Table 3-2. These experiments represented the first simultaneous 2-wavelength measurements of diode plasma and neutrals. The CO2 laser deflection diagnostic was found to have the advantage that the long wavelength made it ideal for measurements of diode plasmas. In combination with the helium neon laser the CO2 laser made it possible for the first time to distinguish between cathode plasma and neutrals. This will be discussed in further detail in the following sections.

Table 3-2. Diode diagnostics developed and utilized

* beam voltage

* cathode stalk current

* anode current

* apertured anode current collector

- cathode plasma and neutrals; CO2 and HeNe laser deflection

* Cerenkov emission measured to characterize e-beams; also utilized radiation darkening of glass in single shot

- large area Cerenkov plate for e-beam uniformity

- small area Cerenkov plate for e-beam velocity ratio $\alpha = v_{\perp}/v_{||}$

* X-rays; scintillator, fiberoptic, PM tube in Faraday cage

* diode optical emission; fiberoptic bundle, PM tube in Faraday cage

4.0 Effects of Gradient and Uniform Magnetic Fields on Diode Closure

Diode closure experiments were performed for three cases:
1) Gradient magnetic field (25% gradient)
2) Uniform magnetic field, and
3) Unmagnetized case.

The MELBA generator could be operated in either a crowbarred mode or a non-crowbarred mode. Figures 4.1 - 4.3 show the voltage and current traces (non-crowbarred shots) for the three magnetic field cases for cathode A: Figure 4.1 shows the gradient magnetic field (shot M1850); Figure 4.2 shows the uniform magnetic field (shot m1852); and Figure 4.3 shows the unmagnetized case (shot M1851). The results of these experiments are discussed below in terms of the Child-Langmuir modeling of the perveance. The crucial factor in these experiments is the edge emisssion which is determined experimentally by the anode current to the wall current.

If the radial/edge effect is to be neglected then we expect the diode current (which is a measure of the total current) would follow the C-L planar model as does the anode current . This implies that the ratio of anode to diode current be essentially one. In the cathode A data, this is not the case as shown in Table 4.1. Thus it was concluded that radial/edge effects may indeed be large for cathode A, and the analysis presented below suggest that this is indeed the case.

Table 4-1
Ratios of Anode to Diode current for the cathode A Data

Case	Peak I_A/I_D
Gradient B (M1850)	58%
Uniform B (M1852)	44%
Unmagnetized (M1851)	30%

The models employed in the analysis are:
a) radial model
b) planar model
c) total model

A brief description of each follows:

a) Radial Model

Using the radial non-relativistic Child -Langmuir (C-L) equation (see Bob Parker's thesis, and J. Appl. Phys. 45, no. 6, 1974) as in the J. Coogan handout,

$$I = (1.83 \times 10^{-6}) \frac{2\pi r_0}{d_0 \alpha^2} V^{\frac{3}{2}}$$

with I in amps, V in volts, d_0 in cm and r_0 in cm which implies the perveance for the radial case, P_r, is

$$P_r = (11.498 \times 10^{-6}) \frac{r_0}{d_0 \alpha^2}$$

where,

r_0 is the cathode plasma radius;

d_0 is the initial AK gap spacing (shortest distance to anode);

α is the 'geometric edge factor' given by (for a planar cathode),

$$\alpha = \ln\left(\frac{d_0}{vt}\right) - \frac{2}{5}\left(\ln\left(\frac{d_0}{vt}\right)\right)^2 + \frac{11}{120}\left(\ln\left(\frac{d_0}{vt}\right)\right)^3 - \frac{47}{3300}\left(\ln\left(\frac{d_0}{vt}\right)\right)^4$$

where,

v is the closure velocity;

$t = t_1 - t_0$ is time with t_0 being the initial time.

b) Planar Model

Using the planar non-relativistic C-L equation (see R. B. Miller's book),

$$I = (2.34 \times 10^{-6}) \frac{A_{eff}}{d^2} V^{\frac{3}{2}}$$

with I in amps, V in volts, d in cm, and A_{eff} in cm^2, gives the perveance, P_p,

$$P_p = (2.34 \times 10^{-6}) \frac{\pi r_0^2}{d^2}$$

assuming a uniform area, A_{eff}, approximately equal to πr_0^2, where,

r_0 = cathode plasma radius (in cm);

$d = d_0 - v(t_1 - t_0)$, d_0 = initial AK gap spacing;

v = closure velocity;

t = time, t_0 = initial starting time.

Thus, for comparison (as J. Coogan does), the expected $d = d_0 - vt$ (with a given closure velocity) can be plotted with the d obtained from the measured planar perveance,

$$d = \sqrt{\frac{(2.34 \times 10^{-6}) A_{eff}}{P_p}}$$

Note that using the AK gap comparisons (d from P_p) will always give a straight line slope with the initial AK gap, d_0, at $t=t_0$ (from $d=d_0-vt$) as the y-intercept.

c) Total Model

Assume that the total perveance is just a linear combination of the planar and radial models such that,

$$P_{total} = P_p + P_r.$$

A comparison of the three currents (diode, anode, and wall) using the above models is needed in order to show if the radial/edge effect is large. The comparisons are made in the following way:

1) Total (diode) current with total (including 'edge' effects) perveance.

2) Anode current with planar C-L model.

3) 'Wall' (anode subtracted from diode) current with radial C-L model.

The comparisons are applied as follows:

a) For a non B-field case, we expect that the anode current (measured) will be mostly composed of the planar emission (axial) closure, in which a straight line slope will be given for the measured experimental values lying in the C-L region since,

$$d \propto \sqrt{\frac{1}{P_p}}$$

is linear.

By choosing a diode closure velocity and plotting $d = d_0-vt$ superimposed on

$$d = \sqrt{\frac{(2.34 \times 10^{-6}) A_{eff}}{P_p}}$$

and adjusting r_0 (the cathode plasma radius, which only changes the y-intercept), we can match the two lines in the C-L regime (manipulating both the velocity and r_0 may have to be done several times to obtain the 'best fit'). Also plotting $(1/P_p)^{1/2}$ for both theoretical and measured P_p by manipulating the closure velocity and the cathode plasma radius should give the same answer.

b) Also for the non B-field case, we expect the 'wall' current (measured) to be mostly due to radial emission closure. Due to the $(1/\alpha)^2$ function, we cannot expect to find a linear relationship as for the planar case. But one can still plot $(1/P)^{1/2}$ for the radial measurement (from the 'wall' current) and compare with $(1/P_r)^{1/2}$ from the radial C-L prediction. Again, as for the planar case, a best fit is found by manipulating both the velocity and the cathode plasma radius.

c) We expect the diode current (measured) to contain the total effects, radial and planar emission, so a best fit is found by comparing the meaured $(1/P)^{1/2}$ (from diode current) to the predicted $(1/P_{total})^{1/2}$. Again, the manipulation of the velocity and cathode plasma radius is used to find the best fit .

The results for the three magnetic field cases for cathode A are shown in table 4-2. As shown in table 4-2, the gradient field case has the slowest closure velocity , 4.2 cm/μs, the unmagnetized case has 4.4 cm/μs, and the uniform field case has the fastest closure velocity at 5.0 cm/μs. Note that the closure velocity does not depend on the comparison of the current (diode, anode, wall) to the model (total, planar, radial); only the effective radius (effective area) depends on the model and current used. Examples of the fit are shown in figures 4-5 through 4-10.

Notice also the differences in the effective radius (in table 4-2) given by the three models. The anode/planar comparison show large values of the effective radius suggesting edge/radial effects are present for cathode A. The 'wall'/radial comparison gives an idea as to how large an effect the edge/radial emission is on the analysis. A smaller effective radius implies more delivered current from the diode to the anode (as observed experimentally), but not necessarily a negligible effect on the closure velocities. The diode current incorporates the total effects thus should give the best measure of r_{eff}.

In using the diode current model (including 'edge' and radial effects), one can see the effect of the axial magnetic field on the cathode plasma radius. Recall that the radius of the carbon felt is 3.8 cm, and that the radius of the total cathode (the corona ring, spacing rings, and stalk itself) is 7.0 cm. As shown in table 4-2 the uniform field gives the smallest r_{eff} at 4.7 cm, the gradient gives 5.75 cm, and the unmagnetized case gives the largest r_{eff} of 7.0 cm. Note that in the unmagnetized case, r_{eff} matches that of the total

radius of the cathode stalk, thus suggesting that 'edge' emissions do play a role in the cathode A planar experimental setup. The magnetized cases, gradient and uniform, have r_{eff} larger than the carbon felt radius also suggesting that there is 'edge' emission, but the applied magnetic field has a definite effect on the 'edge' plasma electron motions. Figure 4-4 has an example of what the two field cases look like (note that the figure does not necessarily represent the exact field lines nor the dimensions of the experimental setup for the above shots).

Table 4-2
Closure Velocity and 'Effective' Radius for cathode A

Using Diode Current and 'Total' Model

Shot#	Closure Velocity (cm/μs)	r_{eff} (cm)
M1850 (Gradient)	4.2	5.75
M1851 (No Field)	4.4	7.0
M1852 (Uniform)	5.0	4.7

Using Anode Current and Planar Model

Shot#	Closure Velocity (cm/μs)	r_{eff} (cm)
M1850 (Gradient)	4.2	6.2
M1851 (No Field)	4.4	7.0
M1852 (Uniform)	5.0	6.9

Using 'Wall' Current and Radial Model

Shot#	Closure Velocity (cm/μs)	r_{eff} (cm)
M1850 (Gradient)	4.2	5.0
M1851 (No Field)	4.4	7.0
M1852 (Uniform)	5.0	2.75

5.0 Cathode Research and Development

A new cathode (B) was developed in order to reduce radial diode closure effects observed on the previous cathode design (A), which had a relatively large edge enhancement due to a small-radius edge. The new cathode design utilized an existing hemispherical-end (HE) cathode stalk, which was not previously employed in the LANL diode experiments. The hemispherical-end cathode was initially fabricated as a non-emitting stalk for resistive load testing of MELBA. With fresh anodization this stalk was previously operated up to the full 1 MV MELBA voltage over several microseconds without significant electron emission. Subsequently a hole was drilled and tapped in the hemispherical end of this cathode. In order to minimize edge emission and radial diode closure a quasi-Chang profile form was fabricated by scaling down the radius of the cathode utilized on EGUN test facility. The aluminum cathode form was covered by velvet, and screwed onto the large (HE) stalk (Figure 5-1). This made it possible to stretch the fabric around between the two sections, so that the edges were hidden. Edge emission was greatly reduced by the resultant cathode shape.

Cathode modeling is depicted in figures 5-2, 5-3, and 5-4, which show the electron beam trajectories calculated by the Hermannsfeldt code for uniform magnetic field, gradient magnetic field, and unmagnetized cases, respectively. It can be seen that the electron flow is extremely well focused, especially in the gradient magnetic field case. This agrees with the experiments discussed below.

Experiments were performed on cathode B for three cases: Gradient magnetic field, uniform B field and unmagnetized for an A-K gap of 12 cm. Radial emission was diagnosed by three techniques: first by measurement and comparison of anode and diode currents, and second, by placing X-ray film under the lead shielding which covers the diode chamber (suggested by Lou Rosocha). The third diagnostic for radial emission was an x-ray scinitillator (located on the outside wall of the diode chamber), fiberoptic coupled to a photomultiplier tube in the Faraday cage.

Experimental results were striking. In the magnetic field gradient, we measured smooth electron beam pulselength of 4.5-5 microseconds before shorting, (Figure 5-5), yielding an effective closure velocity of 2.4 cm/μs and a perveance closure velocity of 2.3 cm/μs. Uniform magnetic field cases gave similarly long, smooth pulselengths (Figure 5-6) and a perveance closure velocity of about 2.4 cm/μs. The unmagnetized diode gave only 3 μs pulselength (Figure 5-7), indicating an effective closure velocity of 4 cm/ μs and a perveance closure velocity of 3-3.8 cm/μs. Data analysis of perveance-closure velocities is given in Figures 5-8, 5-9, and 5-10 for the same shots for each case. It should be noted these

closure velocities fit the planar Child-Langmuir model almost perfectly without including radial/edge emission. Cathode B closure velocities are summarized in Figure 5-11. Also, note that the uniform magnetic field had a slight gradient due to the large A-K gap in these experiments.

X-ray measurements showed that the radial electron emission from cathode B was lower than the old cathode A. As expected, we observed slightly greater radial emission of electrons for the unmagnetized case compared to the magnetized cases. The current measurements showed that the ratio of anode to diode current was increased (radial current decreased) as summarized in Table 5-1. Anode (axial) current is almost 100% of diode current (~zero radial current) for gradient magnetic fields. Note that the A-K gap was almost equal to the radial gap, so significant increase in the anode/diode current ratio(decreases in radial current) can be achieved in our new cathode designs with smaller A-K gaps.

The most remarkable results obtained were the long-flat voltage pulses obtained for cathode B. Figure 5-12 shows that the diode power was almost flat at 4 GW for 4 microseconds yielding a delivered e-beam energy of about 16 kJ in a small spot. The increase in delivered electron beam energy was demonstrated by the damage to the graphite anode plate (1/8 inch thick) which was severely cracked and broken by the electron beam during this run.

Table 5-1
Ratios of Anode current to diode current for first experiment on the new cathode B.

Case	peak I_A/I_D	average I_A/I_D
Gradient B	99%	85%
uniform B	100%	70%
unmagnetized	68%	56%

Another cathode "C" was developed in order to provide large area with minimal edge emissions. This cathode is depicted in Figure 5-13. It consists of a toroid /plate with the flat side of the plate covered with graphite felt. Figure 5-14 shows the E-Gun code modeling of cathode C. It can be seen that the edge enhancement of the electric field is very low. Since we were not able to shield the edge of the felt in initial experiments, the results has evidence of arcing. Time constraints prevented us from giving the cathode the required edge shielding.

6.0 CO2 Laser and Helium Neon Laser Deflection as a Diagnostic of Microsecond Electron Beam Diode Closure

Extensive laser deflection experiments using a helium neon laser to detect cathode plasma and neutrals indicated that the HeNe wavelength was too short to measure electron density gradients in long-pulse e-beam diodes. In order to obtain improved sensitivity a CO2 laser was built for use with an existing fast infrared detector. At the CO2 laser wavelength of 10.6 microns the deflection from a plasma density gradient will be 290 times as great as that at the HeNe wavelength of 0.62 microns. The deflection from a neutral gas density gradient will be nearly the same at both wavelengths.

The CO2 laser was fabricated from a 1 inch glass tube, 1 meter long, surrounded by a concentric water jacket for cooling. The ends of the tube consist of salt windows oriented at Brewster's angle. A mixture of 10% N2, 10% CO2 and 80% helium is flowed through the tube at a pressure of 8 Torr. A 15 mA pink discharge is maintained between electrodes at opposite ends of the tube using a 5000 volt full-wave rectified, unfiltered power supply through a 25 kiloohm ballast resistor.

The end mirror is a fully reflecting copper mirror with a 10 meter radius of curvature. The output mirror is a 65% reflecting germanium mirror, coated for antireflectance on the output side. This mirror system gives a fundamental radial mode with 6 mm diameter. An adjustable aperture within the laser cavity allows selection of this mode. Lasing at 10.6 microns produces a power density of 3-10W/cm2 in a spot of 6 mm diameter, for a total output power of 1-3 Watts. The calculated divergence of the beam is 2.6 X 10^{-3} radians, giving a 5 cm spot after 20 meters of propagation; observations confirm this value.

A Raytheon IR101 PbSnTe liquid nitrogen cooled detector coupled to a Raytheon DA-20 preamplifier provides high speed measurement of the laser signal. The detector has a responsivity of 20-60 V/W; the preamplifier amplifies this by 10,000 and can drive 50 ohms. The CO2 laser signal is passed through the diode and imaged on a knifedge before entering the detector in the Faraday cage.

Results of these experiments are described in detail in the following article which is being published0 in Review of Scientific Instruments.

Deflection of carbon dioxide laser and helium-neon laser beams in a long-pulse relativistic electron beam diode

R.A. Bosch, H. Ching, R.M. Gilgenbach, P.L.G. Ventzek,
P.R. Menge, J.J. Choi, and T.A. Spencer
Intense Energy Beam Interaction Laboratory
Nuclear Engineering Department
The University of Michigan
Ann Arbor, Michigan 48109-2104

ABSTRACT

Deflection of carbon dioxide and helium-neon laser beams has been used to measure plasma and neutral density gradients during the operating mode and after the shorting time of a long-pulse field-emission electron beam diode. Plasma density gradients of (10^{14}-10^{15}) cm^{-4} were observed throughout the diode during the final microsecond of the 2-3 μs electron beam pulse. The neutral density gradient was less than 1 x 10^{18} cm^{-4} during the electron beam pulse. Upon diode-shorting, neutral density gradients increased to (10^{18}-10^{19}) cm^{-4} over ~1 μs, and decayed over many microseconds. Plasma density gradients of ~ 10^{15} cm^{-4} were also observed after shorting. These experiments demonstrate the value of carbon-dioxide laser and helium-neon laser deflection for diagnosing plasma and neutral particles in long-pulse electron beam diodes.

PACS numbers: 41.80.Ee, 52.70.Kz, 84.70+p

I. Introduction

Field-emission electron beam diodes can be used to provide long-pulse electron beams with energies of ~ 1 MeV, pulse length ~ 1 μs, and multi-kiloampere currents.[1] In a typical diode, an electric field of hundreds of kilovolts per centimeter is applied between parallel plates separated by a few centimeters. The cathode may be covered with felt or velvet to provide electric field enhancement at the tips of fibers. The application of the electric field initiates a series of events: 1) cathode turn-on in which plasma spots form on the cathode and coalesce into a plasma layer over several ns, providing an electron source; 2) operating mode, a time period on the order of ~2 μs (for anode-cathode gaps of several cm) during which electrons from the cathode plasma are accelerated towards the anode at energies ~1 MeV, and the diode impedance drops towards zero; and 3) shorting, a high-current, low-impedance arc with decreased voltage between anode and cathode, during which the diode becomes filled with neutral particles and plasma.

The diode impedance during the operating mode is typically that of a vacuum diode whose anode-cathode separation decreases linearly with time at a velocity of several cm/μs. Researchers have frequently relied upon the time-dependent diode impedance to infer the diode properties.[2] The impedance behavior has been ascribed to the diode filling with cathode plasma (the expansion of the cathode plasma created during turn-on plus additional production), in which the boundary of the plasma-filled region moves from cathode to anode at a uniform velocity. For

sufficiently-high energy deposition in the anode by the accelerated electrons, anode plasma is also formed.[3,4]

Cathode plasma and cathode neutrals have been previously observed with optical interferometry using a nitrogen laser at λ=0.3371 μm in a relativistic electron beam diode with anode-cathode gap of 2.4 mm and 100 ns pulse length.[5] In a diode with 1.5 mm gap and 35 ns pulse length, the energy deposition in the anode by accelerated electrons was sufficient to create an anode plasma which was observed in addition to cathode plasma by visible interferometry using a ruby laser at λ = 0.6943 μm.[4] Cathode and anode plasmas were observed with ruby laser interferometry in a relativistic electron beam diode[6] and a magnetically insulated ion diode[7] with anode-cathode gaps of 5 mm. Deflection of a helium-neon laser (λ = 0.633 μm) by cathode plasma density gradients has been previously observed with a 1.2 cm diam cathode in the long-pulse diode of the present experiment at the University of Michigan.[8]

Sensitivity to plasma has been one limitation of visible light probing techniques. Sensitivity has been insufficient to observe plasma densities less than ~ 1 x 10^{16} cm^{-3}, limiting observation of plasma to the regions within a few mm of the cathode or anode. In addition, the contributions of plasma and neutrals to the measured refractive index cannot be separated with a single wavelength measurement when both species are present. This limitation is important after the diode shorts.

In this paper, we describe two-wavelength deflection measurements using carbon dioxide (CO_2) and helium-neon (He-Ne)

lasers traversing nearly identical paths through a planar diode with anode-cathode separation of 8 cm. The CO_2 laser deflection from plasma density gradients is 280 times as great as that of the He-Ne laser because of its longer wavelength (10.6 μm as opposed to 0.633 μm), while the deflection from neutral gradients are nearly the same (within 3%). As a result, increased sensitivity to plasma density gradients is provided by the CO_2 laser, allowing observation of plasma throughout the diode. From the knowledge of the deflection of both CO_2 and He-Ne lasers at the same time and location, both the plasma and neutral density gradients may be deduced. With this additional capability, density gradients after the shorting time, when both neutral and plasma species are present, have been determined.

With laser beams skimming the cathode, a cathode plasma density gradient was observed during the final μs of the 2-3 μs electron beam pulse, peaking at ~ 1.5×10^{15} cm^{-4} near shorting time. The neutral density gradient was less than 1×10^{18} cm^{-4} during this time period. Upon shorting, a neutral density gradient indicative of cathode-produced neutrals was observed near the cathode, increasing to ~ 6×10^{18} cm^{-4} over ~ 1 μs, and decaying over many microseconds. The cathode plasma density gradient reverses direction at shorting time and disappears over the following μs, consistent with the cathode plasma being pushed away from the cathode by the expanding neutral cloud. Several μs later, plasma density gradients of several 10^{14} cm^{-4} appear, with density increasing away from the cathode.

Cathode plasma density gradients of ~ 1 x 10^{14} cm^{-4} prior to shorting were observed with CO_2 laser deflection at distances of 1.5 cm and 4.5 cm from the cathode. With the CO_2 laser skimming the anode, a plasma density gradient of 2 x 10^{14} cm^{-4} increasing towards the anode was observed during the final 0.5 μs preceding shorting.

II. Apparatus

This experiment was performed using the Michigan Electron Long Beam Accelerator (MELBA), operated with parameters of peak voltage = - 900 kV, peak diode current of 50 kA, and pulselength of ~ 2 μs. This accelerator consists of a modified Marx generator, in which the voltage is compensated by a reverse-charged resistance-inductance-capacitance (RLC) ringing circuit.[9] The cold cathode was an aluminum disc of 10 cm diam covered with carbon felt, separated from the carbon anode plate by a distance of 7 cm. A shielded guard ring (OD = 14 cm) covers the edge of the fabric cathode, exposing 7.6 cm diameter of fabric. A current density of 30 - 125 A/cm^2 was thereby produced. Voltage was measured with a resistive divider, while anode current was measured with wide-band current transformers (Pearson Electronics 110A) on four isolated current return paths.

A schematic of the experiment is shown in Figure 1. A 5 mW He-Ne laser is directed through the diode, upon a 10.8 m path into a Faraday cage, through a He-Ne line filter, to a photodiode quadrant detector (Silicon Detector Corporation SD-380-23-21-051) with a very fast differential amplifier.[10]

With the resultant laser spot size (~ 1 cm), the detector output is proportional to the laser spot position over a distance of ~ 1 cm, so that deflections up to ±0.5 mrad can be measured.

A 1-5 W CO_2 laser provides a 7 mm beam for infrared laser deflection. The beam traverses 6 m, then is reduced and focused using a NaCl lens pair 2 m from the diode, with best focus in the diode. This provides a beam diameter of ~ 5 mm on its 7.6 cm path through the diode, which is nearly identical to the He-Ne path in the diode. Because of diffraction effects, the CO_2 beam diameter cannot be significantly reduced over a 7.6 cm path length. The beam is then directed on a 11.3 m path to the Faraday cage, and focused onto a detector using a NaCl lens with 10 cm focal length. A knife edge bisects the beam (diam ~ 4 cm) as it exits this final lens. The detector used was a liquid-nitrogen-cooled Raytheon IR101 PbSnTe detector with Raytheon DA-20 preamplifier (bandwidth of 20 Hz to 4 MHz), filtered with a 10.6 μm line filter. The portion of the beam intersected by the knife edge changes with the laser spot position, so that the detector signal varies linearly with laser spot position over a distance of ~ 2 cm. Deflections up to ± 1 mrad can thus be measured.

Response curves of the CO_2 and He-Ne laser deflection systems are shown in Figure 2. A position shift of 1 cm over the 10 m path from the diode to the detectors corresponds to a deflection of 1 mrad. Deflection signals were converted from mV to mrad using the slope of these curves at the initial laser spot position. Because the CO_2 laser power varied from shot to shot, the curve in Fig. 2(a) was normalized to the laser power

for each shot. Electrical noise upon the deflection signals was monitored during each data run by performing shots with the laser paths blocked.

III. Theory

Laser deflection results from plasma and neutral density gradients (dn_e/dz and dn_n/dz) in the diode according to:

$$\theta = L\, d\eta/dz = L\, (\, K_e\, dn_e/dz + K_n\, dn_n/dz\,) \qquad (1)$$

where θ is the deflection angle in radians, L is the path length through the diode (7.6 cm), z is the distance from the cathode to the laser path, η is the refractivity of the medium in the diode, K_e is the Gladstone-Dale constant for plasma electrons (in cm^3/electron), and K_n is the Gladstone-Dale constant for neutrals (in cm^3/atom). K_e and K_n have opposite signs, so that the laser is deflected in opposite directions by plasma and neutral density gradients.

K_e equals $(2\, n_c)^{-1}$, where n_c is the critical plasma density for the laser wavelength. K_e depends upon the laser wavelength as λ^2; K_n depends upon the neutral species composition, but has little dependence upon laser wavelength. $K_e = 5.0 \times 10^{-20}$ cm^3/electron for the CO_2 laser beam ($\lambda = 10.6$ μm), while $K_e = 1.8 \times 10^{-22}$ cm^3/electron for the He-Ne laser beam ($\lambda = 0.633$ μm).[10] Thus, the CO_2 laser deflection is 280 times as sensitive

to plasma electrons. For neutral carbon atoms, $K_n = -6.25 \times 10^{-24}$ cm^3/atom for the CO_2 laser and -6.4×10^{-24} cm^3/atom for the He-Ne laser,[11] a difference of only 3 %. A summary of the laser deflection parameters is given in Table 1.

From equation (1), we can write:

$$\theta_{CO_2} = (7.6 \text{ cm})[(5.0\times10^{-20}\text{cm}^3)\,dn_e/dz - (6.25\times10^{-24}\text{cm}^3)\,dn_n/dz] \quad (2)$$

$$\theta_{HeNe} = (7.6 \text{ cm})[(1.8\times10^{-22}\text{cm}^3)\,dn_e/dz - (6.4\times10^{-24}\text{cm}^3)\,dn_n/dz] \quad (3)$$

Multiplying eq.(3) by 0.97 and subtracting it from eq. (2) yields:

$$\theta_{CO_2} - (0.97)\theta_{HeNe} = (7.6 \text{ cm})[(5.0 \times 10^{-20}\text{cm}^3)\,dn_e dz] \quad (4)$$

Equation (4) allows the plasma density gradient to be determined from the measured deflections. Similarly,

$$\theta_{HeNe} - (0.0036)\theta_{CO_2} = (7.6 \text{ cm})[-(6.4 \times 10^{-24}\text{cm}^3)\,dn_n dz] \quad (5)$$

For CO_2 and HeNe deflection angles of the same order of magnitude, the CO_2 contribution to eq. (5) is negligible, so that the HeNe laser deflection may be attributed to neutral density gradients. This is the case in our results. The CO_2 deflection minus 0.97 times the HeNe deflection is proportional to the plasma density gradient. Prior to diode shorting, the He-Ne deflection was not observable, so that the CO_2 deflection is proportional to the plasma density gradient.

IV. Results

Observations with He-Ne and CO_2 laser beams simultaneously skimming the cathode have showed deflection angles of the same order of magnitude for both lasers. This indicates that the observed He-Ne deflection results from the neutral density gradient. In Fig. 3, we display data for laser beams skimming the cathode. The He-Ne deflection is not observable during the operating mode of the diode, indicating that the neutral density gradient is less than 1×10^{18} cm^{-4}. Upon shorting, cathode-produced neutrals produce a density gradient of carbon atoms building to 6×10^{18} cm^{-4} over ~ 1 μs, and decreasing over several microseconds. Similar He-Ne deflection signals were observed in other locations near the cathode. When the He-Ne laser skimmed the anode, the deflection signal was similar but inverted, consistent with anode-produced neutrals.

Subtracting the neutral-produced deflection from the CO_2 deflection signal yields the plasma-produced deflection, shown in Fig 3(e). This is a bipolar signal indicating a cathode-plasma density gradient building to ~ 1.5×10^{15} cm^{-4} during the final microsecond of the operating mode. The deflection reverses direction at shorting time and builds to a comparable angle in the opposite direction, indicating that plasma density increases away from the cathode. This is consistent with the cathode plasma being pushed away by cathode-produced neutrals after the shorting time. A plasma density gradient of 5×10^{14} cm^{-4} increasing away from the cathode is observed 4 μs after shorting, showing the presence of

plasma during the arc. On some shots, this feature was not observed, while other shots showed several plasma density gradient peaks during the arc.

At other locations within the diode, CO_2 laser and He-Ne laser deflection were performed on separate shots. The He-Ne deflection was not observable (< 0.05 mrad) during the operating mode, indicating that the neutral density gradient was less than 1×10^{18} cm^{-4}. Upon shorting, the He-Ne deflection increased over ~ 1 μs, sometimes in an irregular fashion, and then gradually decreased over many microseconds. Near the cathode (anode), the neutral density increased in the direction of the cathode (anode). Shot-to-shot variability prevented a complete analysis of the post-shorting CO_2 signals, for which both plasma and neutral gradients contribute. However, the contribution from the neutral density gradient following shorting could frequently be identified as a slowly decreasing deflection, upon which larger deflections from plasma gradients were superimposed. Because of the small (unobservable) neutral density gradient prior to shorting, the CO_2 laser deflection observed prior to shorting is proportional to the plasma density gradient.

In Figure 4, we show the CO_2 laser deflection signals for several shots at various positions within the diode. Prior to shorting, the deflection is proportional to the plasma density gradient. A plasma density gradient of 2.6×10^{15} cm^{-4} corresponds to a 1 mrad deflection. After shorting, the majority of the deflection is attributable to the plasma density gradient, summed with a smaller slowly-decreasing neutral

density gradient signal. For deflections attributable to plasma gradients, a scale for dn_e/dz is shown in Fig. 4.

Figure 4(a) shows the CO_2 laser deflection when the laser was positioned 1.5 cm from the cathode. A deflection from a cathode plasma density gradient of ~ 1 x 10^{14} cm^{-4} is observed prior to shorting, and develops into a bipolar plasma signal with peak plasma density gradients of ~ 1 x 10^{15} cm^{-4}. Compared with the bipolar signal observed with the probe skimming the cathode, this signal has about one-half the magnitude, occurs 1-2 μs later, and lasts nearly twice as long. Finally, a slowly-decaying neutral-produced gradient remains, with about one-fifth the magnitude observed skimming the cathode.

Figure 4(b) shows the CO_2 deflection at a position 4.5 cm from the cathode (3.7 cm from the anode). At this position near the center of the diode, several cm from cathode or anode, a deflection from a cathode plasma density gradient of ~1x10^{14} cm^{-4} was observed 0.5 μs prior to shorting. To our knowledge, this is the first detection of plasma during the operating mode of a relativistic electron beam diode several cm from either electrode.

In Fig. 4(c), we display a signal with the CO_2 laser skimming the anode. When this data was taken, observations with the laser path blocked showed that negative-going electrical noise signals were associated with transient arcs during the first 2 μs of the pulse. Consequently, the first negative-going voltage pulse on the laser deflection signal is likely to be

noise. During the final 0.5 μs of the pulse, a plasma density gradient of 2 x 10^{14} cm^{-4} is observed, with density increasing towards the anode. The anode surface energy deposition by accelerated electrons is expected to be ~ 300 J/g by this time. This is comparable to the absorbed dose of 330-500 J/g required for the observation of anode plasma from a graphite anode in an earlier study of relativistic electron beam diodes.[3] Consequently, the plasma density gradient may result from anode-produced plasma. Alternatively, the observed plasma deflection may result from cathode-produced plasma which has flowed to the anode and stagnated. Upon shorting, the deflection reverses, and after 1 μs, only a slowly-decreasing signal associated with anode-produced neutrals remains. Three microseconds later, plasma deflection signals are again observed.

In Fig 4(d), we display a signal with the CO_2 laser located 1.5 cm from the cathode, for a shot in which a transient arc precedes shorting. A cathode plasma density gradient of 2 x 10^{14} cm^{-4} is apparent during and after the transient arc. This indicates the ability to examine plasma created during transient arcs. The large negative deflection signal for t > 4 μs is clipped by the response of the knife-edge/detector system.

In Fig. 4(e), we display a signal with the CO_2 laser located 1.5 cm from the cathode, for a shot in which the diode voltage is crowbarred at 1 μs. A pulse similar to the cathode plasma pulse of Fig. 4(a) is observed, but there is no persistent signal from a neutral density gradient. This is

consistent with observations that neutral-ablation is prevented by voltage crowbarring.

The data of Figures (3) and (4) demonstrate the ability of CO_2 laser deflection to detect cathode plasma throughout the diode during the operating mode. In conjunction with simultaneous He-Ne deflection observations, the post-shorting deflection signals, which include deflection from plasma and neutrals, may be interpreted.

V. Summary

Deflection of He-Ne and CO_2 laser beams by a relativistic electron beam diode allows measurement of plasma and neutral density gradients. The He-Ne laser deflection is primarily a result of neutral density gradients of $(10^{18}-10^{19})$ cm^{-4}. Prior to shorting, neutral density gradients are not observable ($< 10^{18}$ cm^{-4}). The neutral gradients build up during the first microsecond after the diode shorts, and decay over many microseconds. Near the cathode (anode), the neutral density increases in the direction of the cathode (anode).

The CO_2 laser deflection is largely a result of plasma density gradients of $(10^{14}-10^{15})$ cm^{-4} during the final microsecond preceding diode shorting, and during the subsequent arc. Near the cathode (anode), the plasma density prior to shorting increases in the direction of the cathode (anode). Near the middle of the diode, plasma density increases in the direction of the cathode prior to shorting.

With CO_2 laser deflection, plasma density gradients as small as $\sim 1 \times 10^{14}$ cm^{-4} can be observed throughout the diode.

Thus, CO_2 laser deflection is a promising plasma diagnostic for long-pulse relativistic electron beam diodes. The He-Ne laser deflection provides a diagnostic of neutral density gradients. When CO_2 laser deflection is used in conjunction with He-Ne laser deflection, plasma and neutral density gradients may be determined prior to shorting and during the subsequent arc.

Acknowledgments

This work was sponsored by Los Alamos National Laboratory.

References.

1. L.A. Rosocha and K.B. Riepe, Fusion Tech. 11, 576 (1987).

2. J.J. Ramirez and D.L. Cook, J. Appl. Phys. 51, 4602 (1980).

3. R.K. Parker, R.E. Anderson, and C.V. Duncan, J. Appl. Phys. 45, 2463 (1974).

4. D.W. Swain, S.A. Goldstein, L.P. Mix, J.G. Kelly, and G.R. Hadley, J. Appl. Phys. 48, 1085 (1977).

5. D.D. Hinshelwood, IEEE Trans. Plasma Sci. PS-11, 188 (1983); see also D.D. Hinshelwood, Explosive emission cathode plasmas in intense relativistic electron beam diodes, Ph.D. thesis, Department of Physics, Massachusetts Institute of Technology, 1984.

6. J.G. Kelly and L.P. Mix, J. Appl. Phys. 46, 1084 (1975).

7. D.J. Johnson, E.J.T. Burns, J.P. Quintenz, K.W. Bieg, A.V. Farnsworth, Jr., L.P. Mix, and M.A. Palmer, J. Appl. Phys. 52, 168 (1981).

8. M.E. Cuneo, Characteristics of the time-evolution of a microsecond electron beam diode with anode effects, Ph.D. thesis, Department of Nuclear Engineering, The University of Michigan, 1989.

9. R.M. Gilgenbach, L.D. Horton, R.F. Lucey, Jr., S. Bidwell, M. Cuneo, J. Miller, and L. Smutek, in Proceedings of the 5th IEEE Pulsed Power Conference, Arlington, VA, June 10-12, 1985, (IEEE, New York, 1985), p. 126.

10. C.L. Enloe, R.M. Gilgenbach, and J.S. Meachum, Rev. Sci. Instrum. 58, 1597 (1987).

11. W.C. Gardiner, Jr., Y. Hidaka, and T. Tanzawa, Combustion and Flame 40, 213 (1981).

TABLE.1

Parameter	CO_2 Laser	HeNe Laser
Wavelength	10.6 μm	632.8 nm
Power	1-5 W	5 mW
Detector	Knife-edge/PbSnTe/cooled	Solid state quadrant
K_e	5.0×10^{-20} cm^3/electron	1.8×10^{-22} cm^3/electron
$K_{neutral}$ (Atomic Carbon)	-6.25×10^{-24} cm^3/atom	-6.4×10^{-24} cm^3/atom
Minimum Observable Deflection	5×10^{-5} radian	5×10^{-5} radian
dn_e/dz (minimum)	1×10^{14} cm^{-4}	4×10^{16} cm^{-4}
$dn_{neutral}/dz$ (minimum)	10^{18} cm^{-4}	10^{18} cm^{-4}

Figure Captions:

Figure 1: Experimental configuration.

Figure 2: Calibration curves for laser deflection systems:

(a) CO_2 laser calibration curve.

(b) He-Ne laser calibration curve.

Figure 3: Laser deflection data with lasers skimming the cathode.

(a) Cathode voltage.

(b) Anode current.

(c) He-Ne deflection signal.

(d) CO_2 deflection signal.

(e) CO_2 deflection minus 0.97 times the He-Ne deflection.

Figure 4: Voltage pulse, anode current pulse, and CO_2 laser deflection signals for five shots.

(a) Laser positioned 1.5 cm from the cathode.

(b) Laser positioned 4.5 cm from the cathode (3.7 cm from the anode).

(c) Laser skimming the anode.

(d) Laser positioned 1.5 cm from the cathode, for a shot with a transient arc preceeding diode shorting.

(e) Laser positioned 1.5 cm from the cathode, for a shot in which the voltage is crowbarred after 1 μs.

7.0 X-Ray Emission as a Voltage Diagnostic for Microsecond Electron Beam Diodes

A series of experiments were performed in order to determine whether X-ray emission can be utilized as a diagnostic for electron beam diode voltage. The basic idea is that filtered x-ray detection signals could be post-processed as a diagnostic of e-beam voltage. X-ray-emission voltage diagnostics would have several advantages over capacitive probes: 1) Totally noninvasive, they could be installed on the outside of the diode without breaking vacuum, 2) High signal to noise ratio, since the scintillator light is transmitted by fiberoptic cable to a photomultiplier tube located in the Faraday cage, and 3) Inexpensive.

The X-ray probe employed in these experiments is depicted in Figure 7-1. Two 1/8" pieces of NE102 scintillator are mounted on the end of a lucite light guide that tapers to a fiberoptic cable; these elements are enclosed in a copper tube which is sealed at the end by a copper plug. The fiberoptic cable runs through polyethylene tubing (for mechanical protection) to a Hammamatsu photomultiplier tube in the Faraday cage. In this preliminary set of experiments, X-ray filters were constructed by wrapping multiple layers of 0.34 cm thick lead sheet around the end of the x-ray probe in a lead-sandwich arrangement. The experimental configuration is depicted in Figure 7-2.

Measurements were made at two locations on the MELBA diode: 1) On top of the aluminum diode chamber, and 2) In-line with the MELBA anode. For comparison all of the shots presented here were taken with a uniform magnetic field (~ 500 G). Typical data signals for three layers of lead on the top probe location are shown in Figures 7-3 (M2035) and 7-4 (M 2032). The x-ray data signals have been shifted in time by 110 ns in order to synchronize the signals.

Interpretation of a single x-ray power signal can be done in several ways. The simplest scaling (p 47 in the 1986 NRL plasma formulary) of X-ray power (X) to beam power is:

$X / IV = KV$, where I is the e-beam current and V is the beam voltage, and K is a constant,

Then one can solve for V:

$$V = (X/IK)^{1/2},$$

so that the beam voltage can be found by taking the square root of the ratio of the X-ray signal to the current. These initial experimental data have been plotted with a number of different normalizations in Figures 7-5 and

7-6. It can be see. ..iat for the top measurement, the . ay signal increases with time as the beam voltage droops. This can be explained by the increasing current and by the relatively thin filter (3 layers) on the x-ray probe.

Much better results were obtained when the x-ray probe was located in front of the anode, with 3, 4, and 5 sheets of lead around the probe. Typical data are shown in Figures 7-7 (M2037), 7-8 (M2039), and 7-9 (M2041). It can be seen that the amplitude of the x-ray signals decreased relative to the top probe location when the x-ray probe was placed in line with the anode. This is partly because the anode material is carbon, which would give less x-rays by comparison with the Z from the walls of the aluminum chamber. It should be noted that an empirical analysis of this data in Figures 7-10, 7-11, and 7-12 shows excellent agreement of the square root of the x-ray signal with the beam voltage. The square root of x-rays divided by beam current gives a less accurate reproduction of the voltage. Detailed comparisons of voltage to square root of x-ray signal are presented in figure 7-13. *It can be seen that the best representation of the voltage is given by the square root of the X-ray signal for the front measurement with 5 layers of lead (M2041), the second best result is the front measurement with 4 layers of lead (M2039), followed by the front measurement with 3 layers of lead (M2037). The top measurements yielded worse agreement.*

Data from these experiments indicates that x-ray emission could be a sensitive, inexpensive diagnostic for voltage in electron beam diodes.

8.0 Electric Stress in Microsecond Electron Beam Diodes

We have analyzed MELBA diode data in order to compare the relationship between peak electric field and shorting/arcing pulselength with the plot of diode electric field versus pulselength, referred to as the McGeoch criterion:[1,2]

$$E_k = 70/\tau^{1/2}$$

Note that since MELBA shots may or may not show signs of arcing (voltage notch during the pulse) before the diode shorts, we have compiled the data for a number of cases:

1) *Average* Electric stress (Voltage divided by A-K gap)
   a) versus *arcing* time (first notch in voltage)
   b) versus *diode shorting* time (total pulselength: diode voltage drops to zero)
2) Peak electric stress (from Hermannsfeldt code)
   a) versus *arcing* time
   b) versus *shorting* time

Note that MELBA shots which shorted before any apparent arcing were plotted assuming that the arcing time was equal to the shorting time. Data for all four of the above cases are plotted for both the old cathode A (planar graphite felt with a guard ring), and a new cathode (B), described in section 3. Our old cathode (cathode A) had a relatively high peak electric stress due to the small radius on the outer edge of the cathode. The second data set is MELBA data for the case of our new quasi-Chang profile cathode (B) on the hemispherical-end cathode stalk; this cathode B configuration gave the longest pulses (4.5-5 μs) and maximum delivered e-beam energy obtained on MELBA (discussed in section 5).

Figure 8-1 of *average* electric stress versus *arcing* time showed that cathode A diodes lie below the McGeoch (MG) line for the unmagnetized case, but magnetized diodes lie near and above the McGeoch line. Cathode B arcing time data lies mostly above the MG line for the magnetized cases because of the long pulselengths of these shots.

Figure 8-2 data on *average* electric stress versus *shorting* time show that cathode A data lies on the MG line for the unmagnetized case and slightly above the MG line for magnetized shots. For cathode B, the long pulselength of the magnetized shots moved them further above the MG line than the unmagnetized shots.

The plot of *peak* electric stress versus *arcing* time (Figure 8-3), illustrates that the high peak electric stress of cathode A places the data well above the McGeoch line. Cathode B has considerably lower peak electric stress but longer pulses, which also pushes the data above the MG line. In both cathodes, the magnetized data is further above the MG line than the unmagnetized shots.

In the plot of [illegible] electric stress versus shorting [illegible] (Figure 8-4), both cathode A and cathode B lie well above the MG line for both magnetized and unmagnetized shots.

In summary, it appears that the McGeoch line plot is a reasonably good approximation for *average* electric stress versus *arcing* time, for the unmagnetized case. In the magnetized case, well designed cathodes at long pulses may operate significantly above the McGeoch line. Peak electric stress data can lie well above the MG line for cathodes (A) with large edge enhancement. However, cathodes (B) with low edge enhancement give longer pulselengths which also permit operation above the McGeoch line. It is possible that the operating regime of long-pulse (>2 μs) diodes may flatten out the E vs. τ operating curve near 60-70 kV, permitting much longer pulselengths at these fields.

The physical mechanisms for arcing and diode shorting require further investigation. Note that the anode material was Poco graphite; cathode A used graphite felt/glyptal, whereas in cathode B experiments the cathode surfaces were velvet/ glyptal. Other anode and cathode materials could yield different scaling.[2] Since the plotted data only included non-crowbarred shots, the electric stress standoff of these data was reduced from its ideal value because the glyptal coating was damaged by diode shorting. It is clear that the electrostatic design of the cathode and magnetic field configuration are important in operating significantly above the McGeoch criterion for a given voltage and A-K gap. If the physical mechanisms for breakdown are found, it may be possible to design diodes which will operate well above the McGeoch line.

Section 8 References

1) M. McGeoch, "Scaling Issues in Electron Beam Diodes", Los Alamos National Laboratory Workshop on Large Area Electron Beam Diodes, Monterrey, CA, June 1989

2) Louis A. Rosocha, "Anode Plasma Formation as A Possible Mechanism for an Electrical Stress Limit in Cold Cathode Diodes", Supplement to Proceedings of LANL Workshop on Large Area Electron Beam Diodes, Monterrey, CA, June 1989, (LA-UR-90-655)

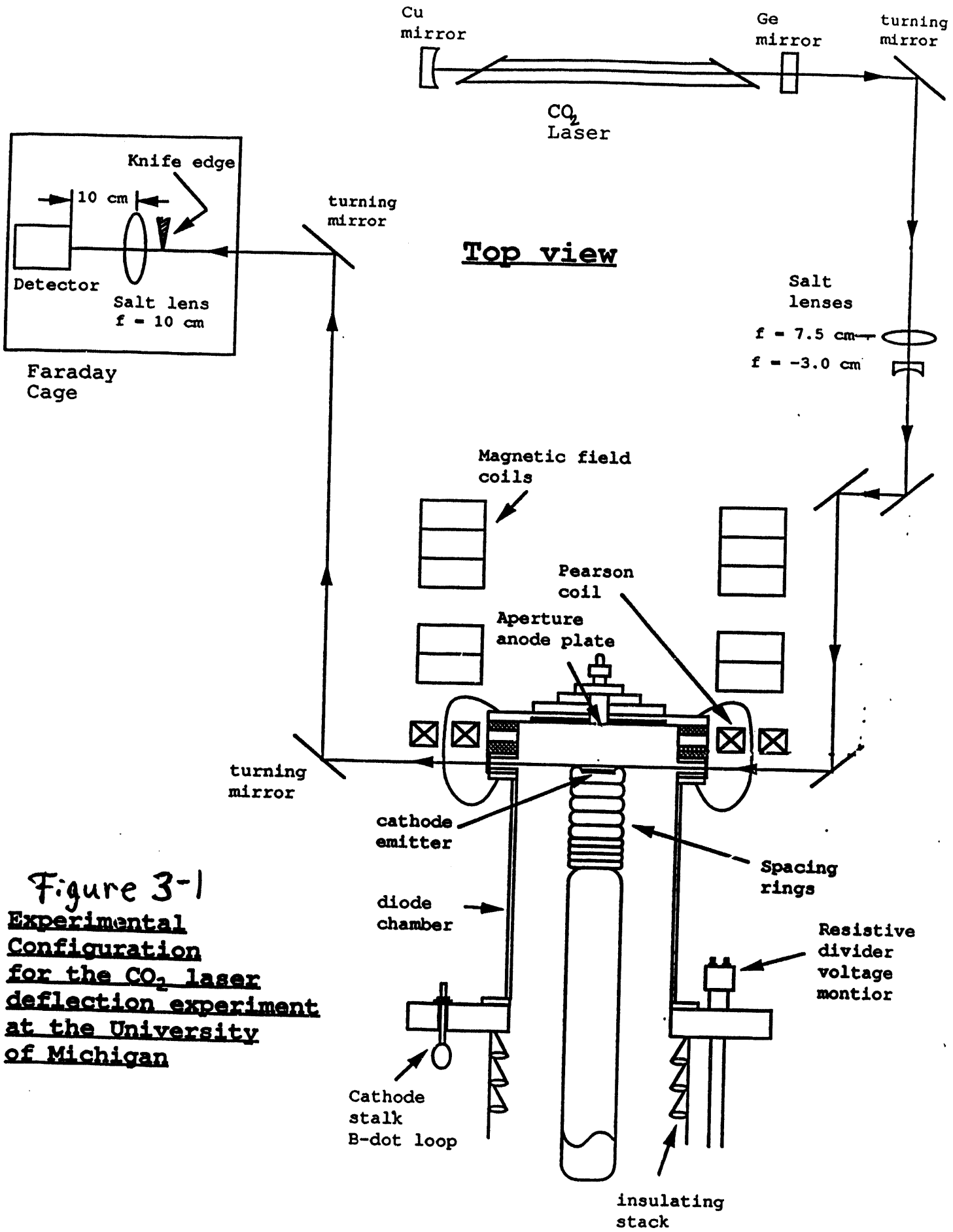

Figure 3-1

Experimental Configuration for the CO_2 laser deflection experiment at the University of Michigan

MELBA Cathodes

Cathode A: Old planar cathode with guard ring

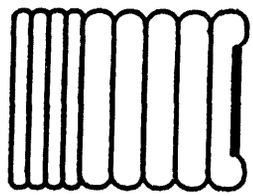

Cathode B: Profiled cathode on hemispherical cathode stalk

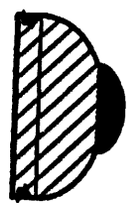

Cathode C: Large Area Planar cathode with Toroid

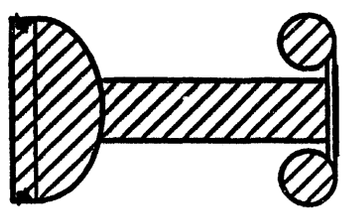

Figure 3-2

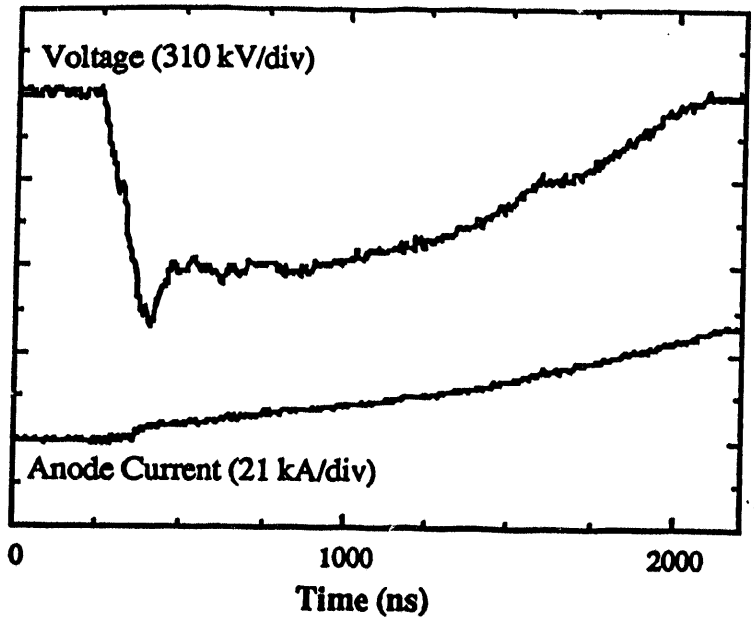

Figure 4-1 **Voltage and anode current for the gradient magnetic field condition for the planar cathode (shot M1850).**

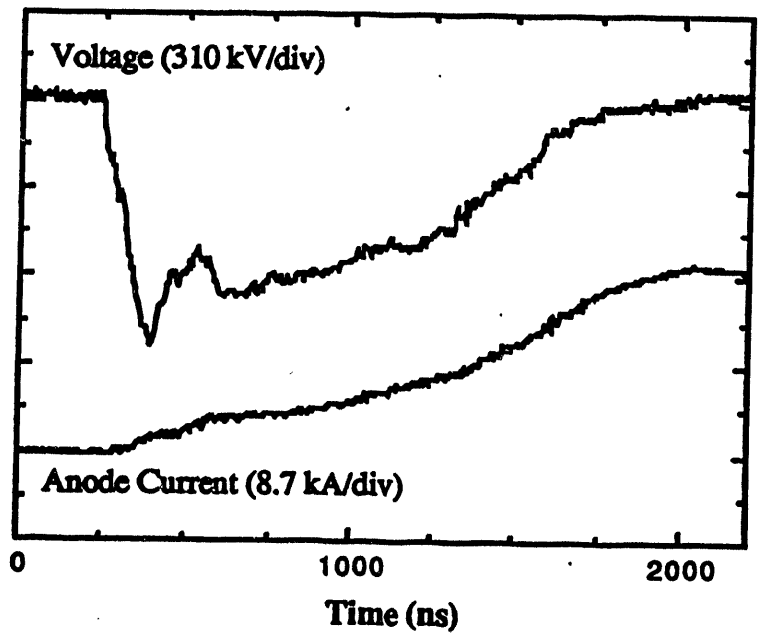

Figure 4-2 **Voltage and anode current for the uniform magnetic field condition for the planar cathode (shot M1852).**

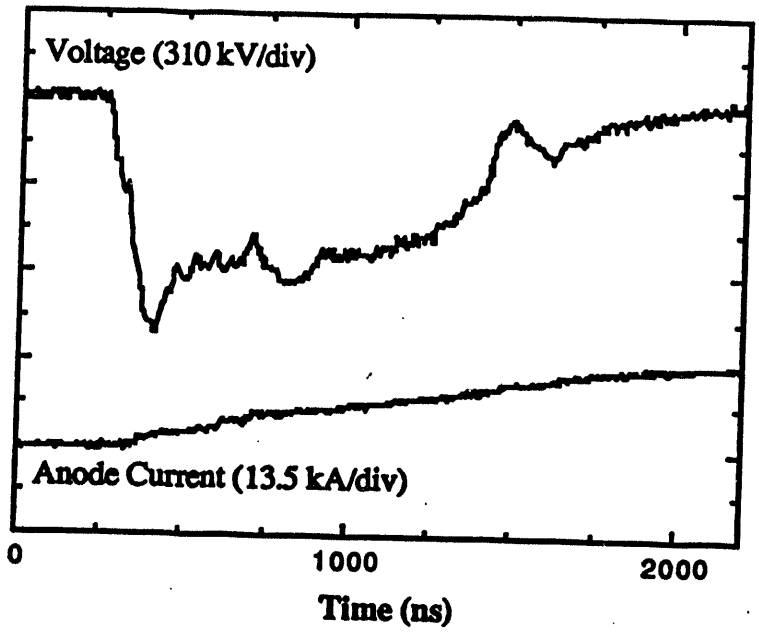

Figure 4-3 Voltage and anode current for the zero magnetic field condition for the planar cathode (shot M1851).

Figure 4-4
Magnetic Field Lines for the Gradient and Uniform Cases

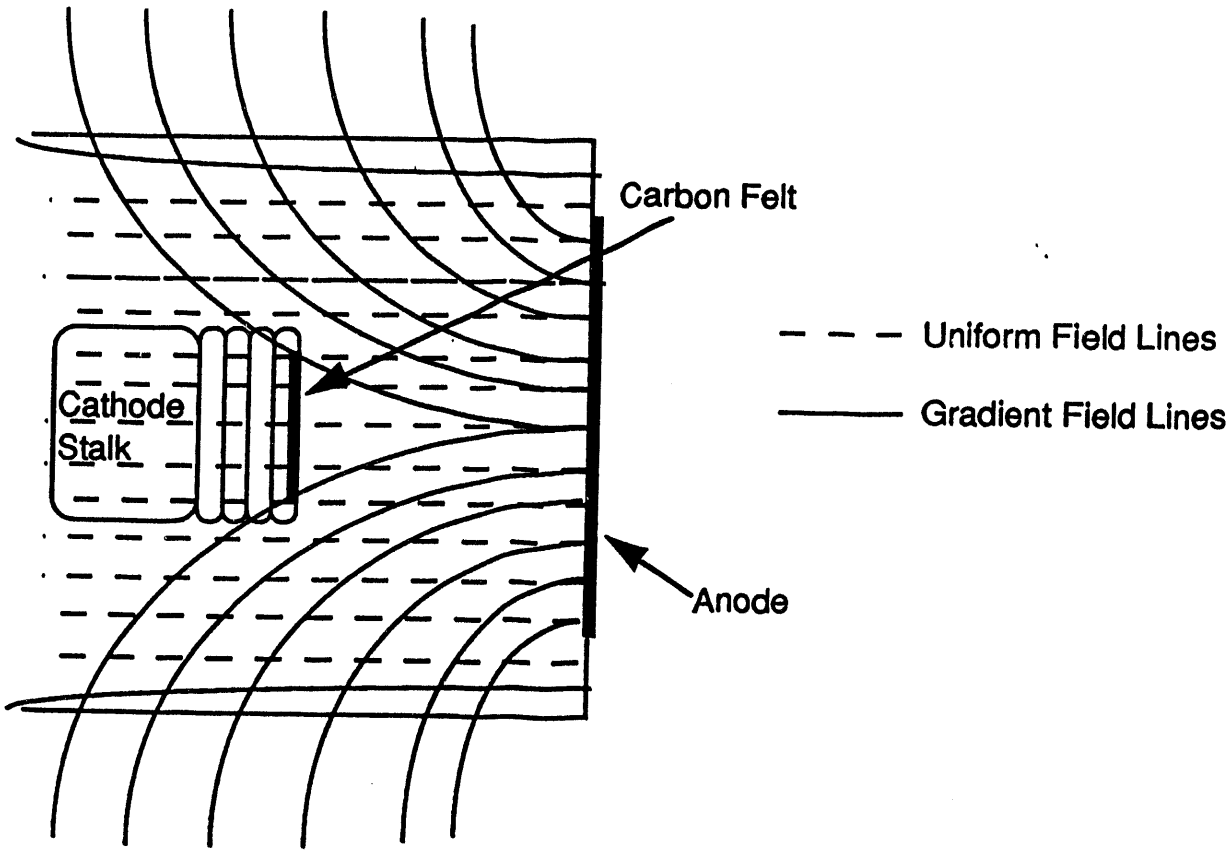

AKAnode.m1850t

Cathode A

Comparison of Anode I AK Gap With C-L Planar M1850

Grad B

GRADIENT

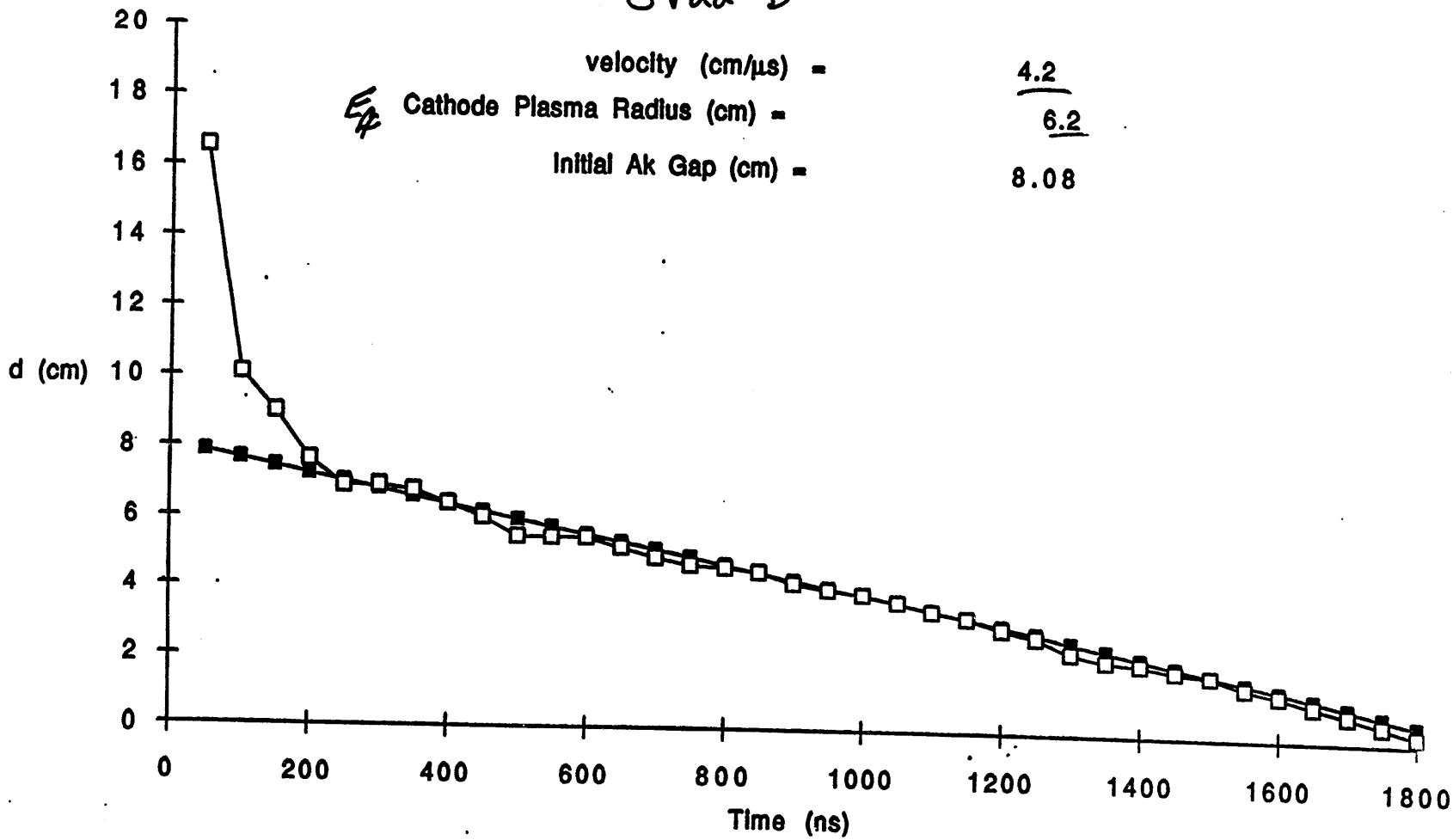

Figure 4-5

1/sqrt(p)diode.1850t

Cathode A

I_{Diode}

1/sqrt(p) comparison M1850

Grad B

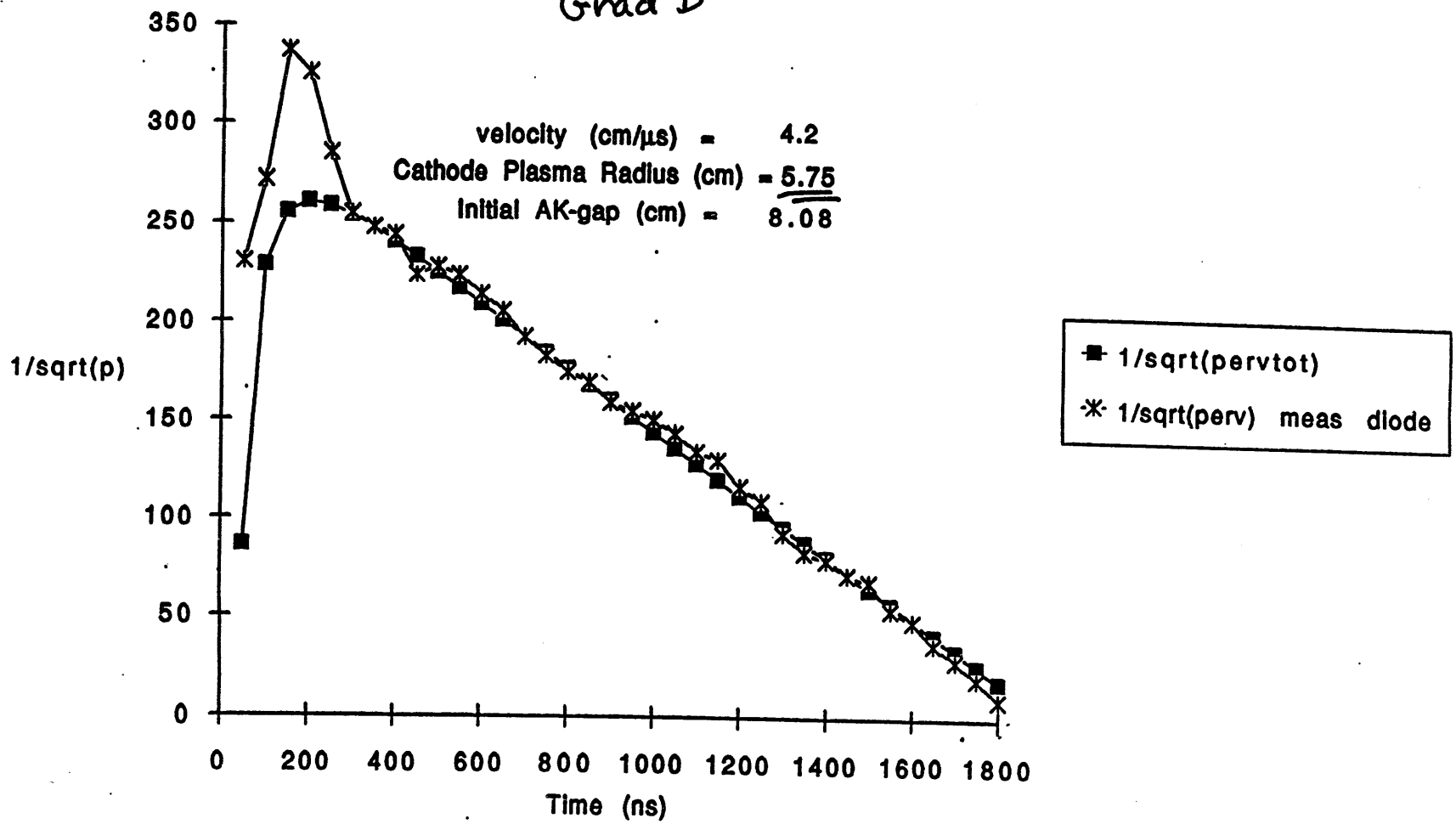

Figure 4-6

AKAnoue.m1851

B=0

Cathode A

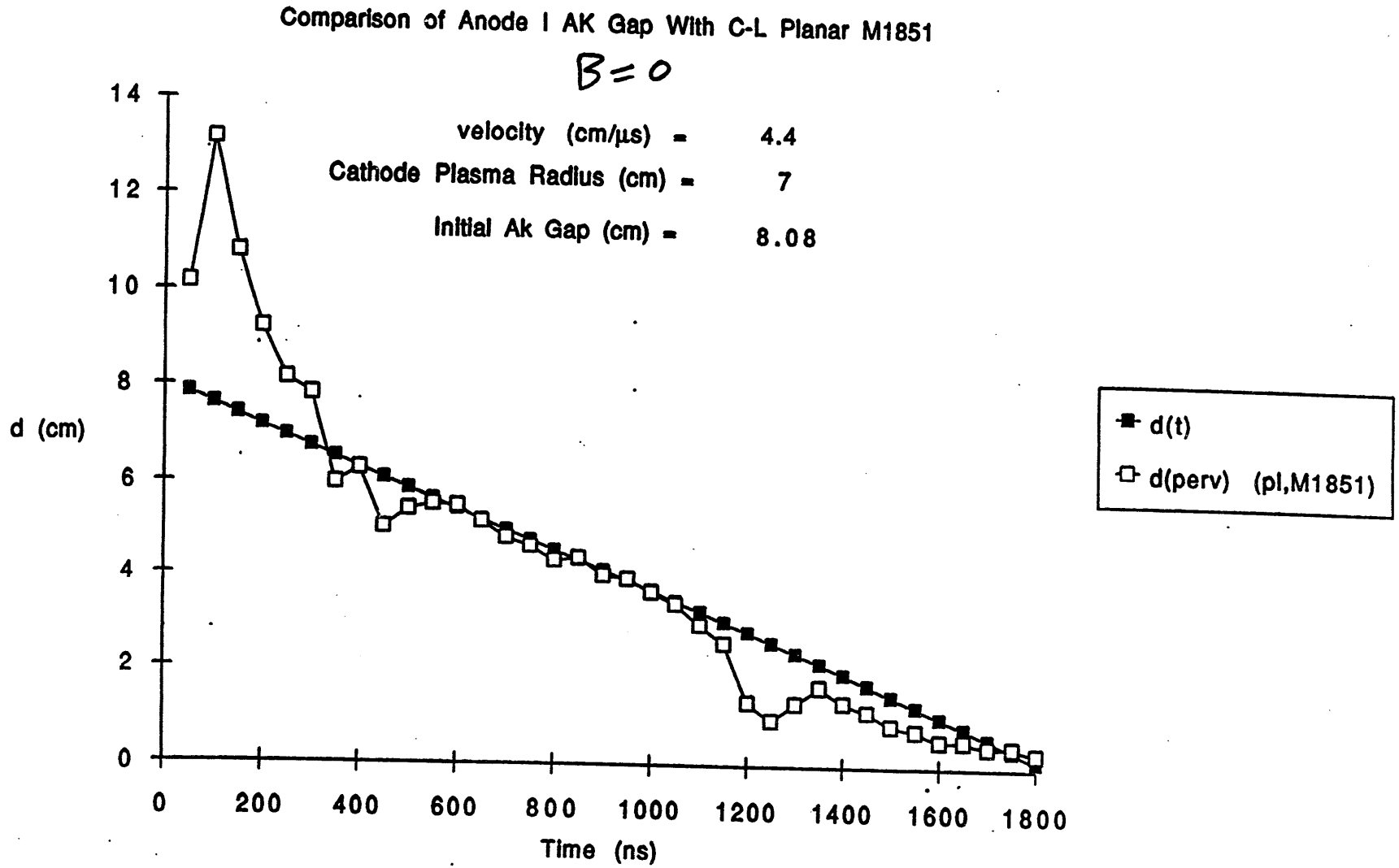

Figure 4-7

1/sqrt(p)comp.1851

Cathode A

I_D

1/sqrt(p) comparison M1851

B = 0

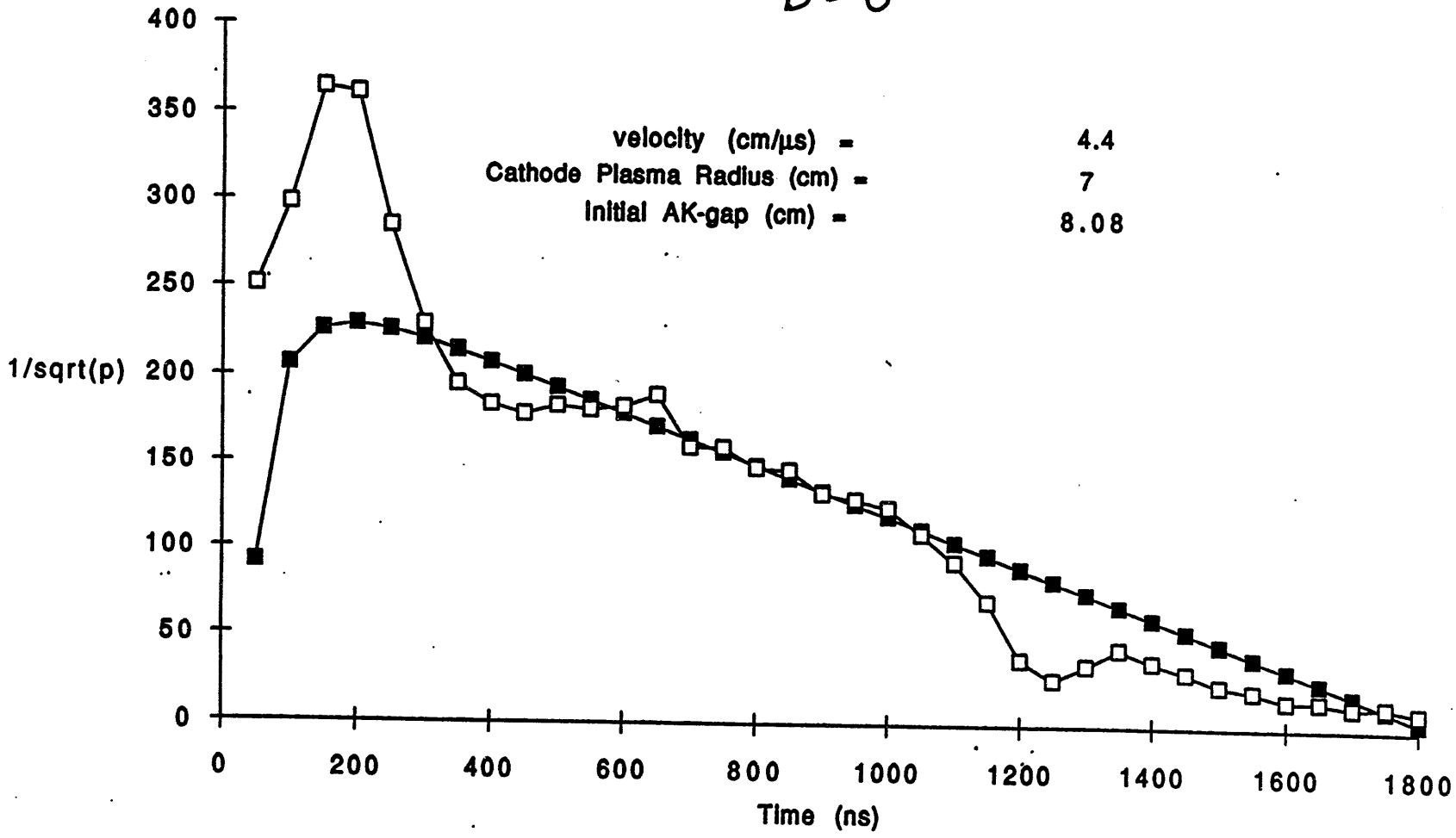

Figure 4-8

AKAnode.m1852t

Cathode A ~ UNIFORM

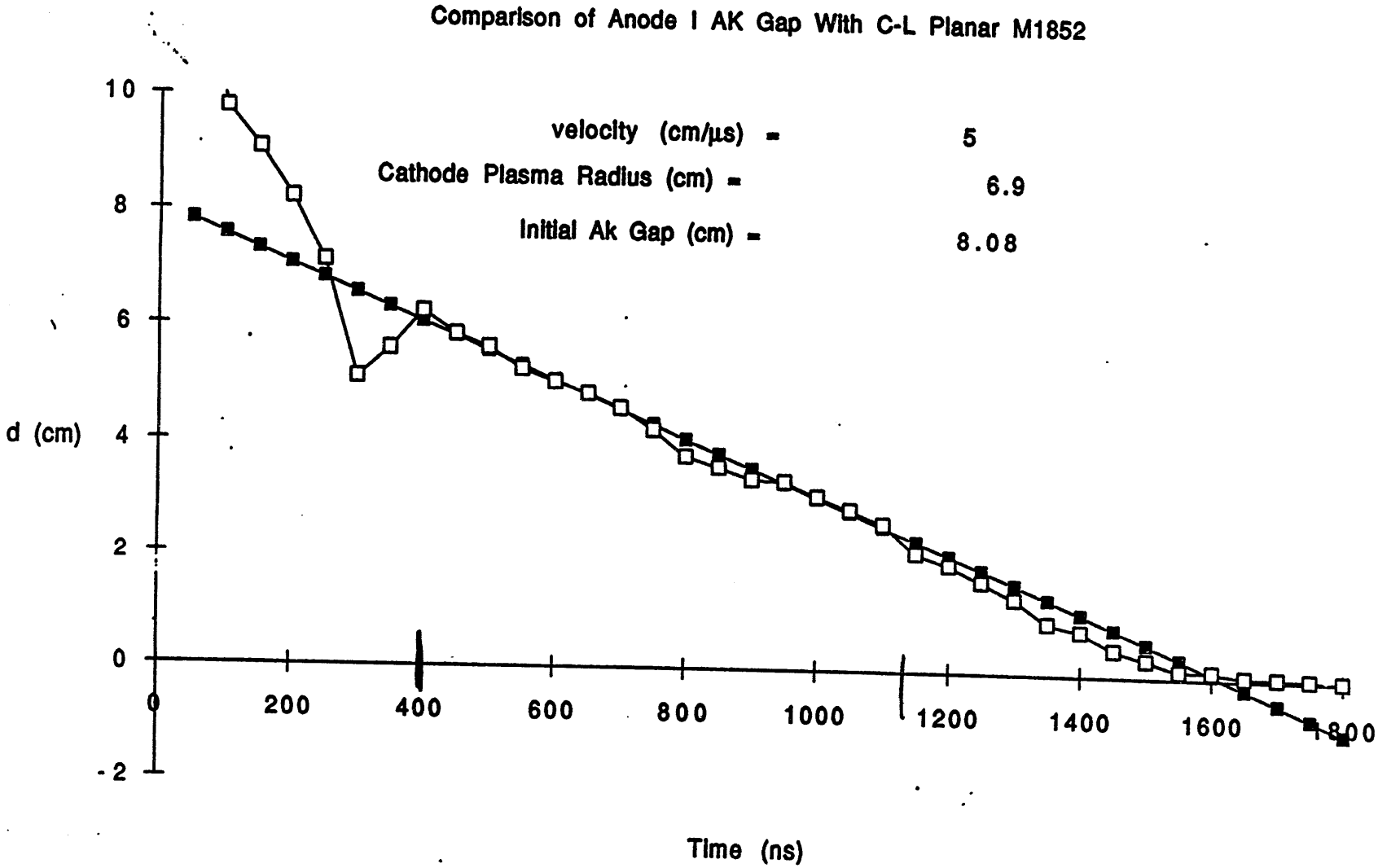

Figure 4-9

1/sqrt(p)diode.1852t

~UNIFoam

Cathode A

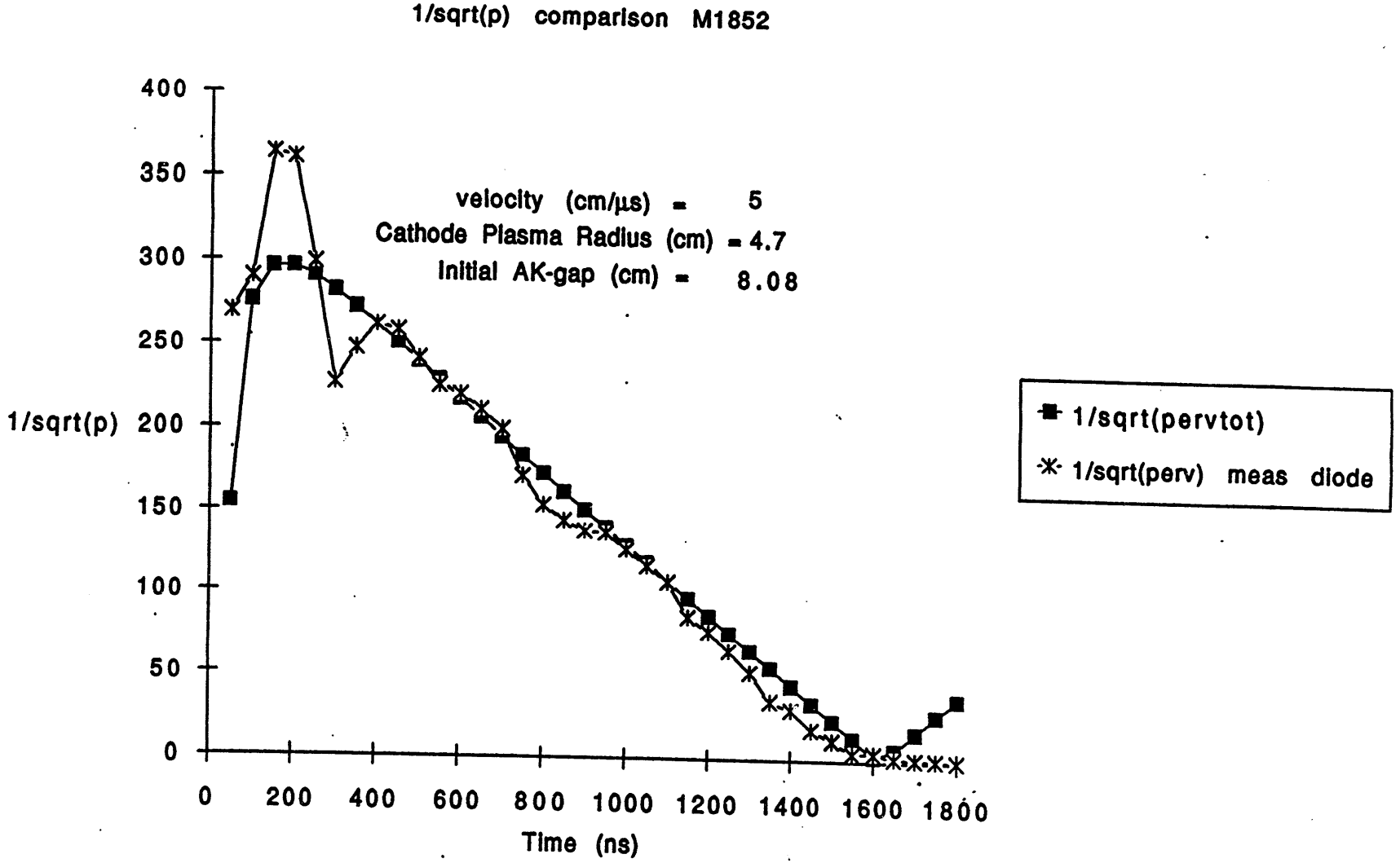

Figure 4-10

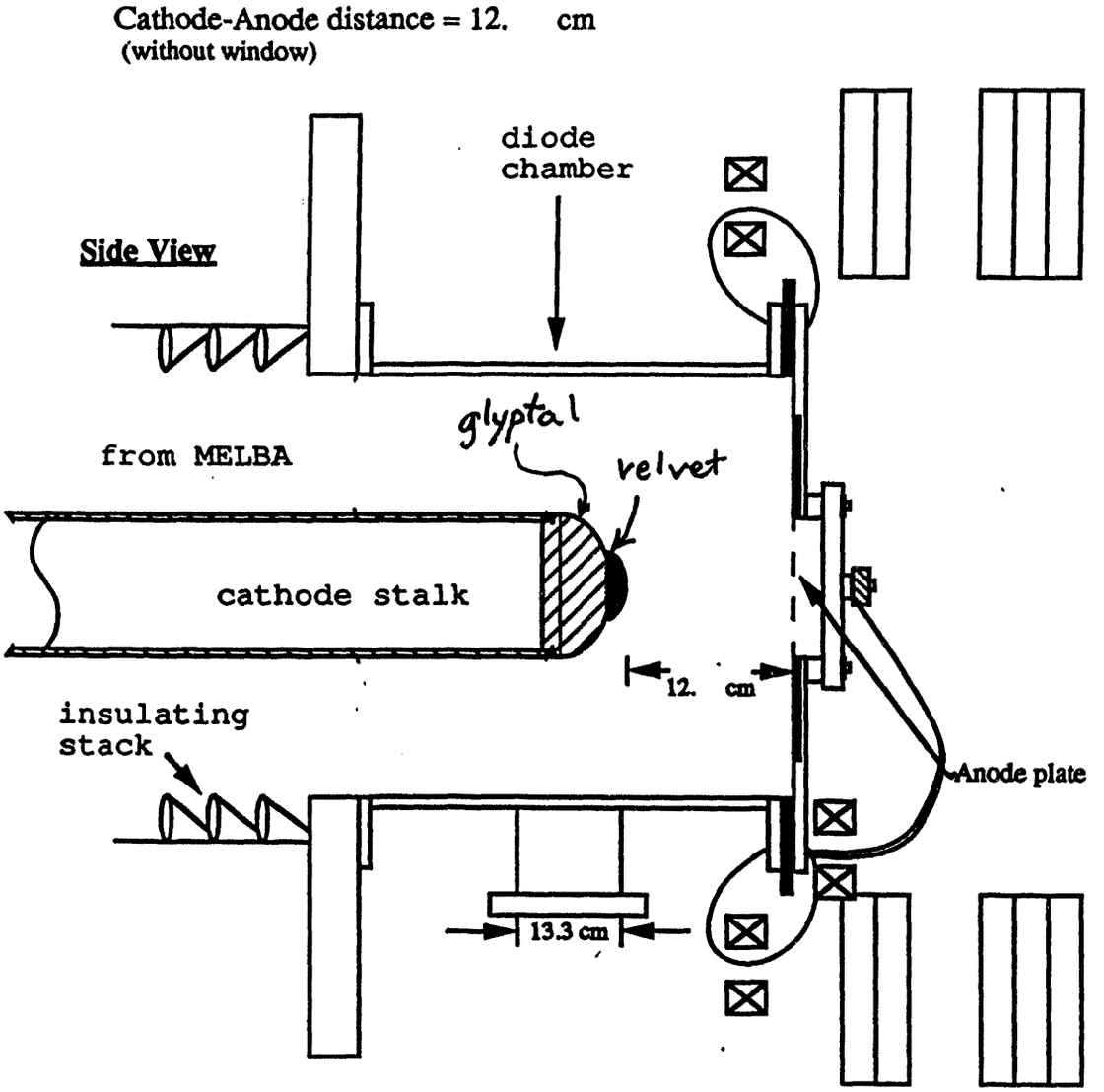

Figure 5-1 Cathode B

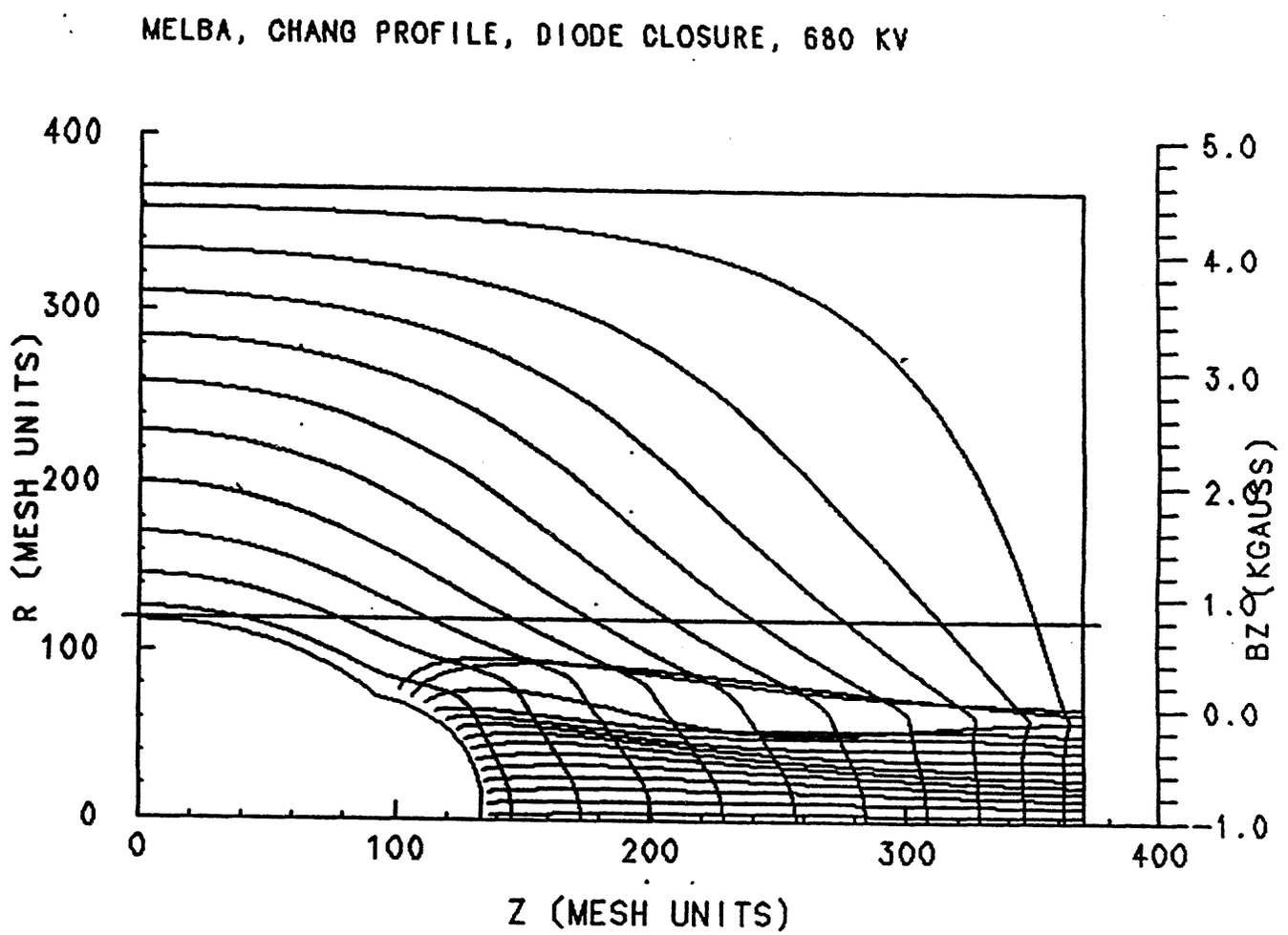

Figure 5-2. Cathode B with Uniform B field

(Converged) Gradient

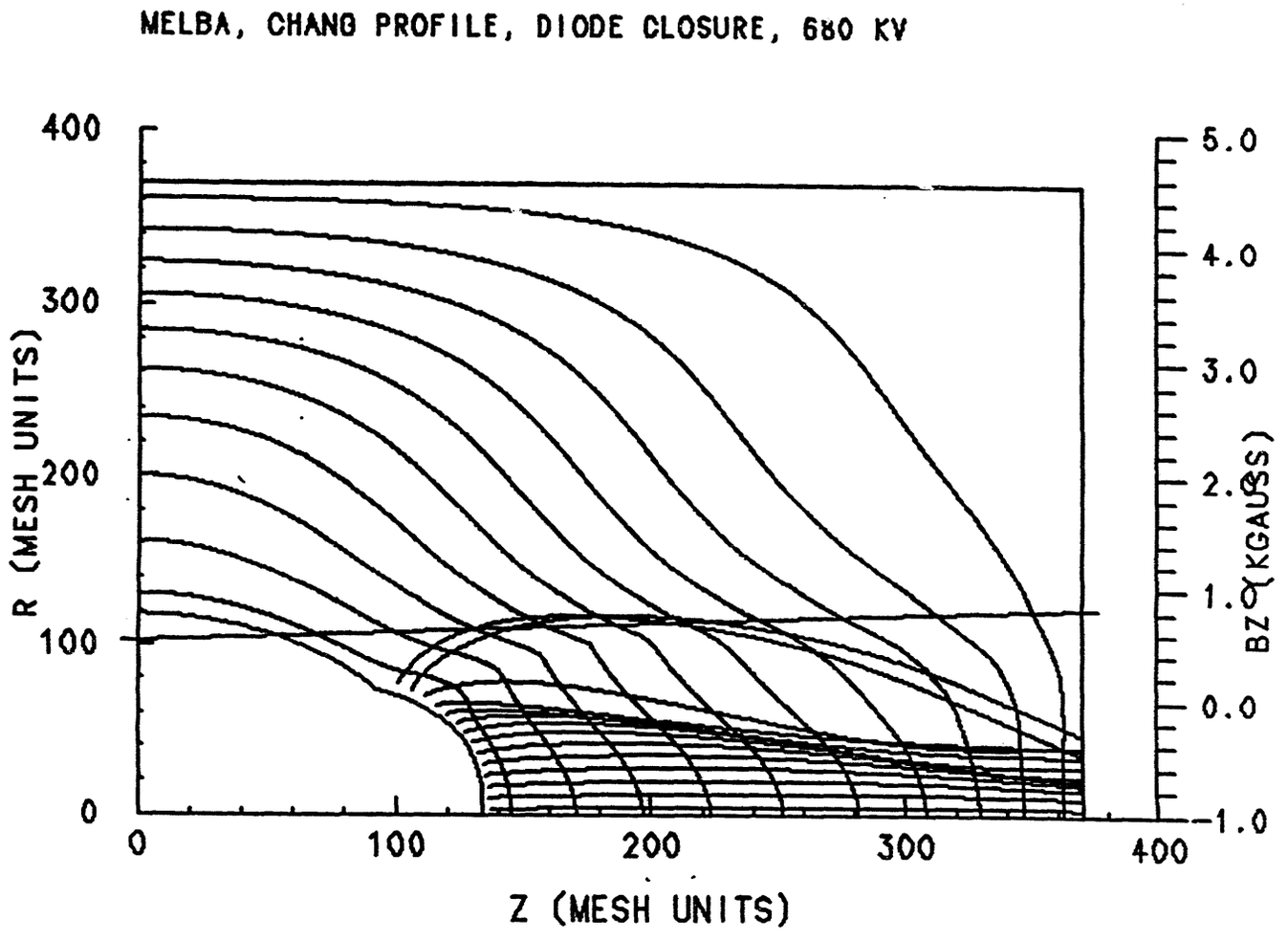

Figure 5-3. Cathode B with Gradient B-field

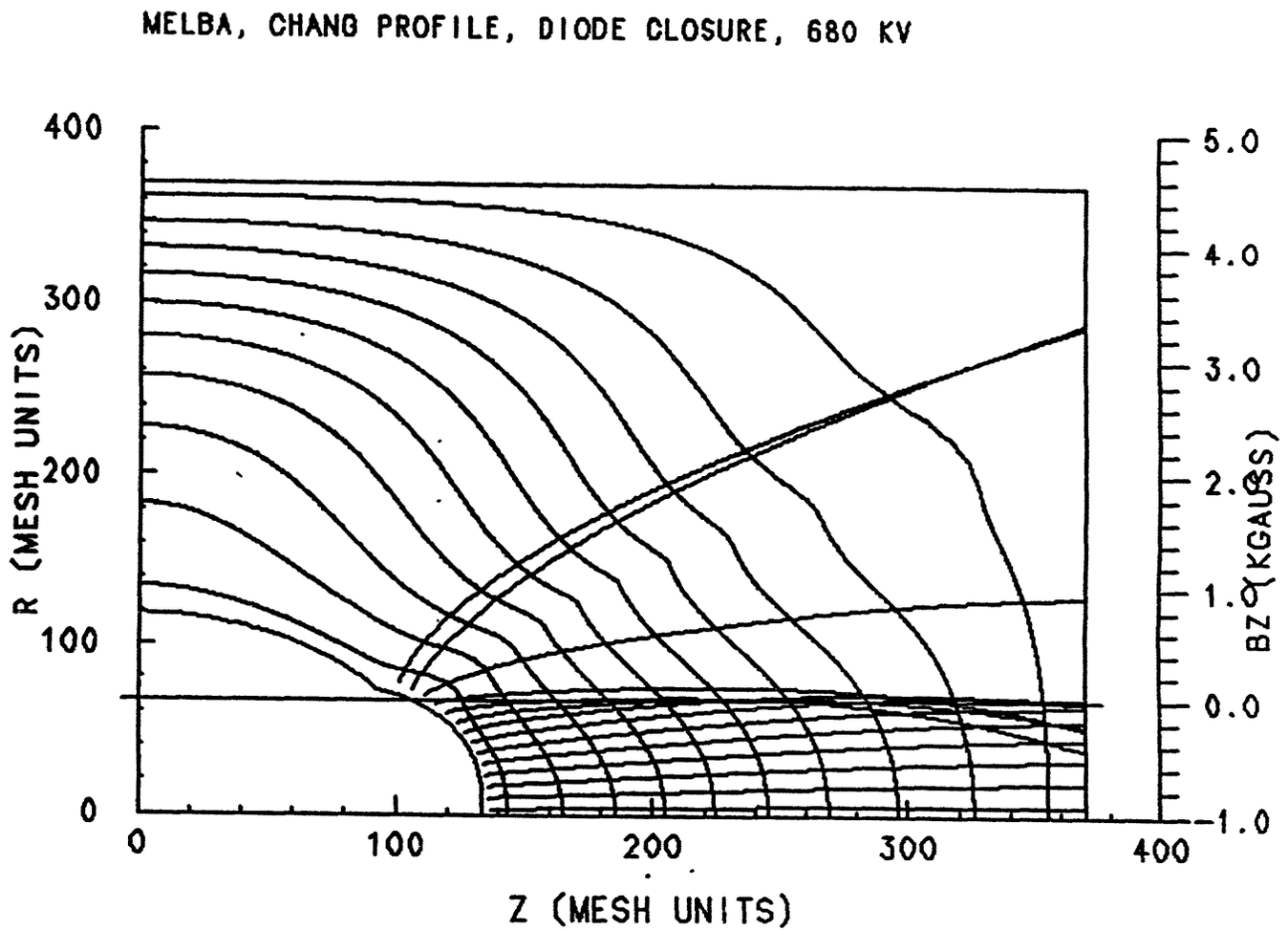

Figure 5-4 Cathode B, Unmagnetized

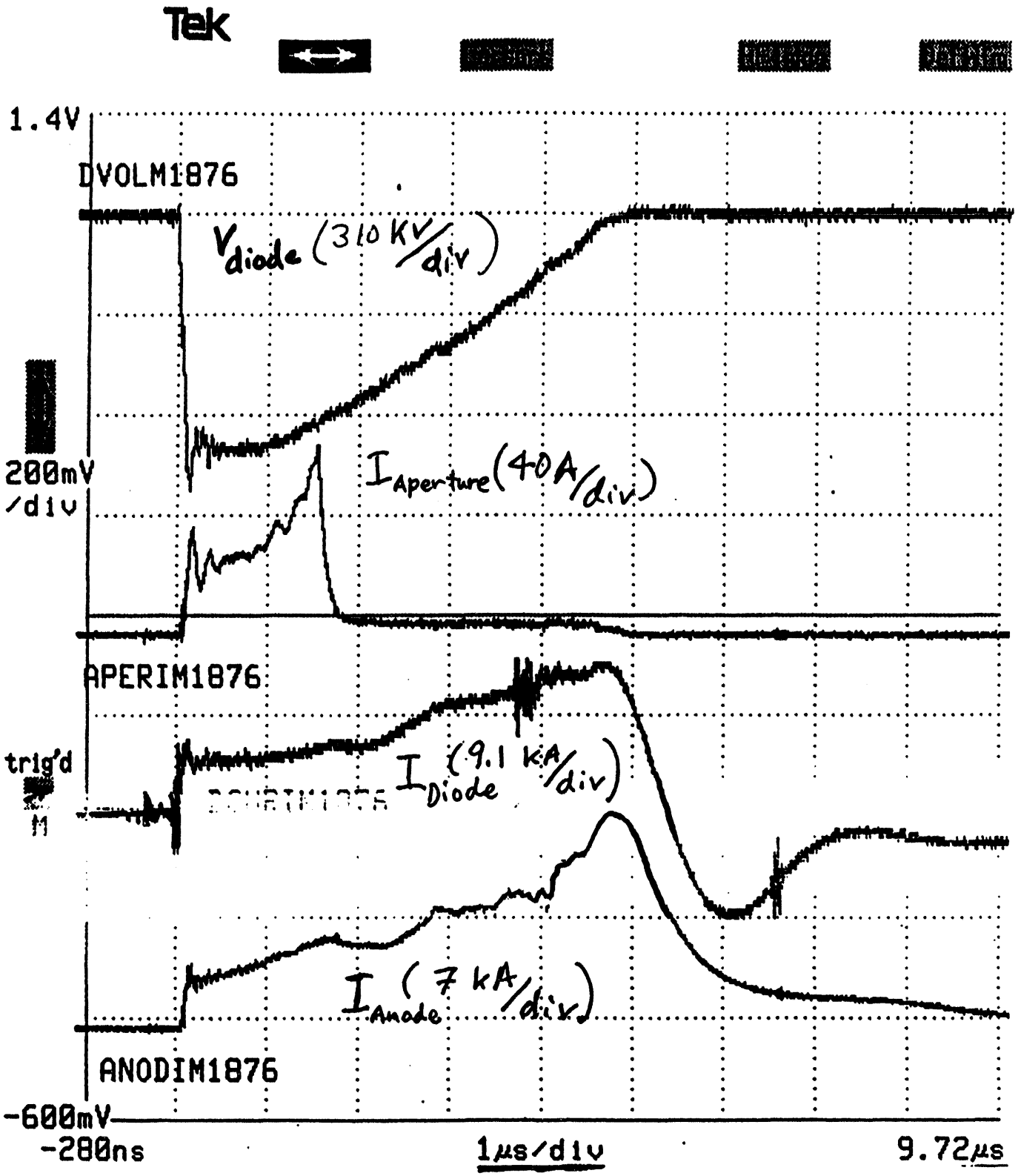

Figure 5-5 Cathode B with Gradient B

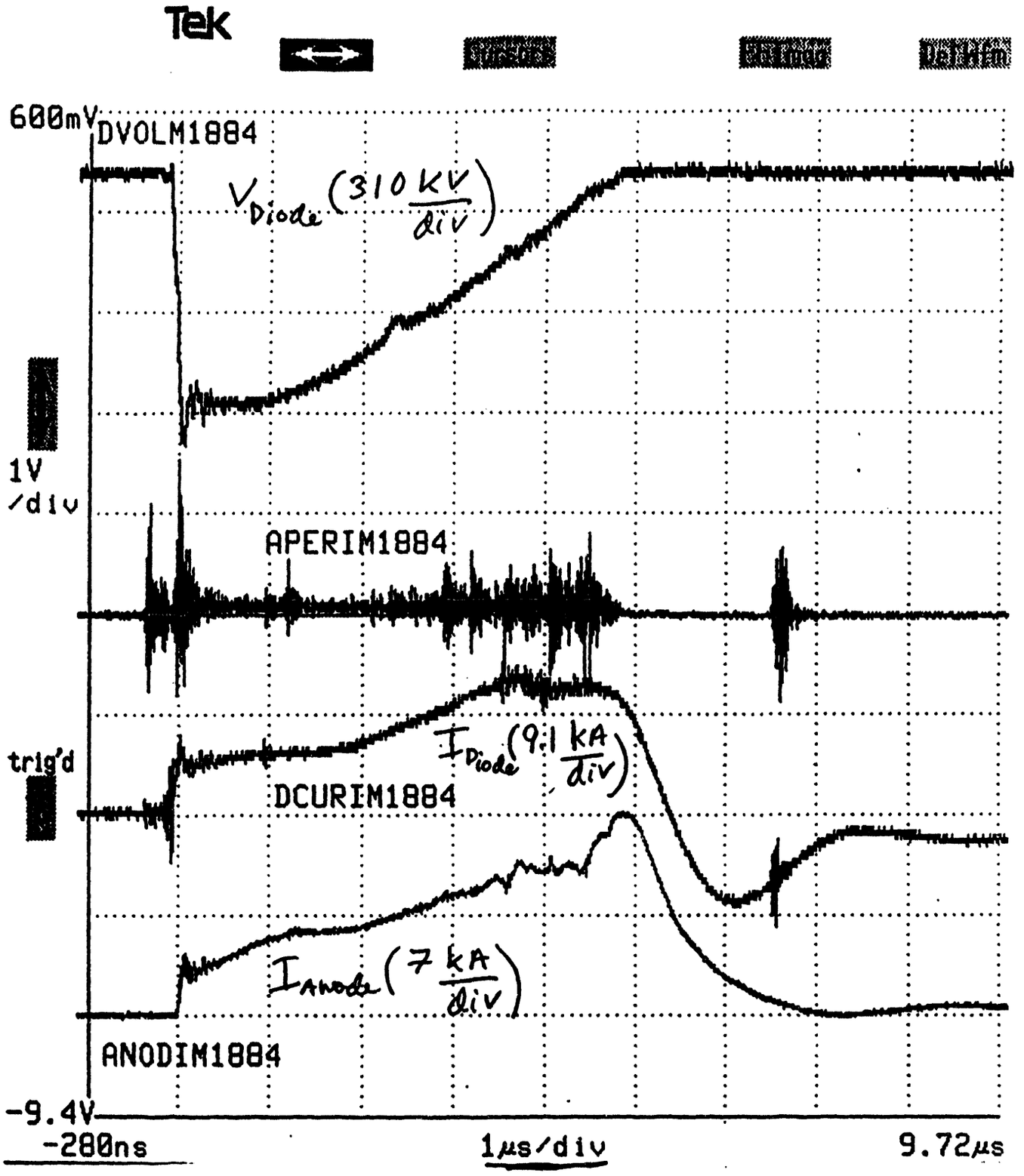

Figure 5-6 Cathode B with Uniform B

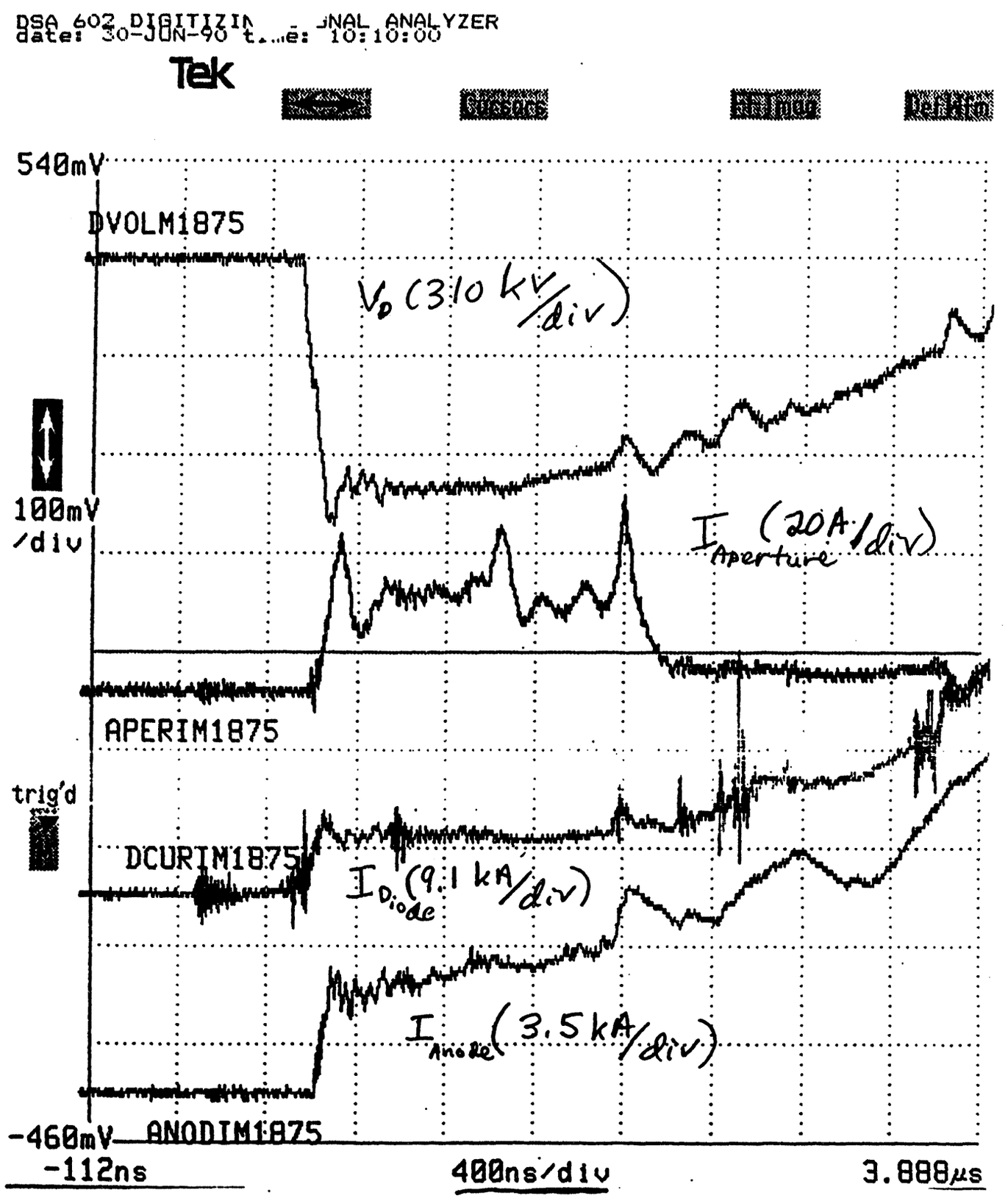

Figure 5-7 Cathode B with Unmagnetized diode

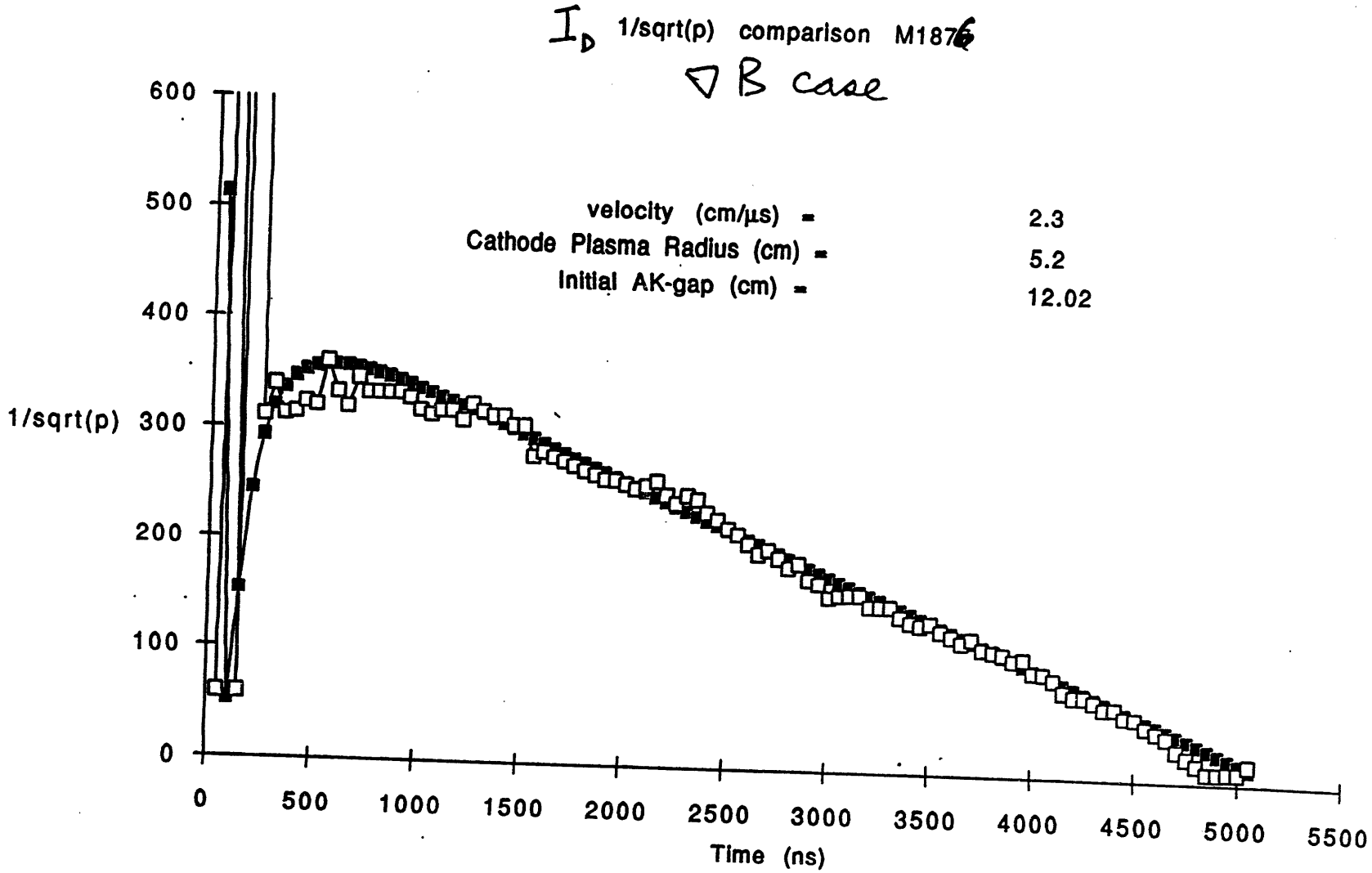

Figure 5-8 Cathode B with Gradient Magnetic Field

Cathode B

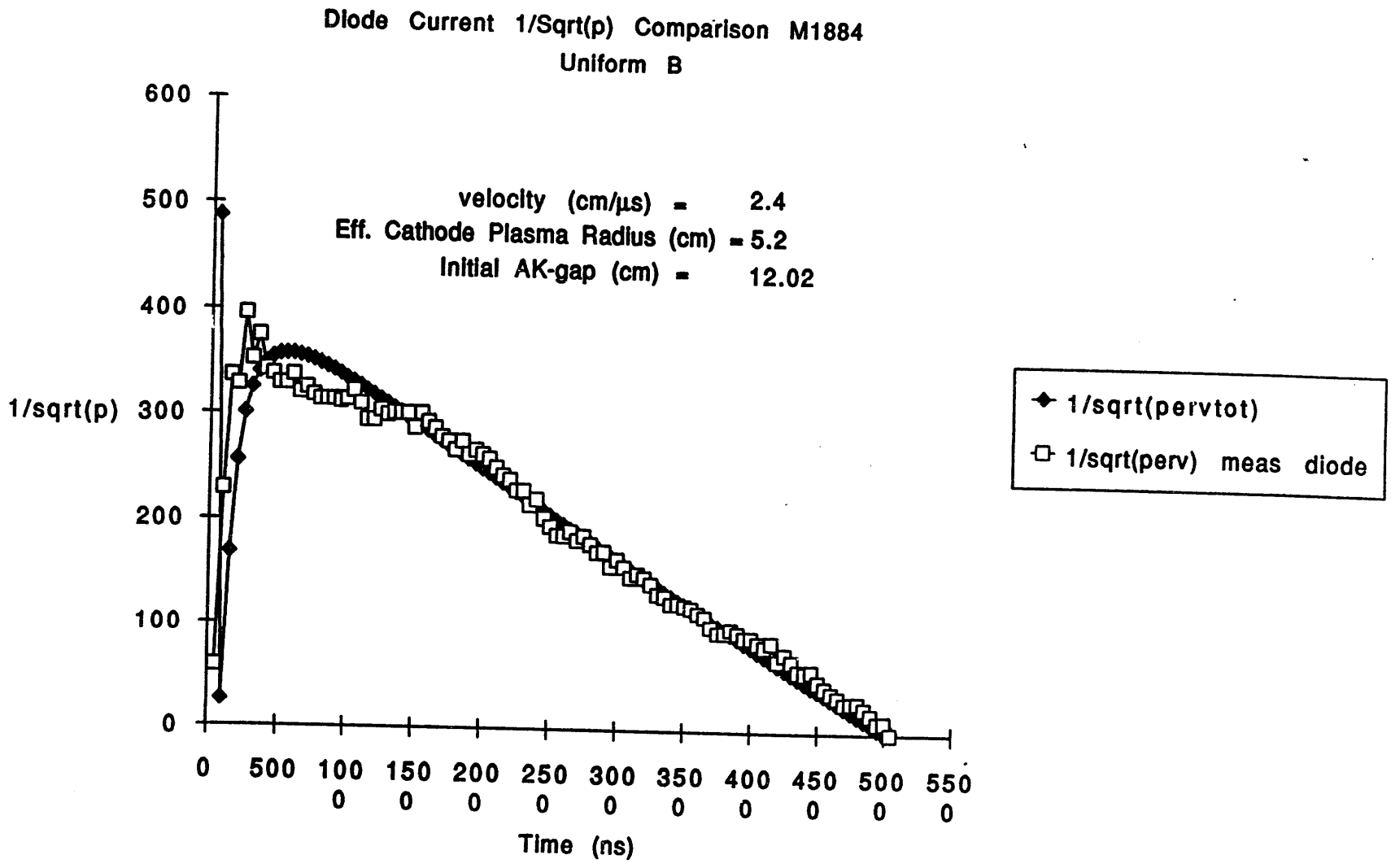

Figure 5-9

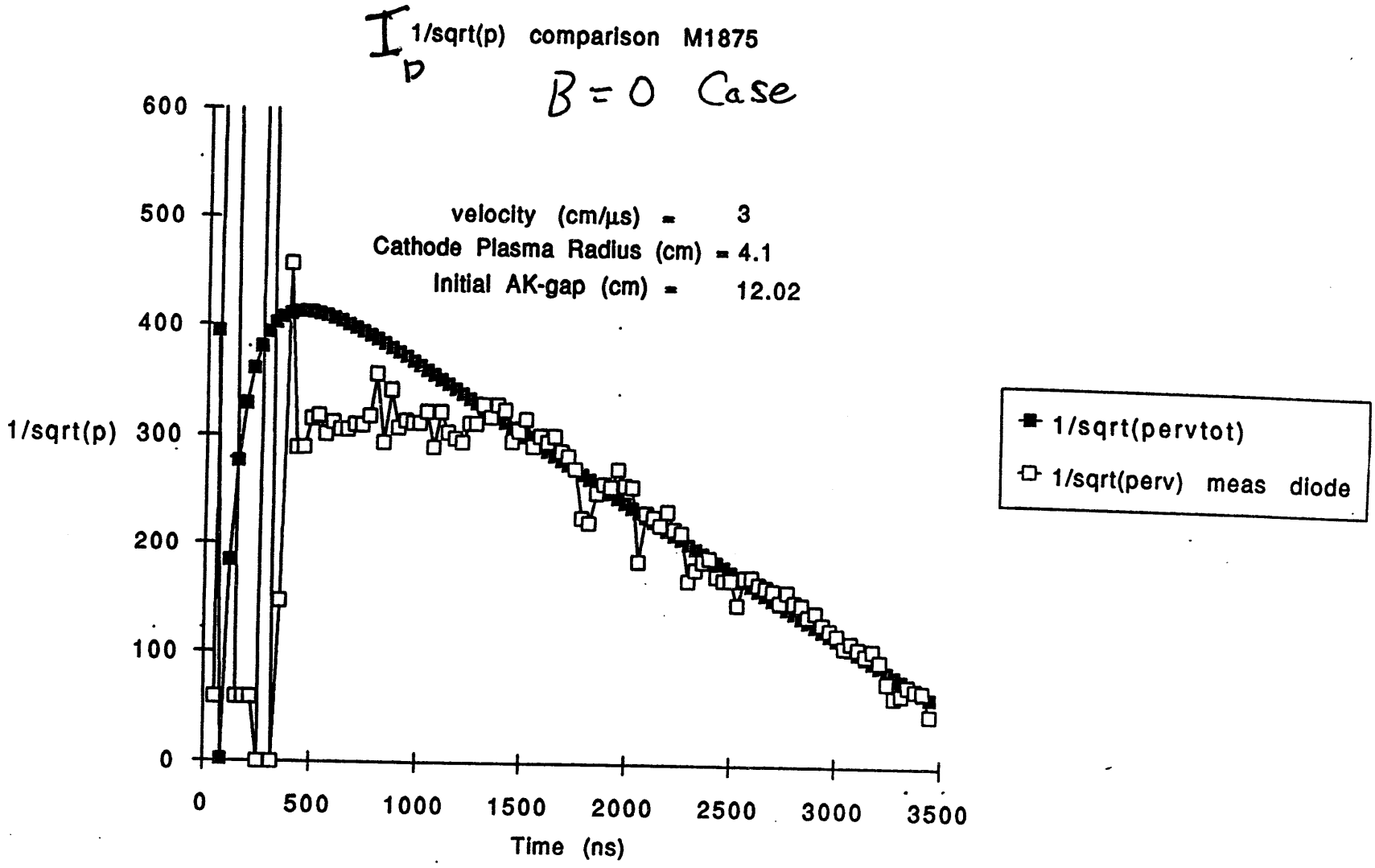

Figure 5-10. Cathode B with No Magnetic Field

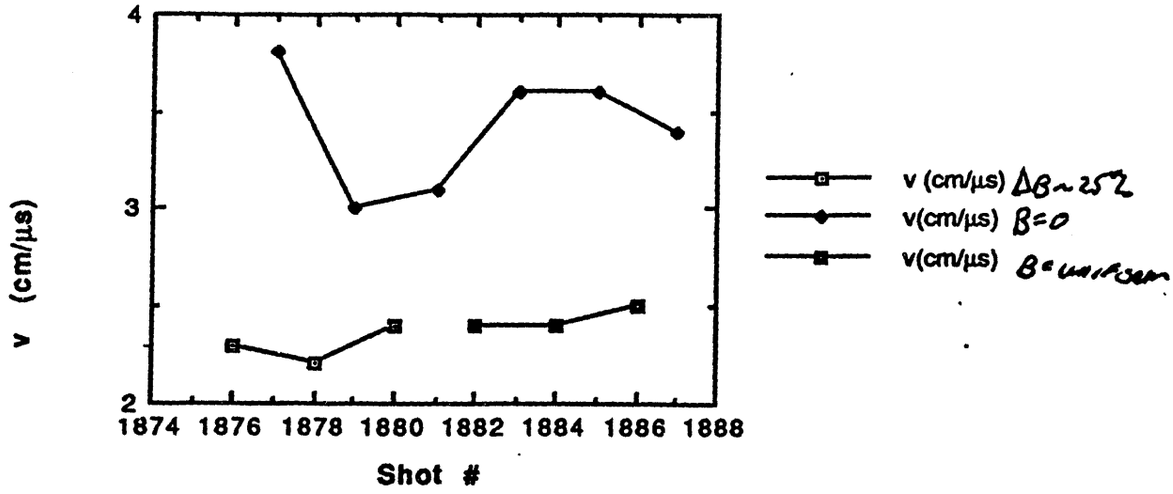

Figure 5-11 Summarized Data for cathode B

Diode

Power M1876

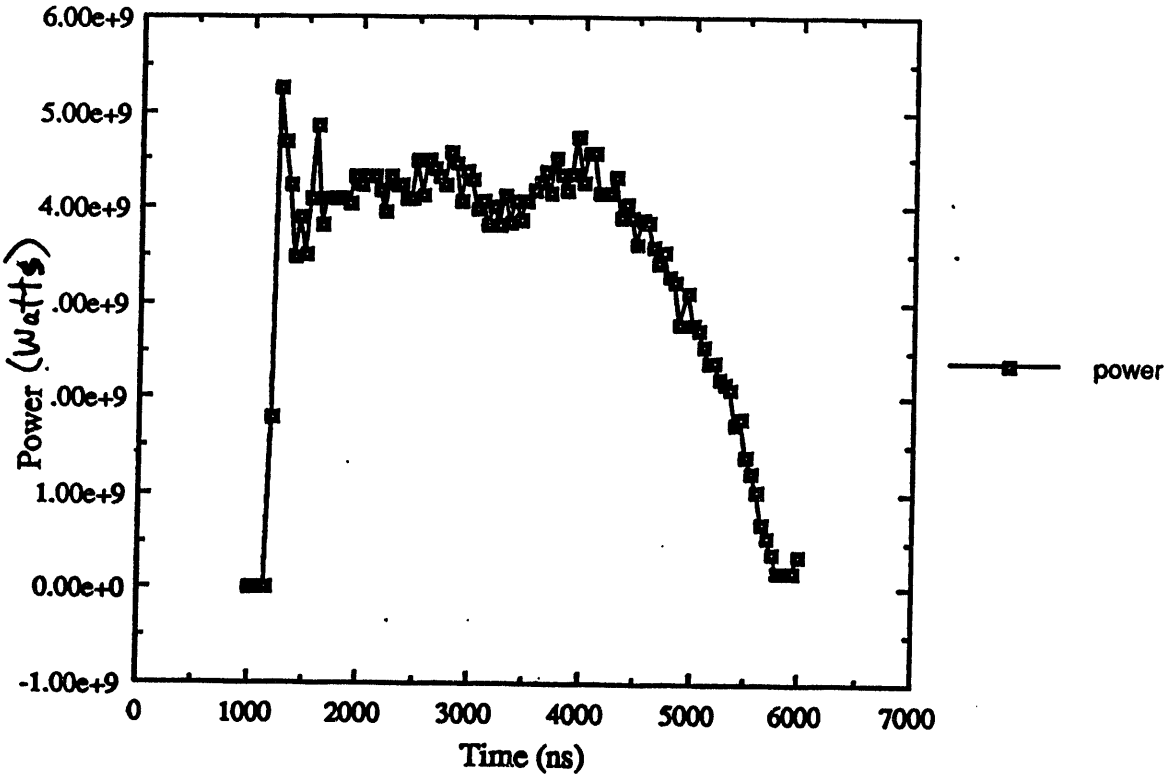

Figure 5-12 Cathode B, e-beam power

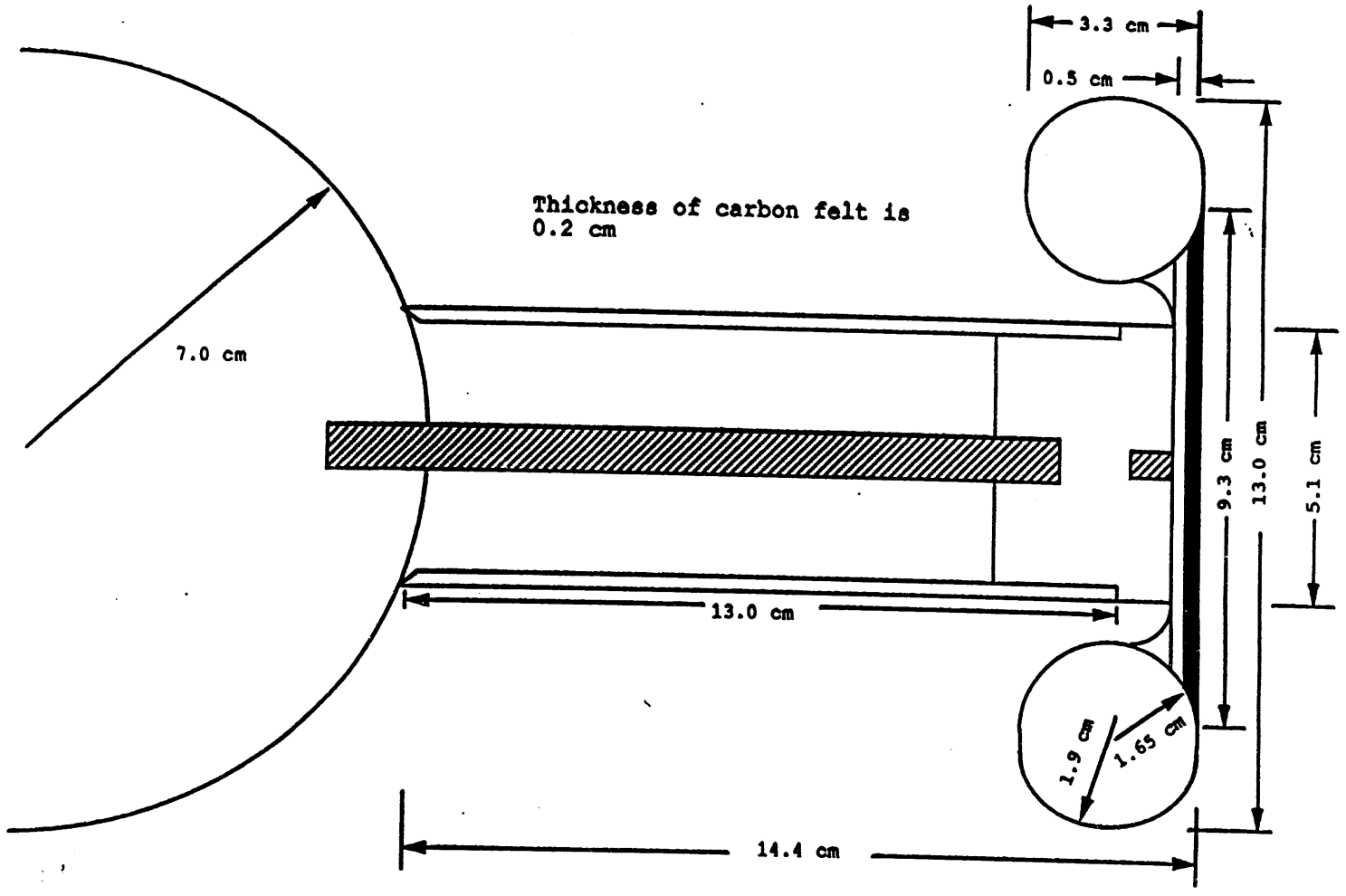

Drawing of a new planar cathode
(C) with a toroidal guard ring

Figure 5-13

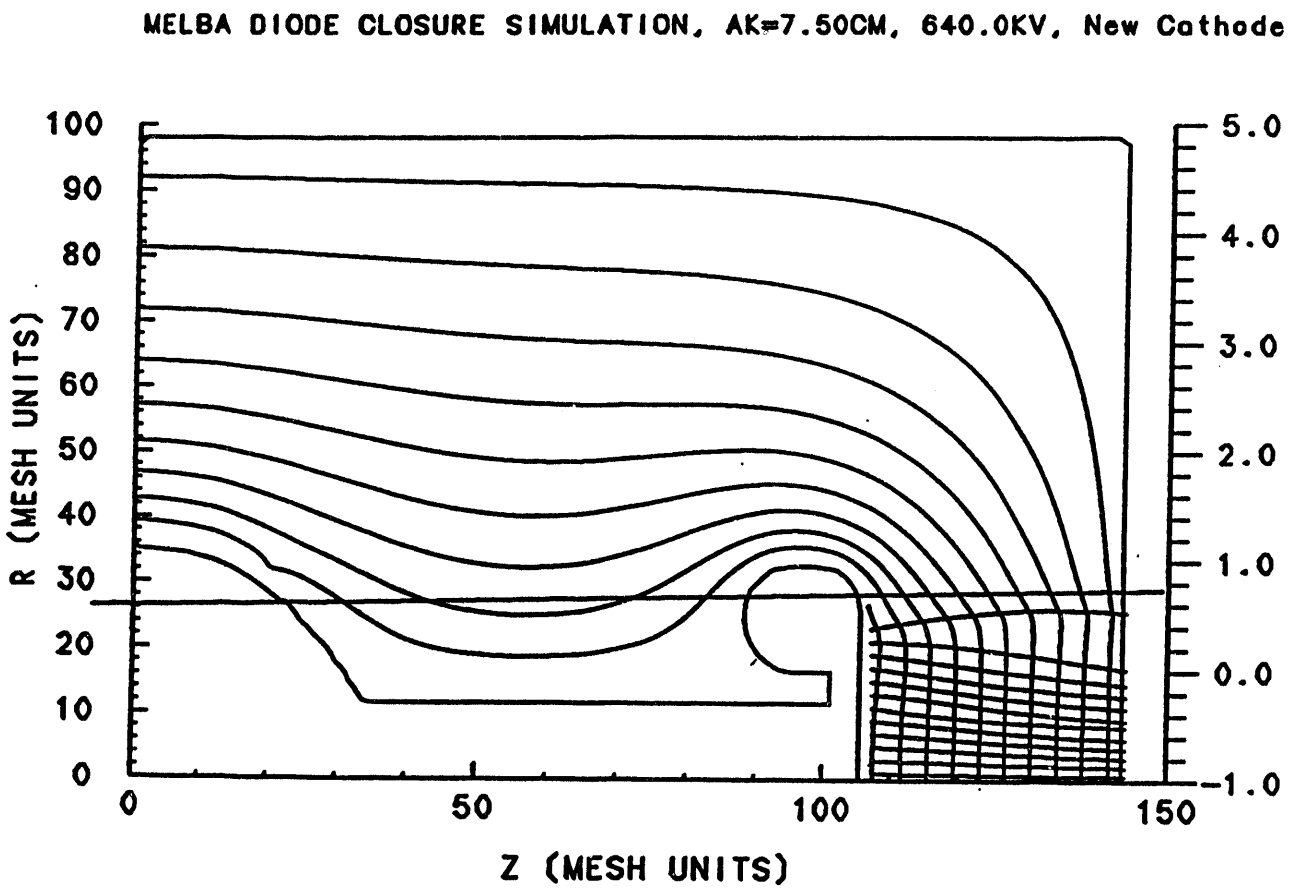
MELBA DIODE CLOSURE SIMULATION, AK=7.50CM, 640.0KV, New Cathode C
R (MESH UNITS)
Z (MESH UNITS)
100
90
80
70
60
50
40
30
20
10
0
0
50
100
150
5.0
4.0
3.0
2.0
1.0
0.0
-1.0

Figure 5-14

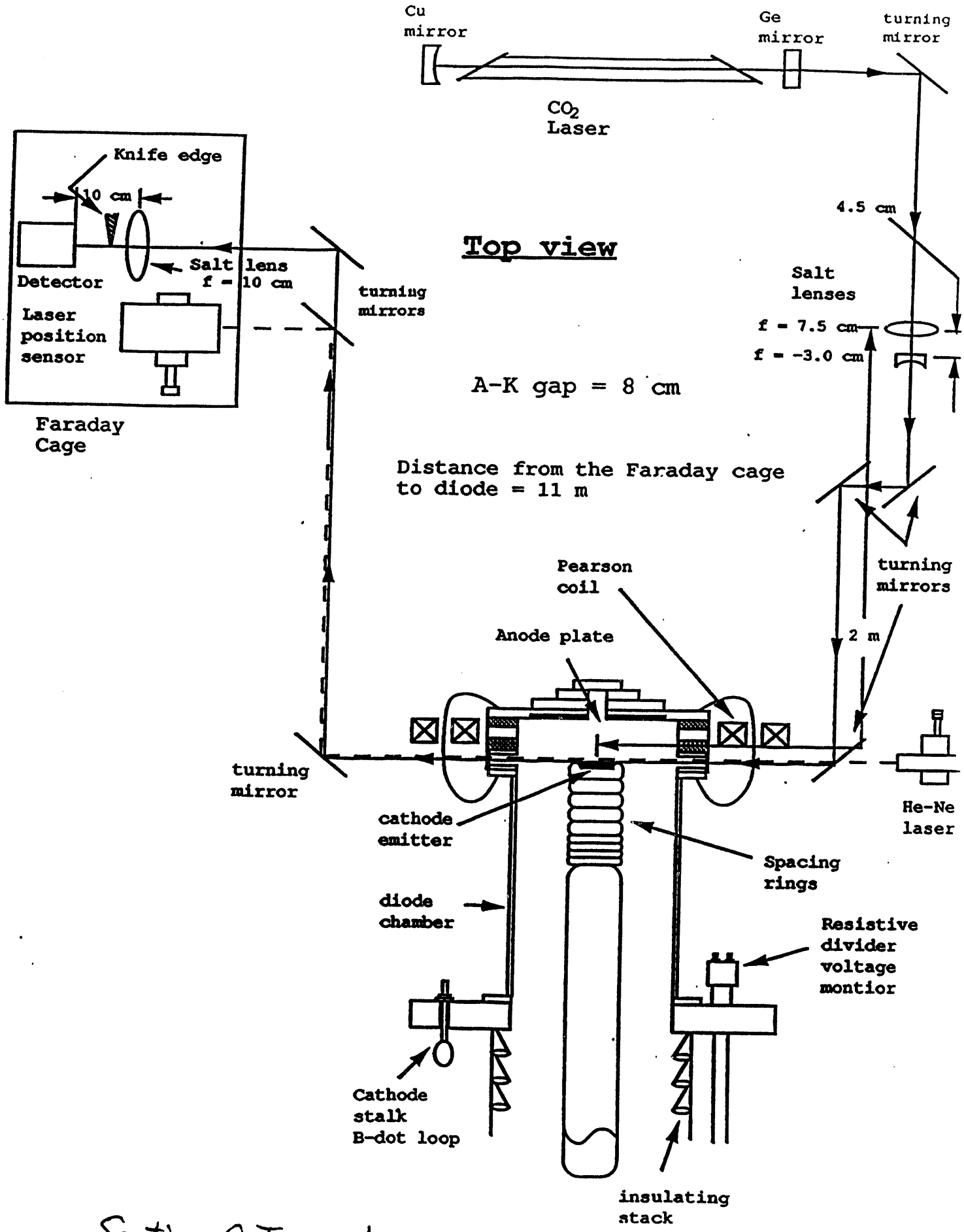

Section 6, Figure 1

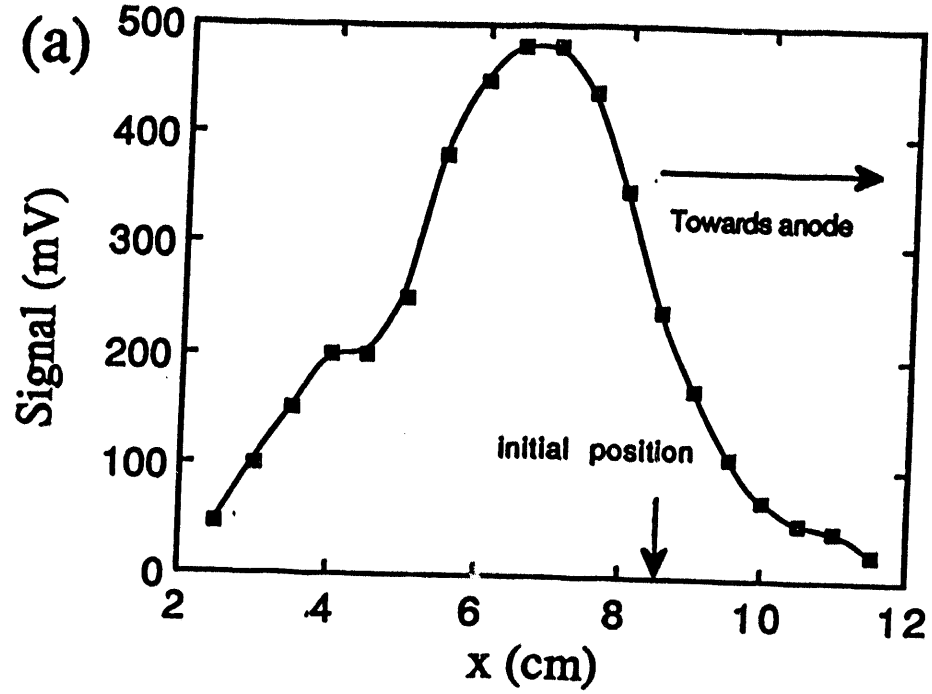

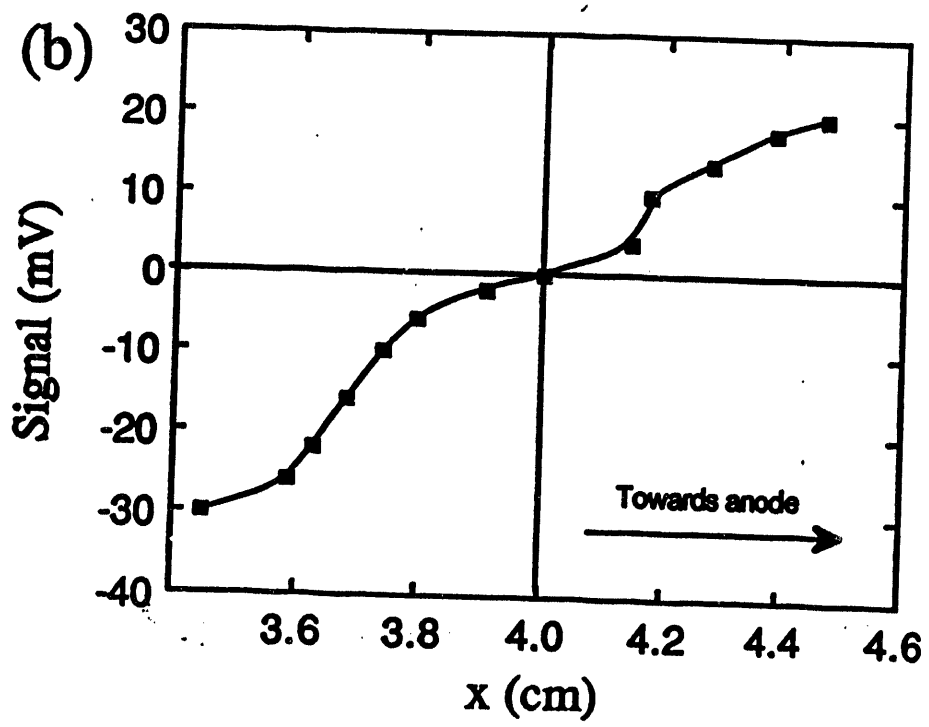

Section 6, Figure 2

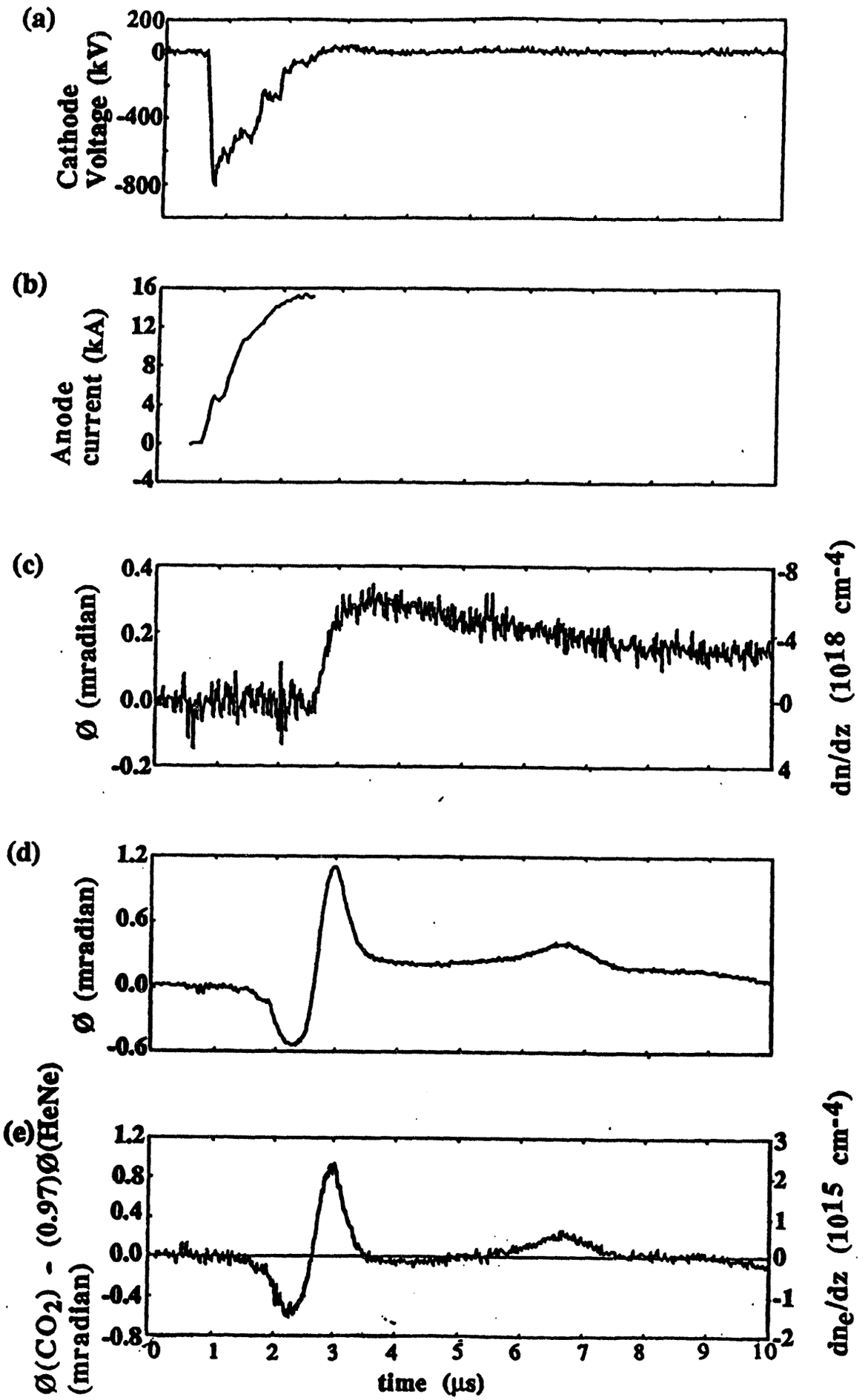
(a)
Cathode Voltage (kV)
200
0
-400
-800
(b)
Anode current (kA)
16
12
8
4
0
-4
(c)
Ø (mradian)
0.4
0.2
0.0
-0.2
dn/dz (10^18 cm^-4)
-8
-4
0
4
(d)
Ø (mradian)
1.2
0.6
0.0
-0.6
(e)
Ø(CO2) - (0.97)Ø(HeNe) (mradian)
1.2
0.8
0.4
0.0
-0.4
-0.8
dne/dz (10^15 cm^-4)
3
2
1
0
-1
-2
0 1 2 3 4 5 6 7 8 9 10
time (μs)

(a) z = 1.5 cm

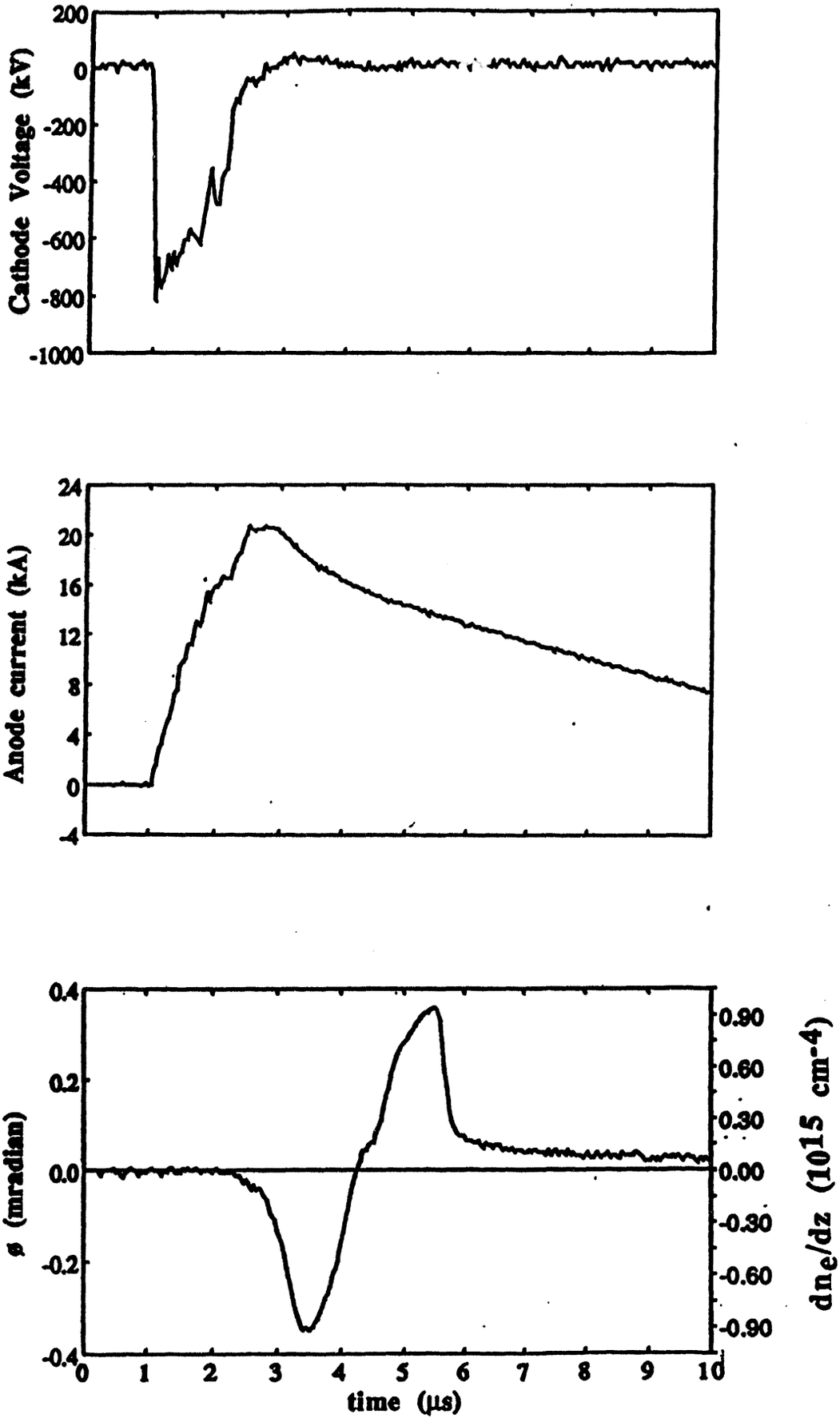

Section 6; Figure 4a

(b) z = 4.5 cm

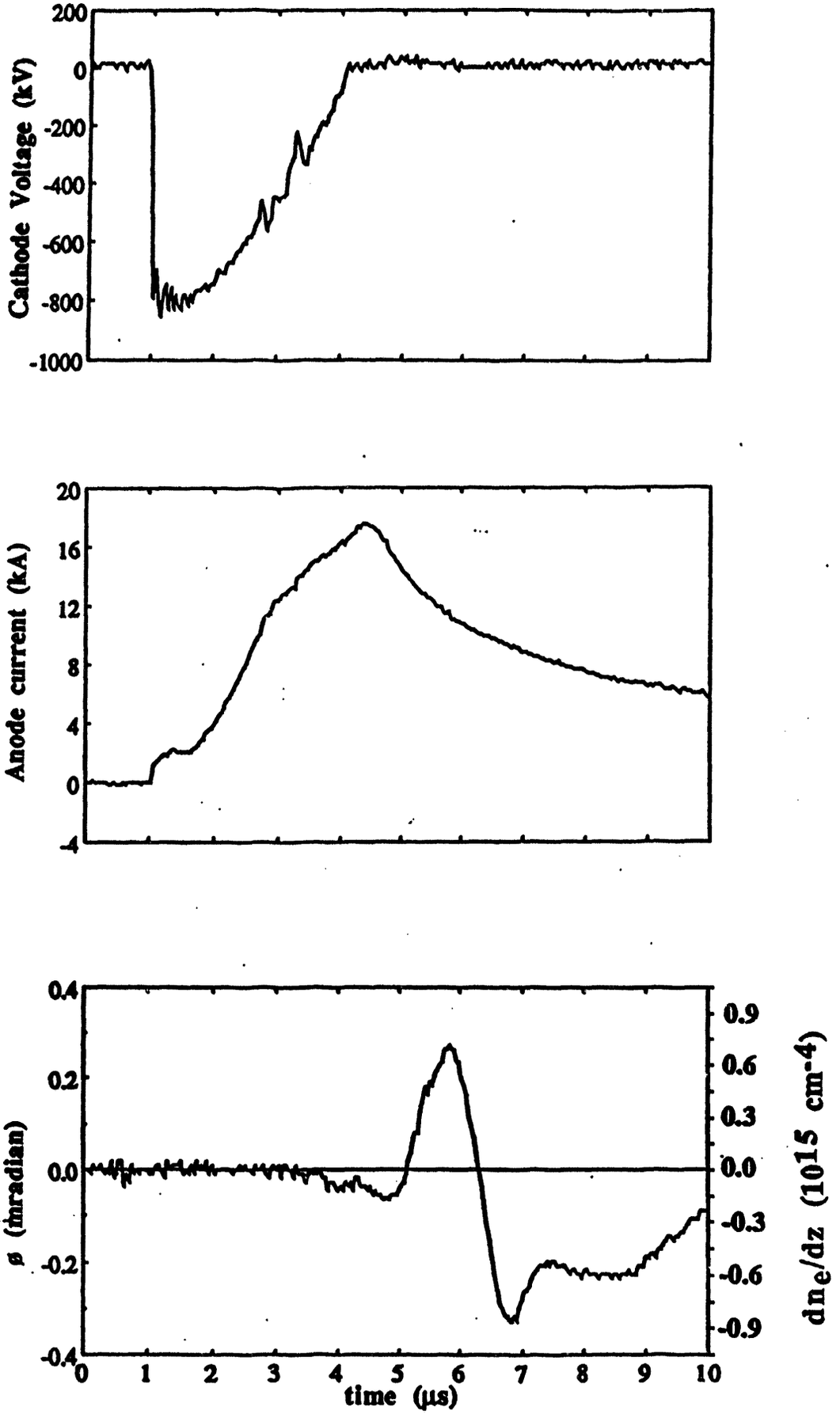

Section 6 ; Figure 4b

(c) z = 7.5 cm

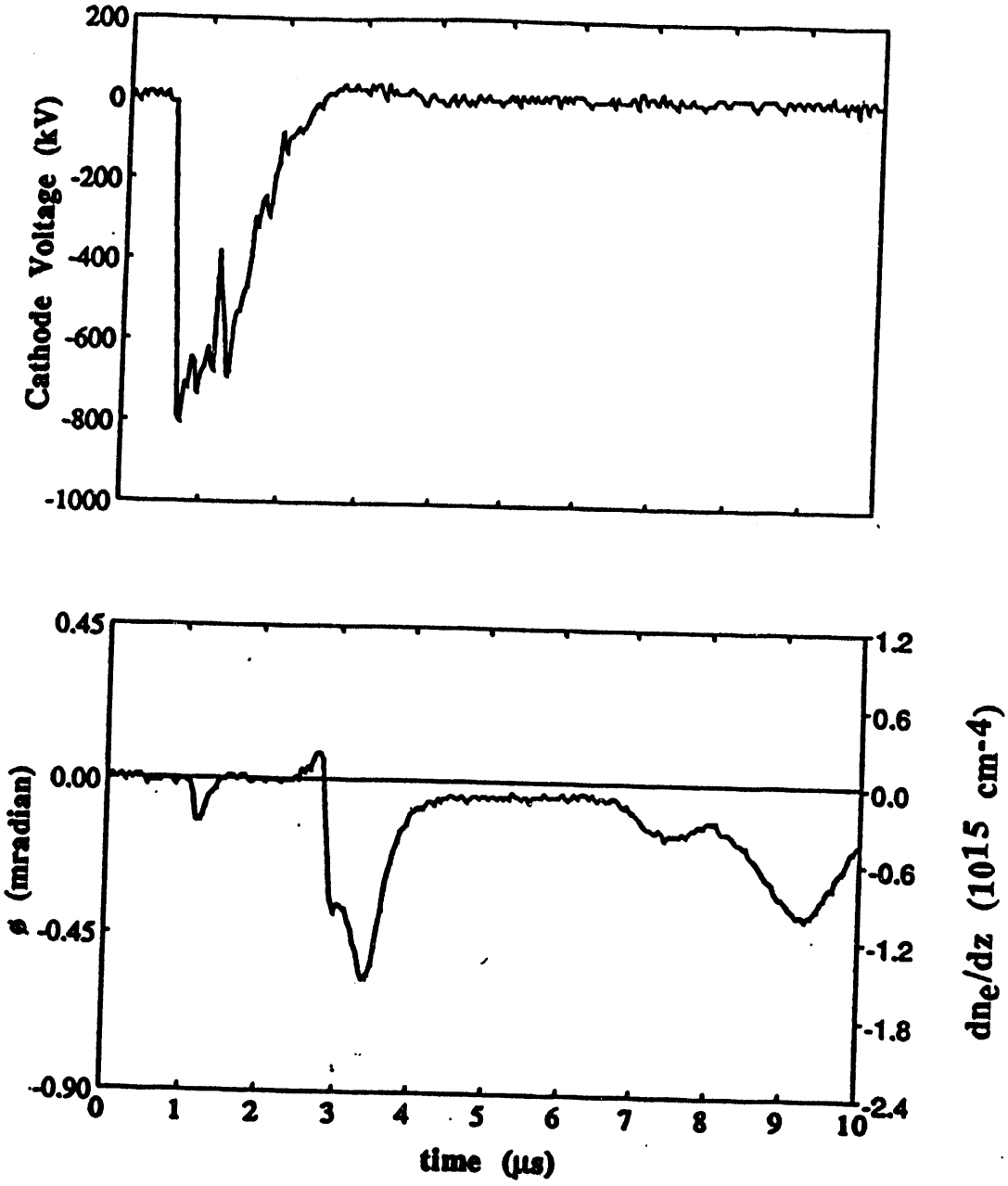

Section 6; Figure 4c

(d) z = 1.5 cm

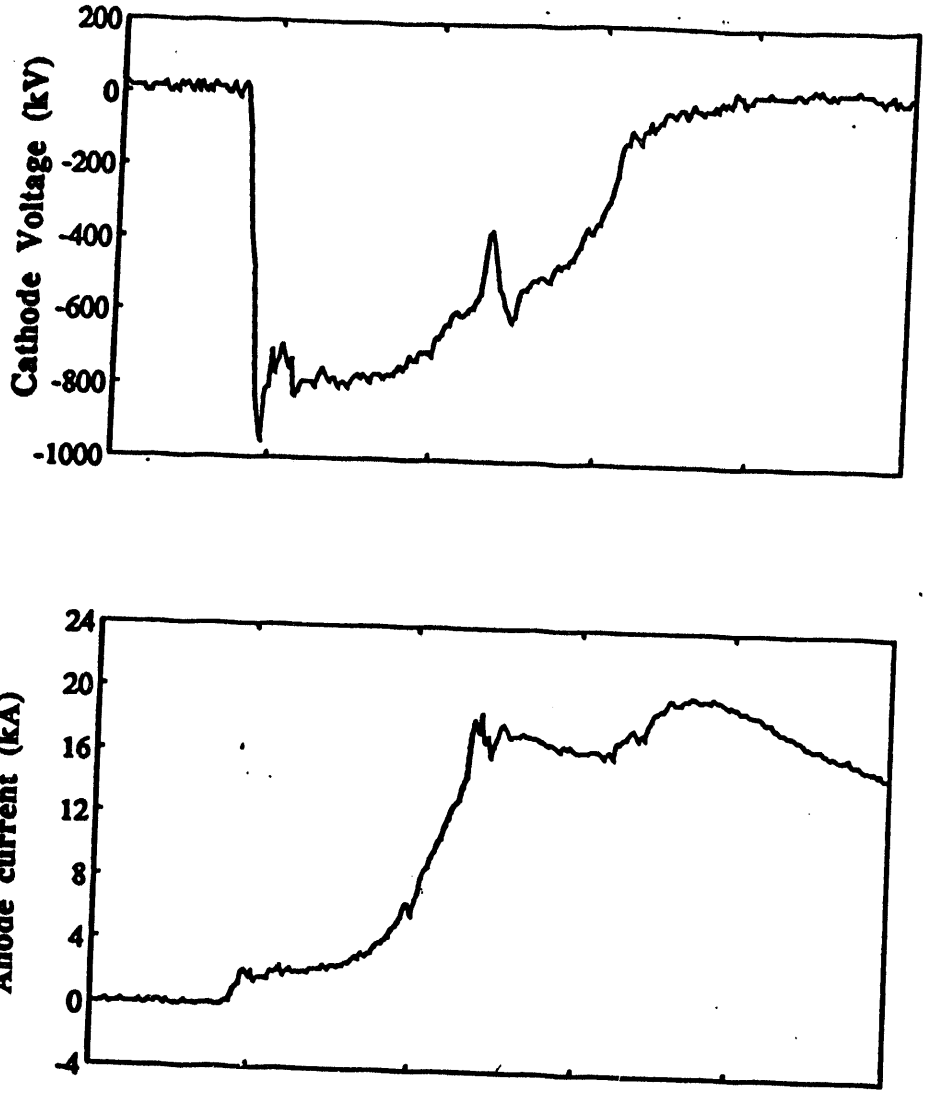

Section 6; Figure 4d

(e) z = 1.5 cm

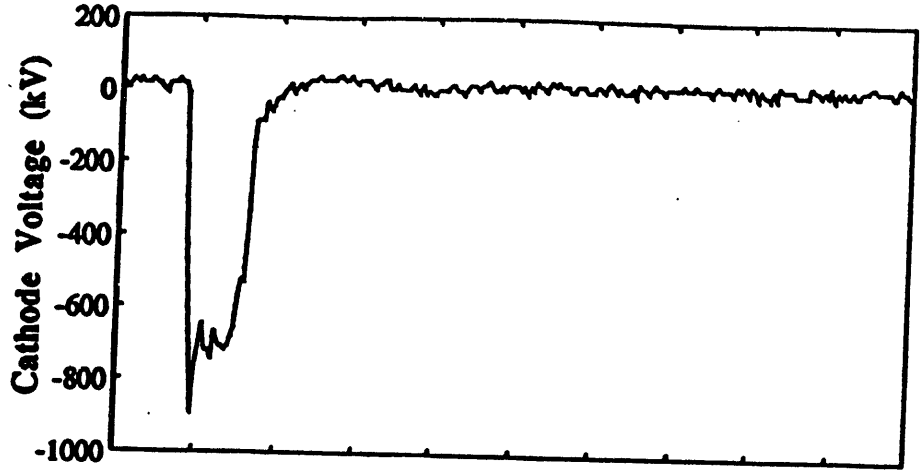

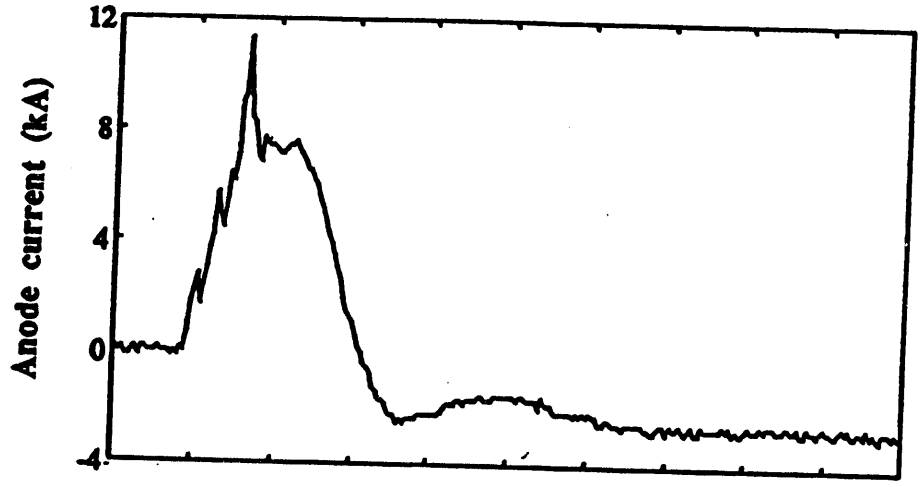

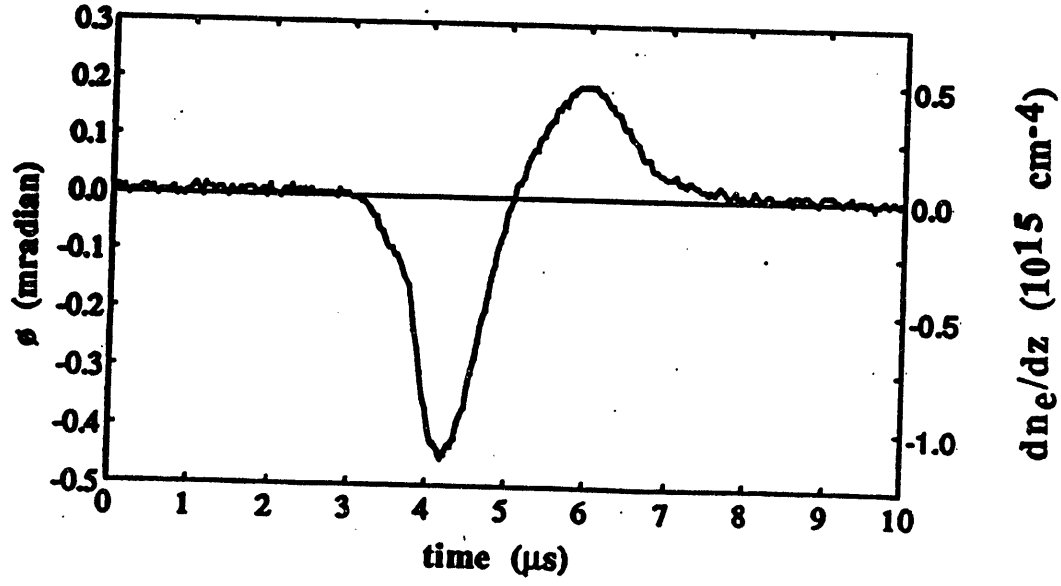

Section 6; Figure 4e

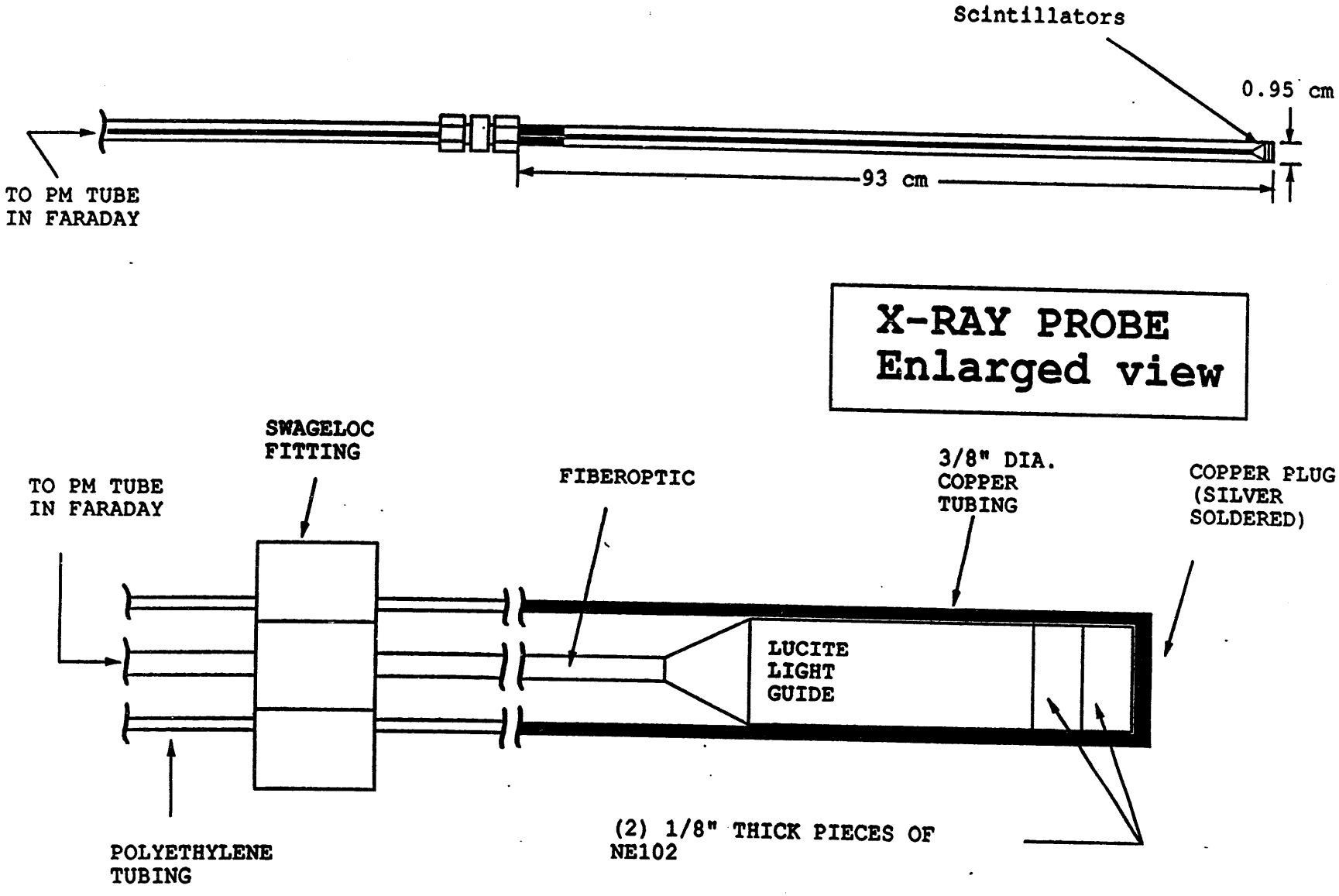

X-RAY PROBE

Figure 7-1

Experimental configuration for the X-ray probe experiment at the University of Michigan

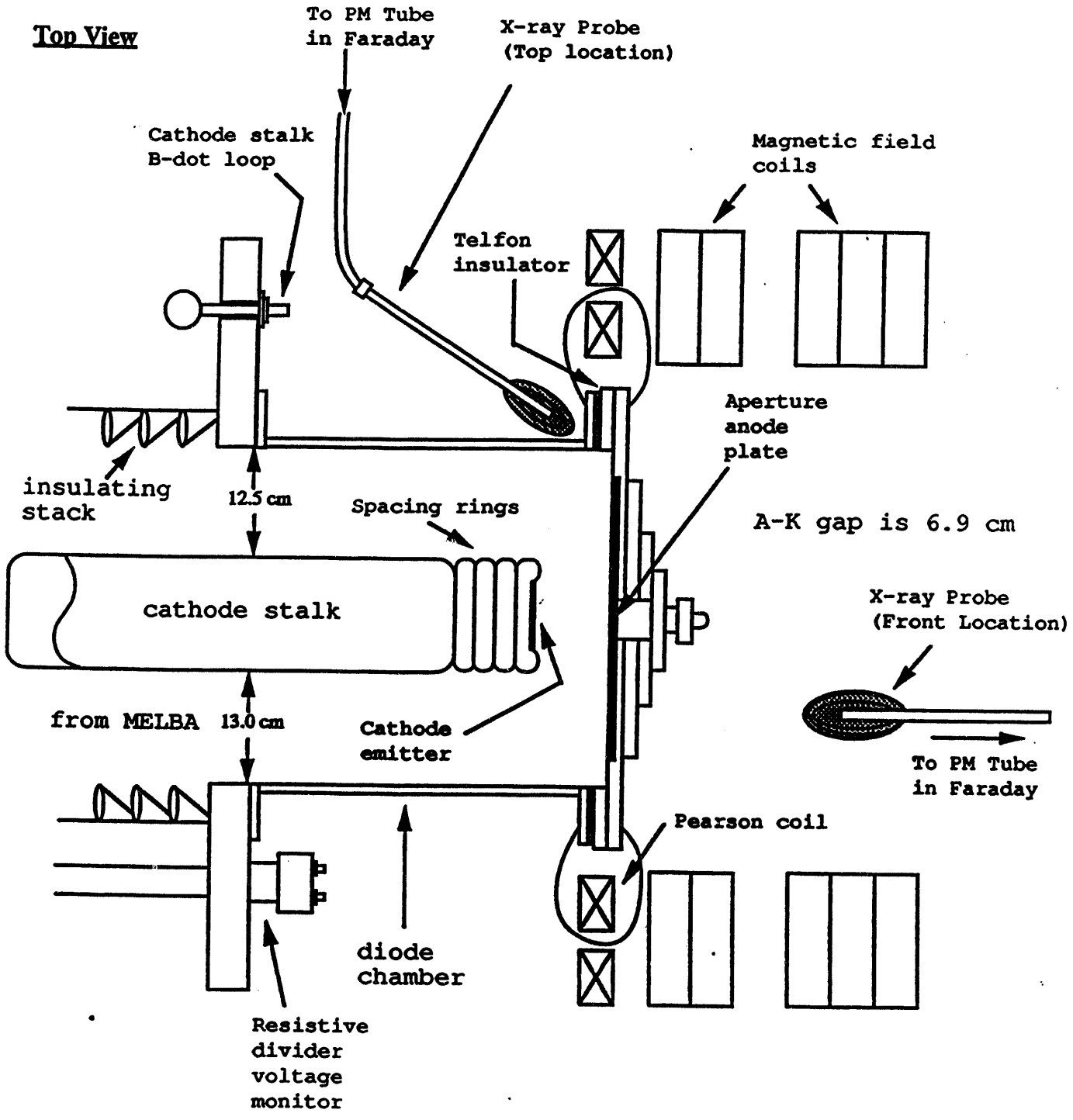

Figure. 7-2

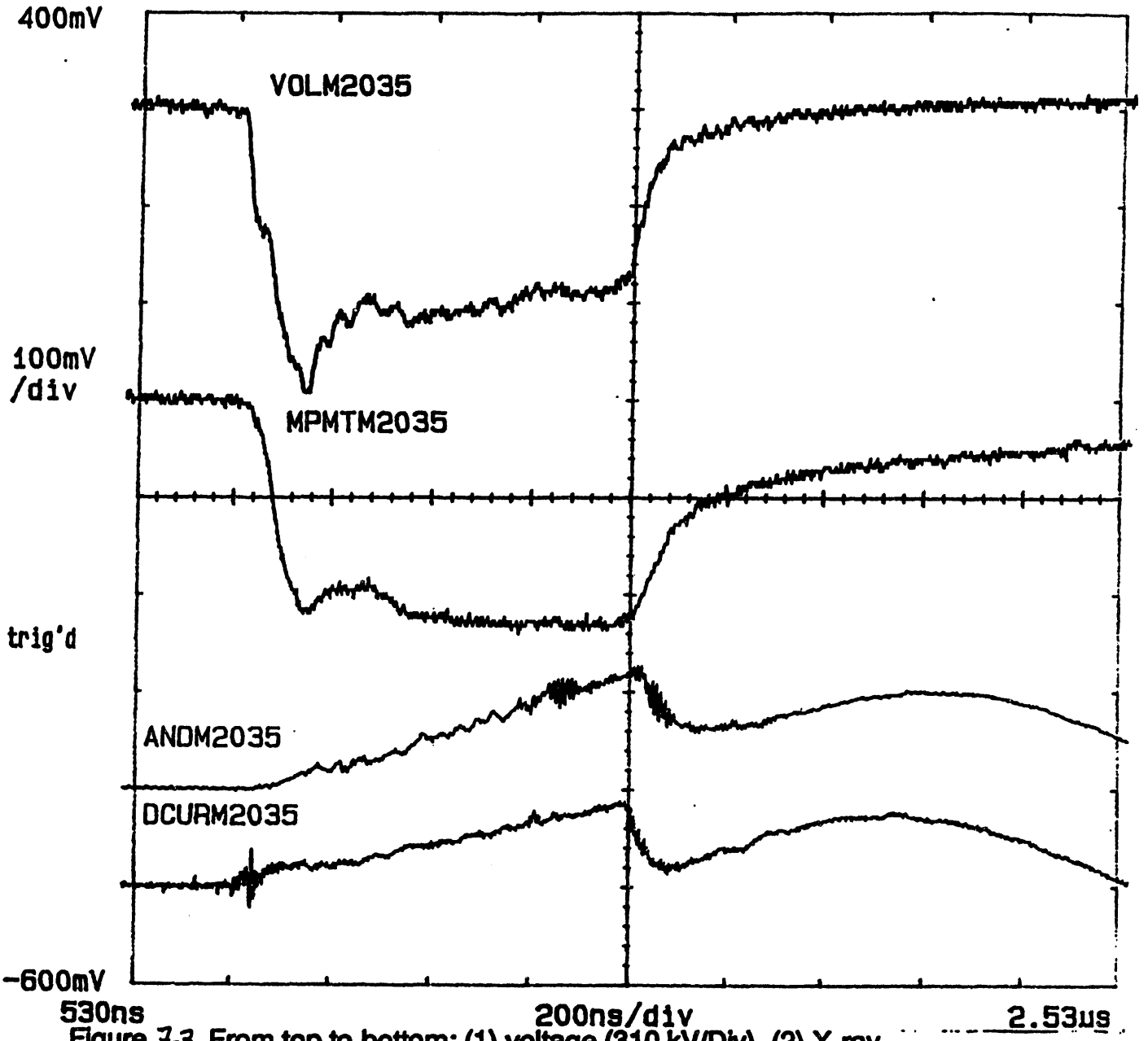

Figure 7-3 From top to bottom: (1) voltage (310 kV/Div), (2) X-ray signal (100 mV/Div) [The X-ray probe is on top of the diode region covered with 3 sheets of lead], (3) current (anode) (14 kA/Div), (4) current (diode) (22.7 kA/Div).

DSA 602 DIGITIZING SIGNAL ANALYZER
date: 5-SEP-90 time: 22: 12: 18

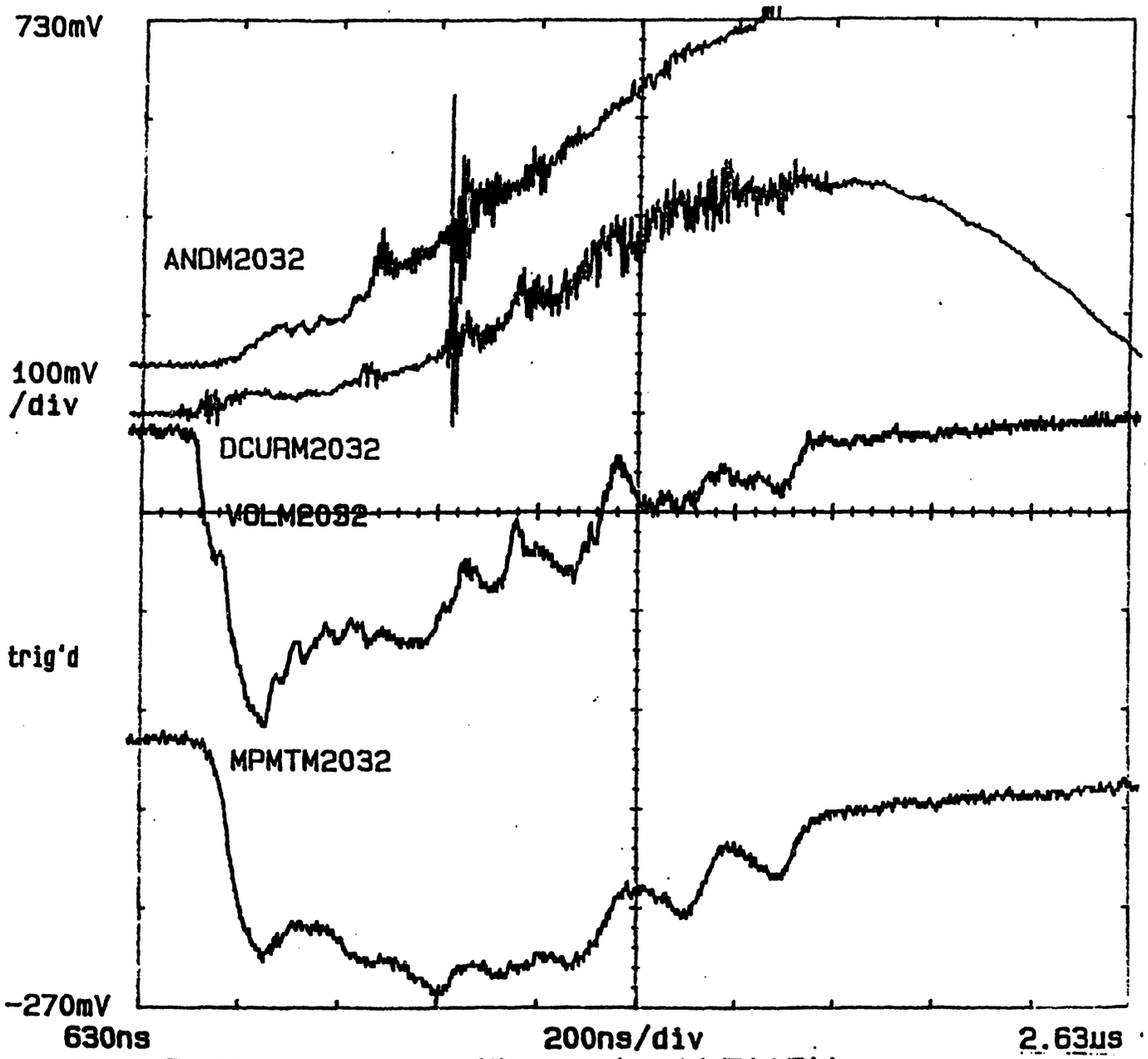

Figure.~~7~~-4 From top to bottom: (1) current (anode) (7 kA/Div), (2) current (diode) (22.7 kA/Div), (3) voltage (310 kV/Div), (4) X-ray signal (100 mV/Div) [The X-ray probe is on top of the diode region covered with 3 sheets of lead].

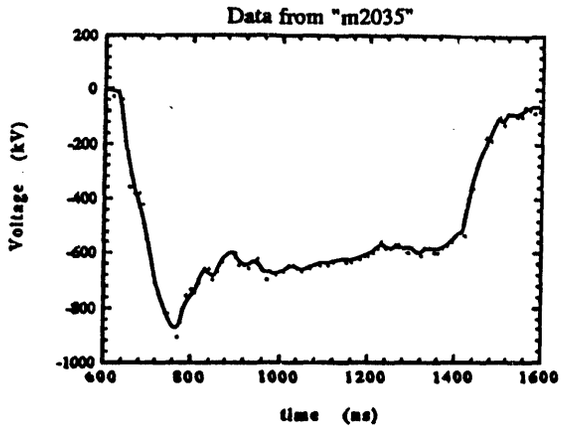
Data from "m2035"
Voltage (kV)
time (ns)

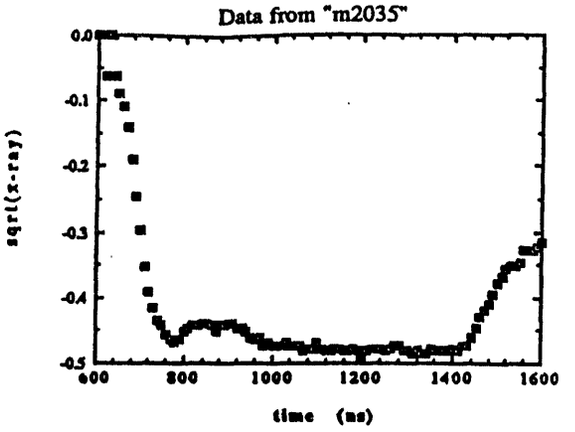
Data from "m2035"
sqrt(x-ray)
time (ns)

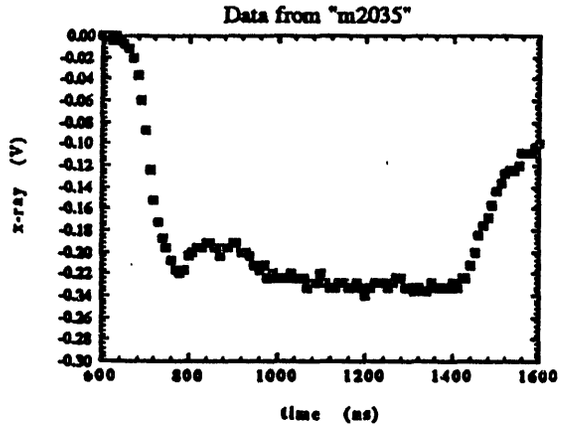
Data from "m2035"
x-ray (V)
time (ns)

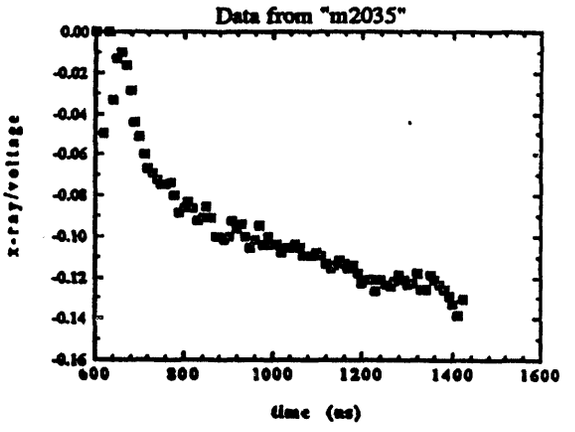
Data from "m2035"
x-ray/voltage
time (ns)

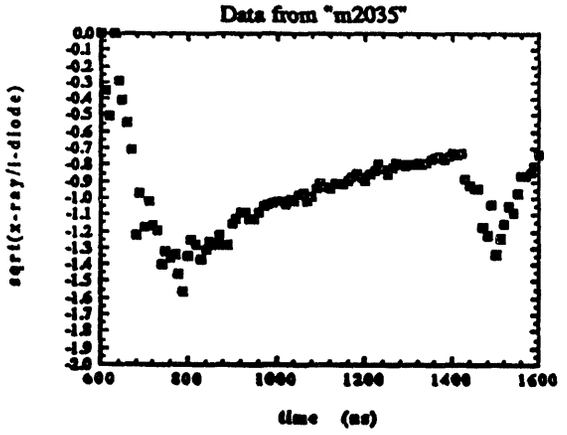
Data from "m2035"
sqrt(x-ray/i-diode)
time (ns)

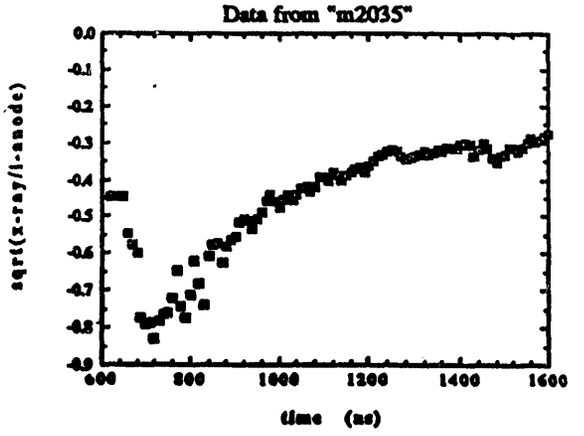
Data from "m2035"
sqrt(x-ray/i-anode)
time (ns)

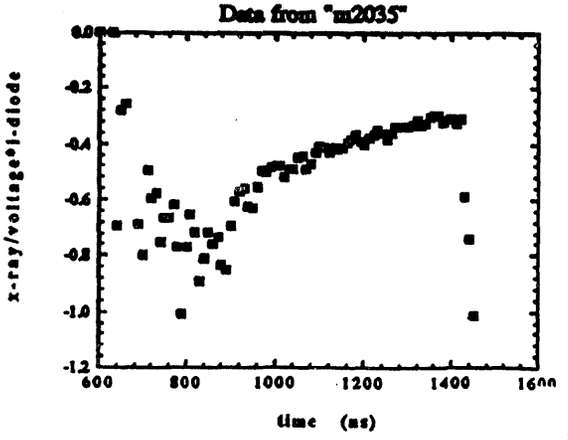
Data from "m2035"
x-ray/voltage*i-diode
time (ns)

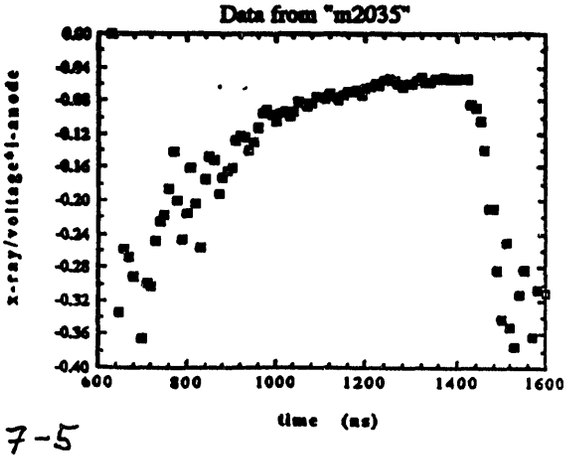
Data from "m2035"
x-ray/voltage*i-anode
time (ns)

Figure. 7-5

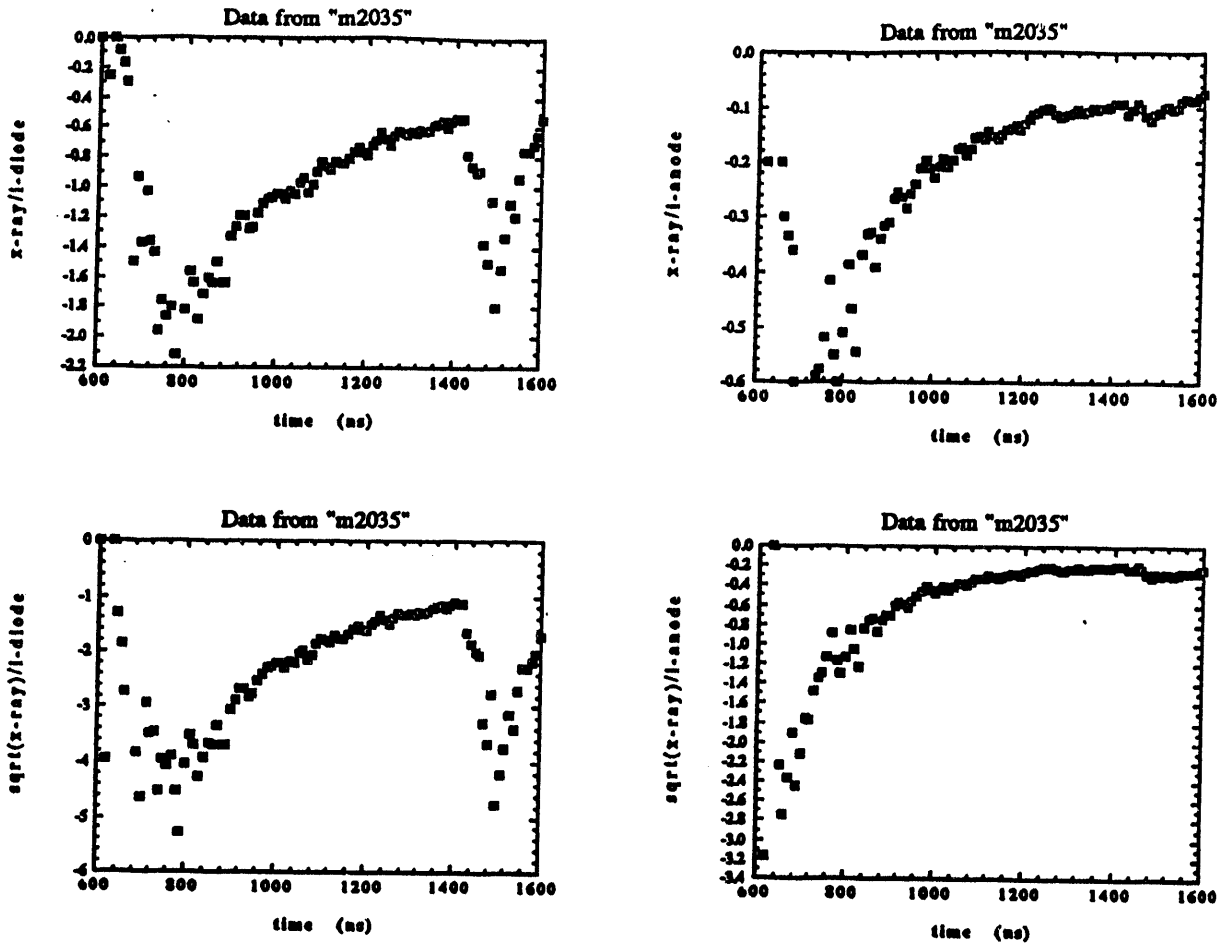

M2035 (On top of the diode covered with 3 sheets of lead)

From top to bottom on the right: (1) sqrt(x-ray) (√V), (2) x-ray signal/ voltage (V/310kV), (3) sqrt(x-ray/current(anode)) (0.38√V/kA), (4) x-ray/(voltage*current(anode)) (0.46 mV/(kV)(kA)), (5) x-ray/current (anode) (0.143V/kA), (6) sqrt(x-ray)/current(anode) (0.143√V/kA).

From top to bottom on the left: (1) voltage (kV), (2) x-ray signal (V), (3) sqrt(x-ray/current(diode)) (√0.022 V/kA), (4) x-ray/(voltage*current (diode)) (71μV/(kV)(kA)), (5) x-ray/current(diode) (0.022 V/kA), (6) sqrt(x-ray) /current(diode) (0.022√V/kA).

Figure 7-5

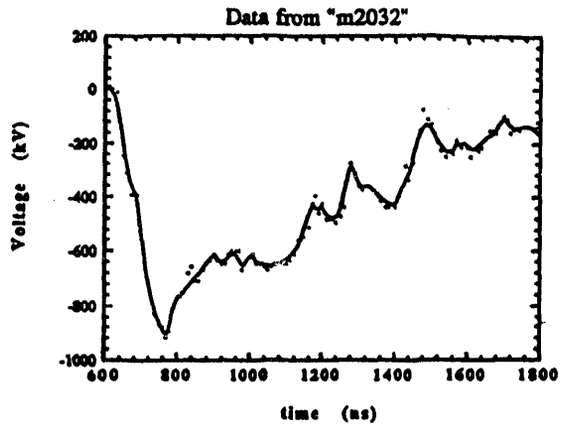
Data from "m2032"
Voltage (kV)
time (ns)

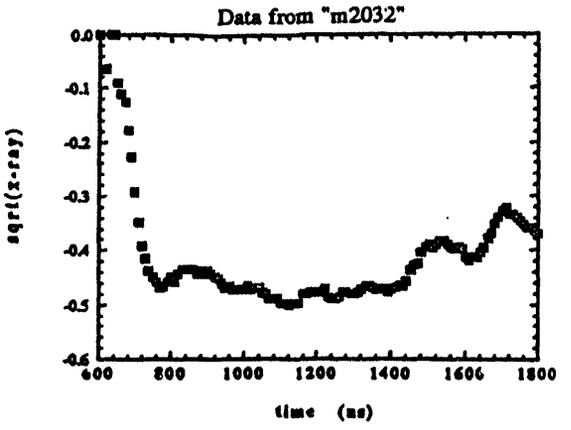
Data from "m2032"
sqrt(x-ray)
time (ns)

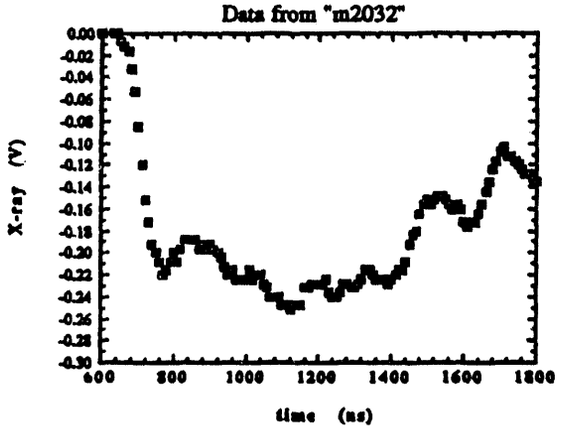
Data from "m2032"
X-ray (V)
time (ns)

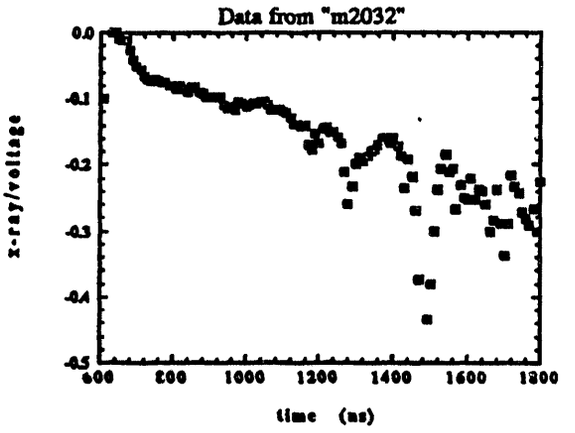
Data from "m2032"
x-ray/voltage
time (ns)

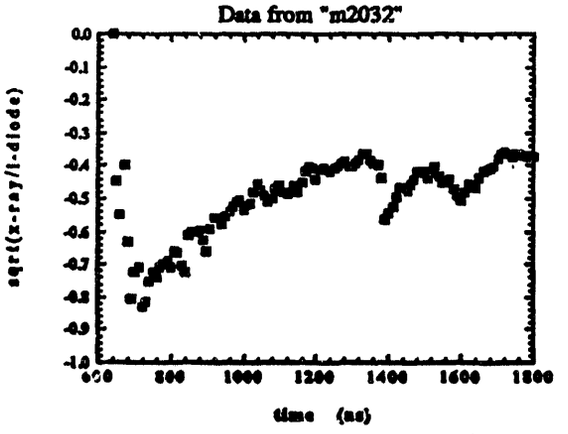
Data from "m2032"
sqrt(x-ray/i-diode)
time (ns)

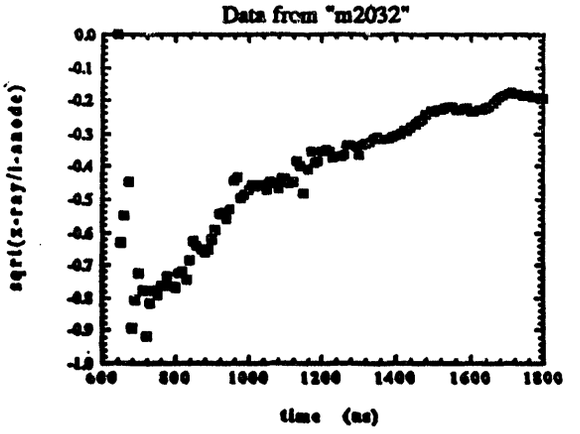
Data from "m2032"
sqrt(x-ray/i-anode)
time (ns)

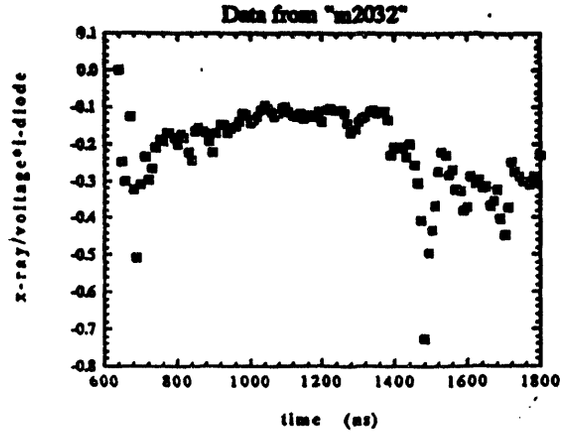
Data from "m2032"
x-ray/voltage*i-diode
time (ns)

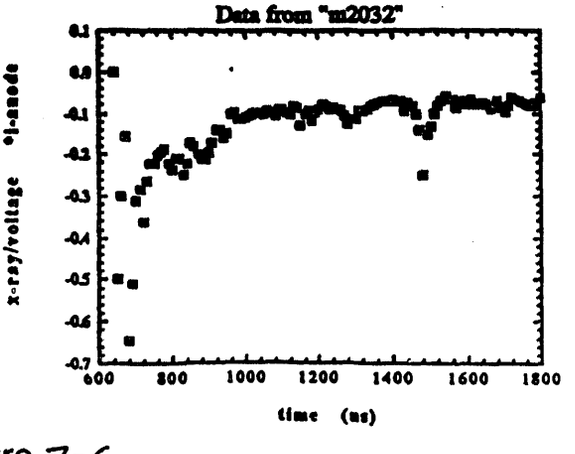
Data from "m2032"
x-ray/voltage *i-anode
time (ns)

Figure.7-6

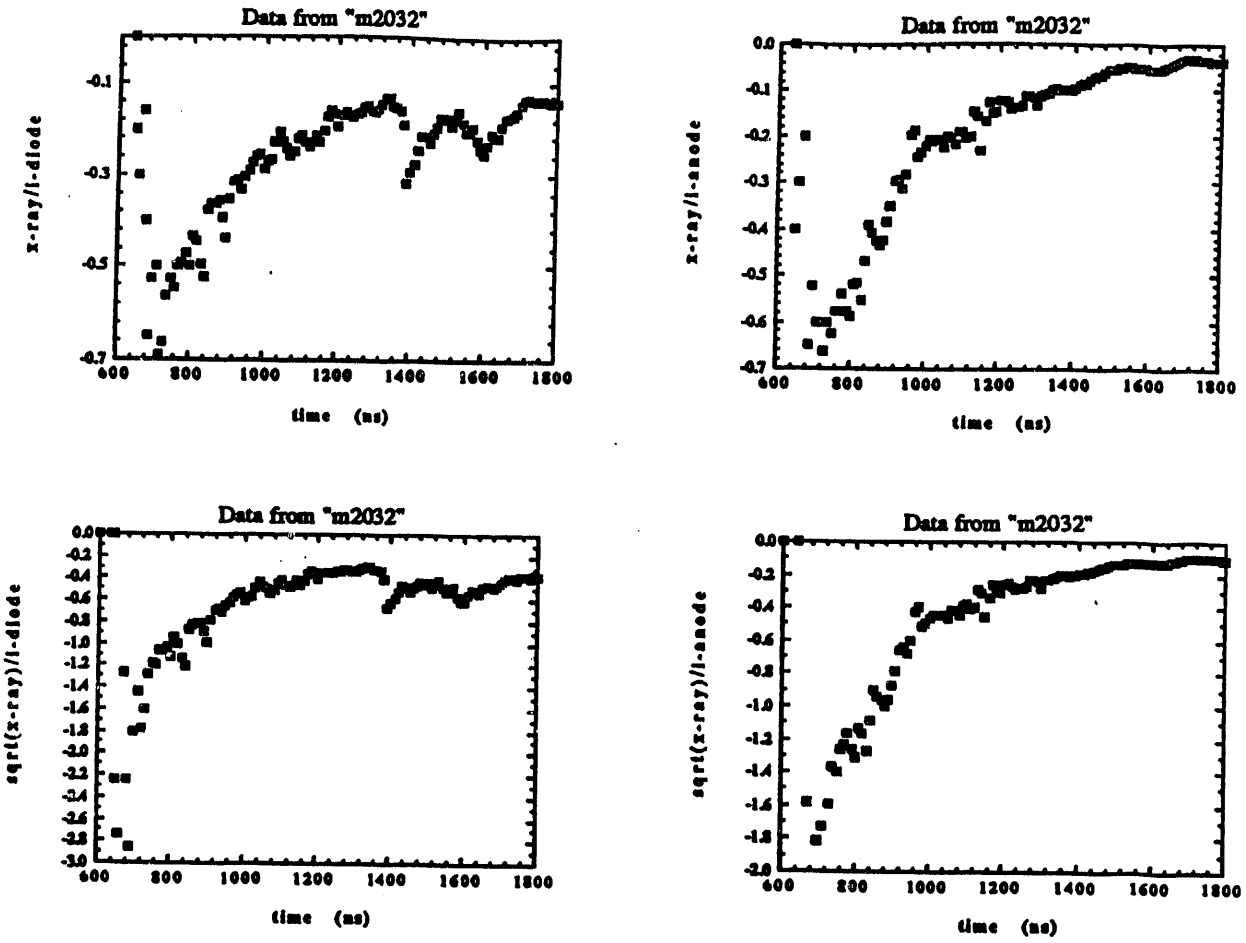

M2032 (On top of the diode covered with 3 sheets of lead)

From top to bottom on the right: (1) sqrt(x-ray) (√V), (2) x-ray signal/ voltage (V/310kV), (3) sqrt(x-ray/current(anode)) (0.38√V/kA), (4) x-ray/(voltage*current(anode)) (0.46 mV/(kV)(kA)), (5) x-ray/current (anode) (0.143V/kA), (6) sqrt(x-ray)/current(anode) (0.143√V/kA).

From top to bottom on the left: (1) voltage (kV), (2) x-ray signal (V), (3) sqrt(x-ray/current(diode)) (√0.022 V/kA), (4) x-ray/(voltage*current (diode)) (71μV/(kV)(kA)), (5) x-ray/current(diode) (0.022 V/kA), (6) sqrt(x-ray) /current(diode) (0.022√V/kA).

Figure.7-6

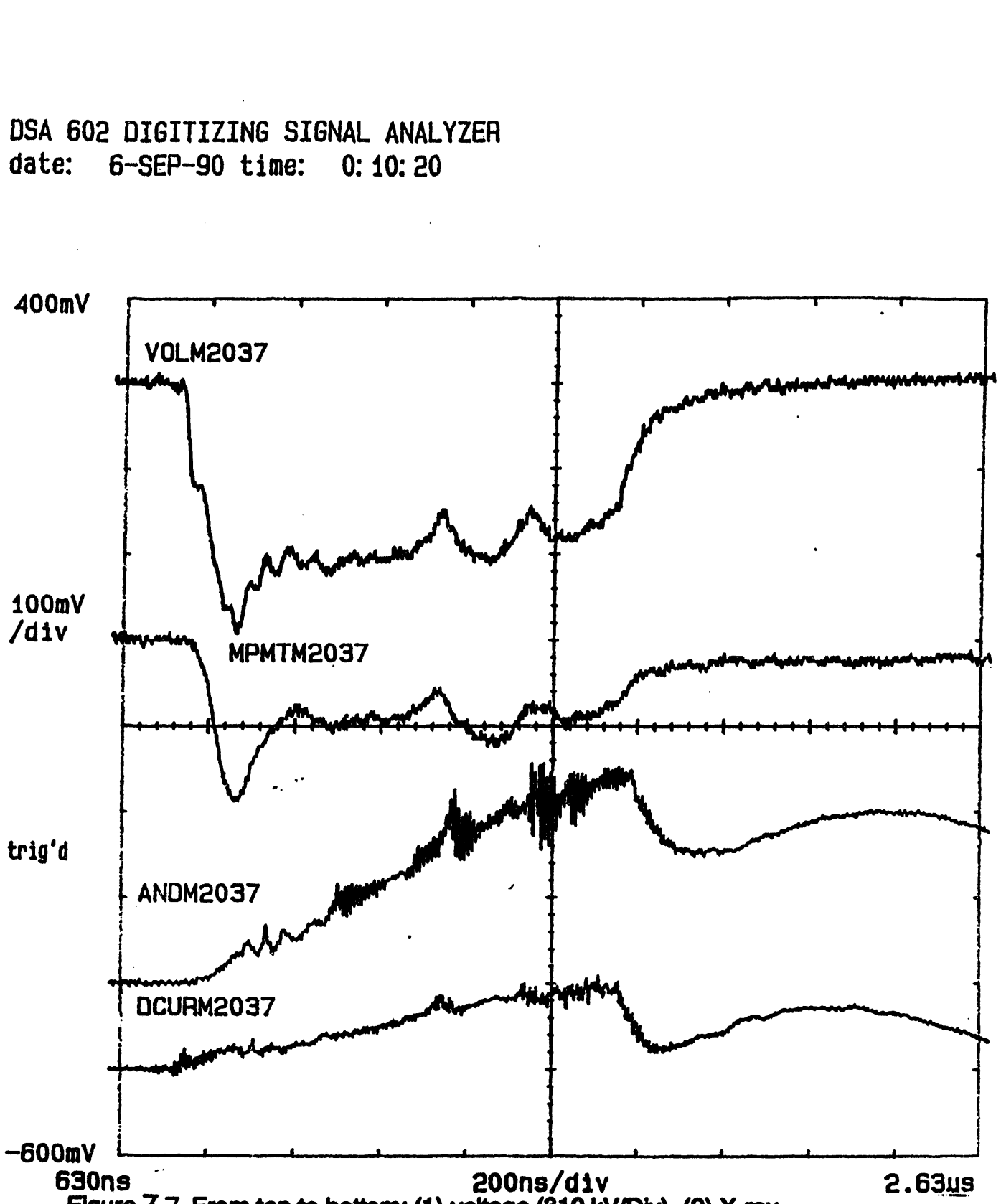

Figure ~~7-7~~ From top to bottom: (1) voltage (310 kV/Div), (2) X-ray signal (100 mV/Div) [The X-ray probe is in front of the diode region covered with 3 sheets of lead], (3) current (anode) (7 kA/Div), (4) current (diode) (22.7 kA/Div).

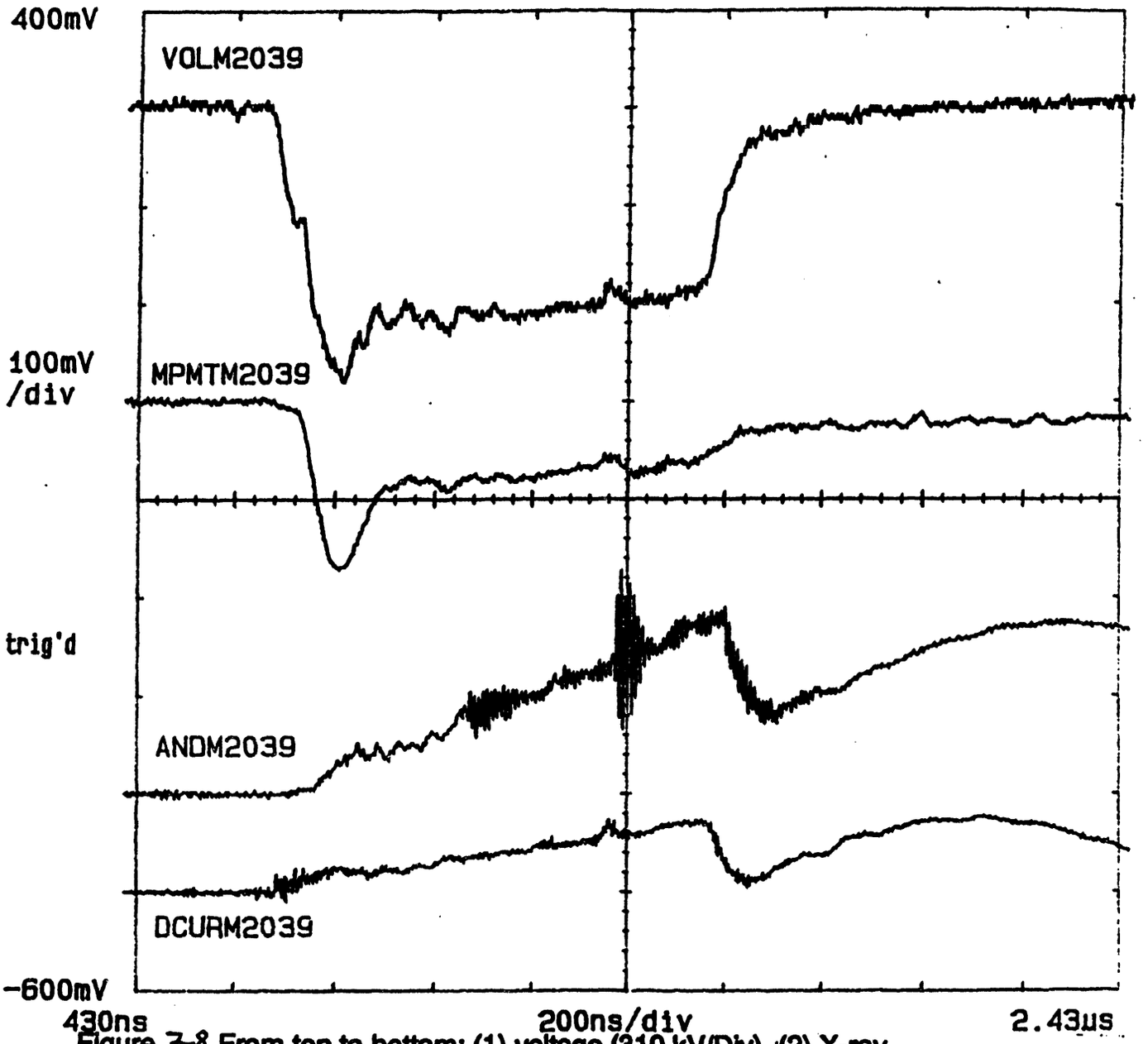

Figure. 7-8 From top to bottom: (1) voltage (310 kV/Div), (2) X-ray signal (100 mV/Div) [The X-ray probe is in front of the diode region covered with 4 sheets of lead], (3) current (anode) (7 kA/Div), (4) current (diode) (22.7 kA/Div).

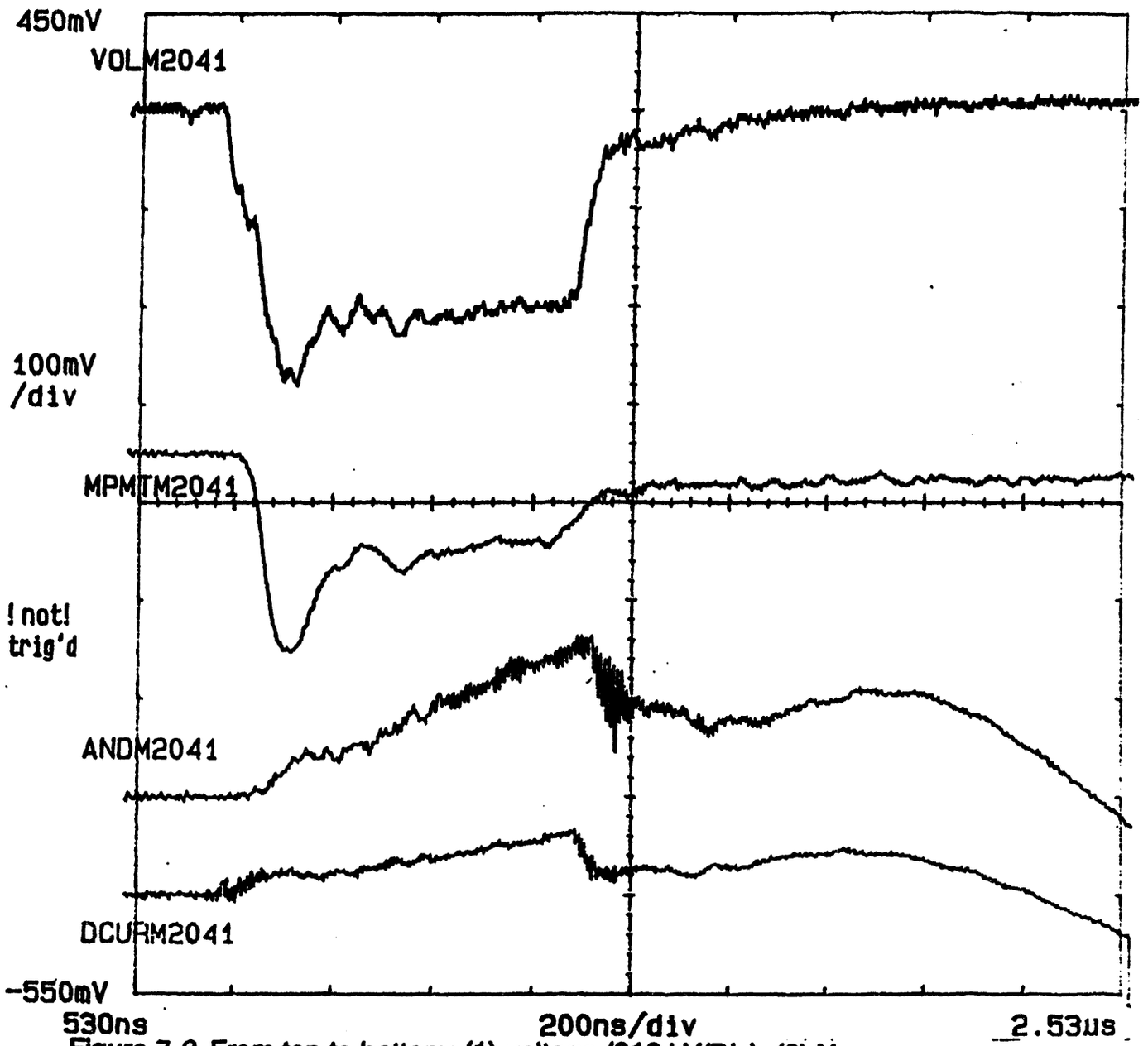

Figure 7-9 From top to bottom: (1) voltage (310 kV/Div), (2) X-ray signal (100 mV/Div) [The X-ray probe is in front of the diode region covered with 5 sheets of lead], (3) current (anode) (7 kA/Div), (4) current (diode) (22.7 kA/Div).

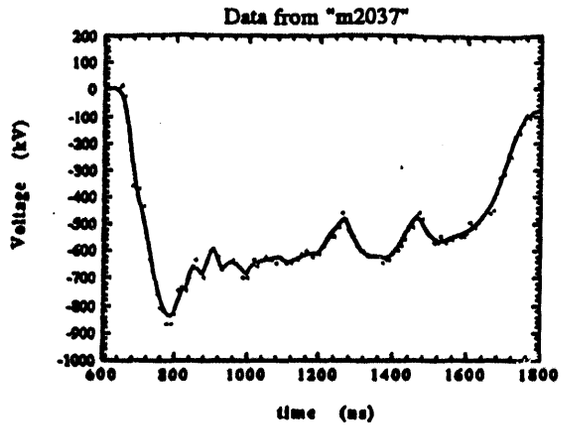
Data from "m2037"
Voltage (kV)
time (ns)

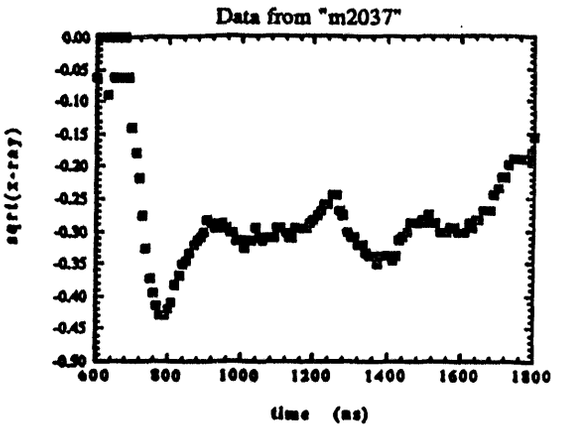
Data from "m2037"
sqrt(x-ray)
time (ns)

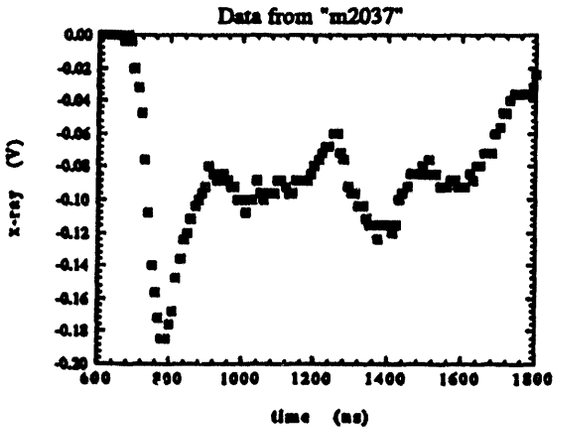
Data from "m2037"
x-ray (V)
time (ns)

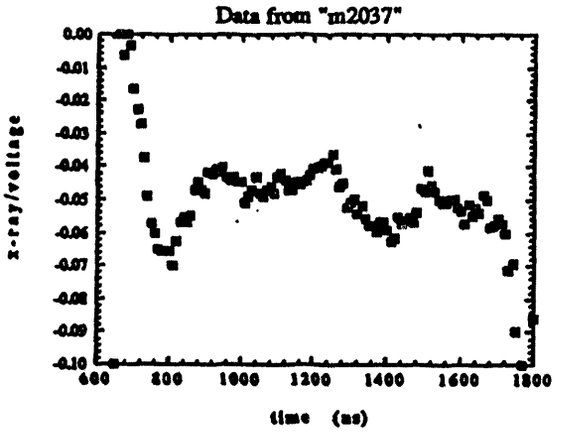
Data from "m2037"
x-ray/voltage
time (ns)

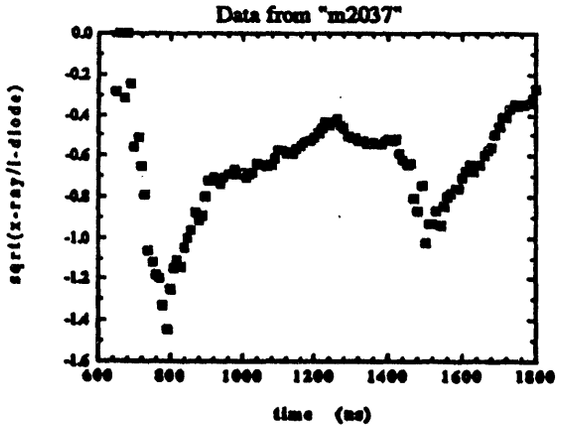
Data from "m2037"
sqrt(x-ray/i-diode)
time (ns)

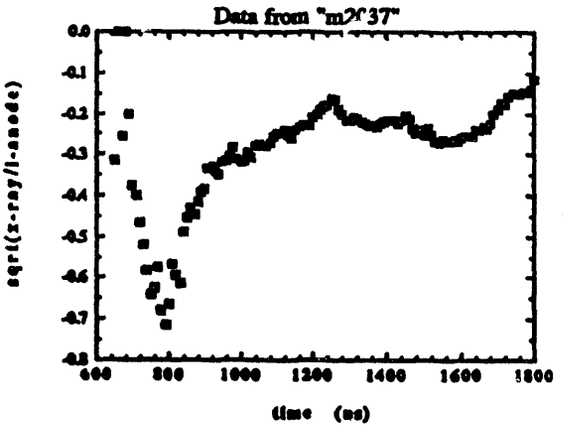
Data from "m2037"
sqrt(x-ray/i-anode)
time (ns)

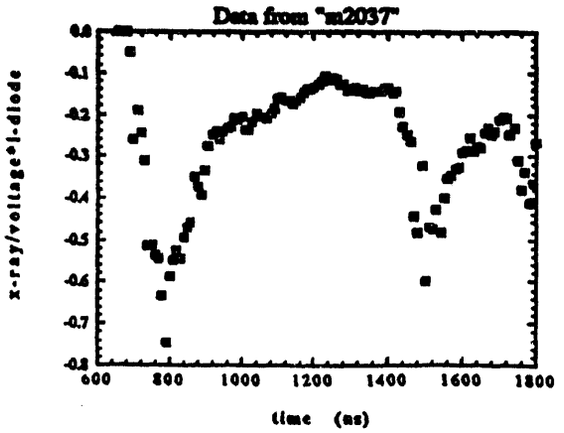
Data from "m2037"
x-ray/voltage*i-diode
time (ns)

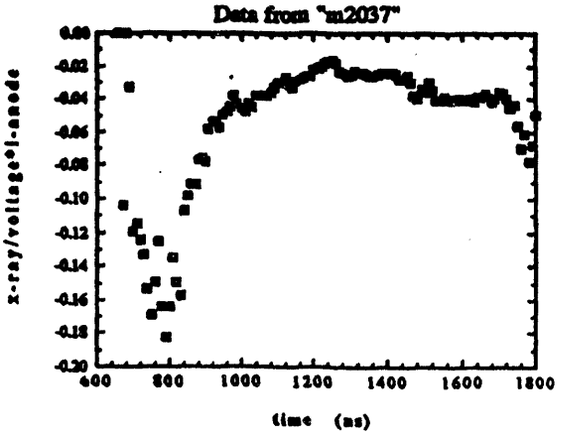
Data from "m2037"
x-ray/voltage*i-anode
time (ns)

Figure. 7-10

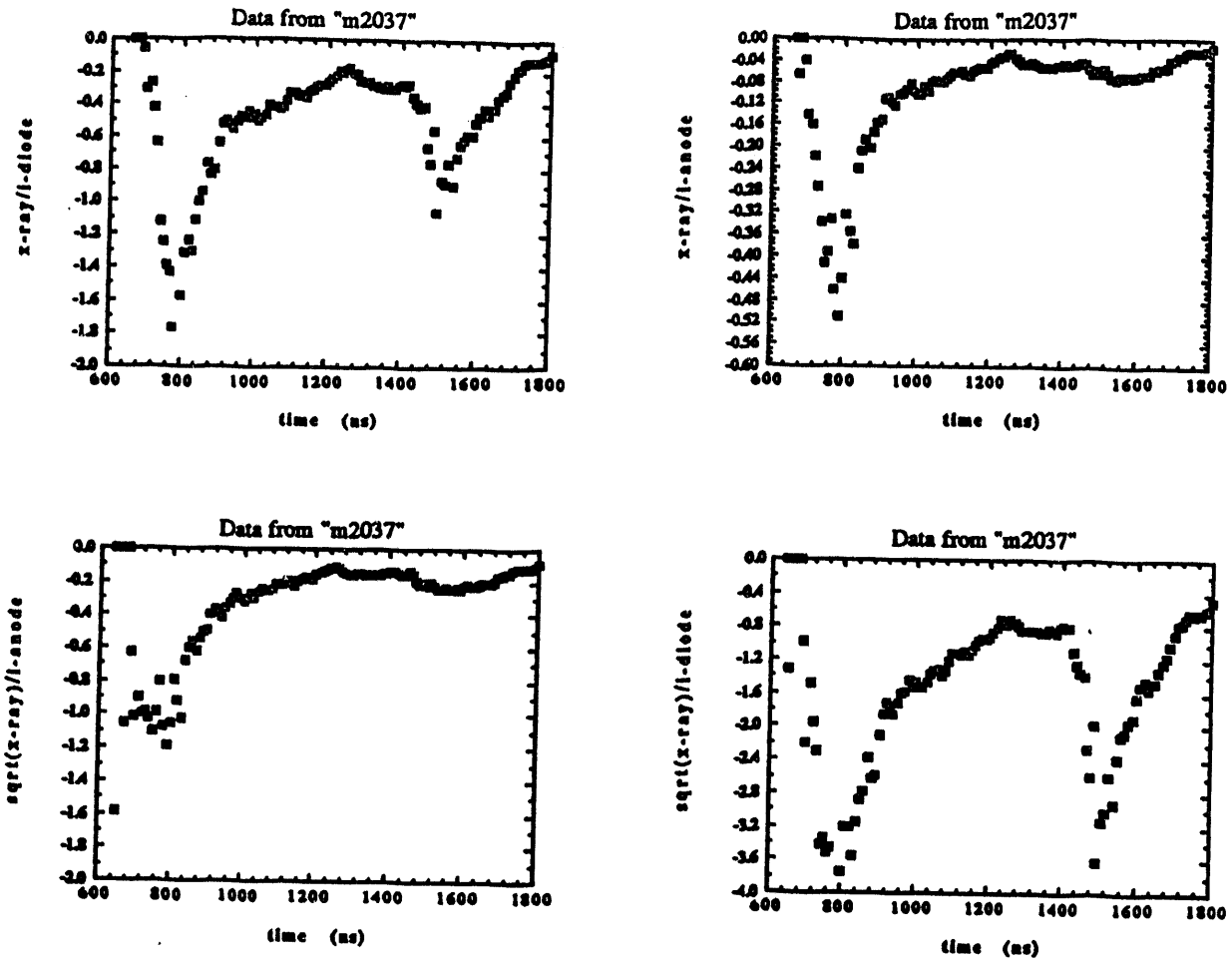

M2037 (In front of the diode covered with 3 sheets of lead)

From top to bottom on the right: (1) sqrt(x-ray) (√V), (2) x-ray signal/ voltage (V/310kV), (3) sqrt(x-ray/current(anode)) (0.38√V/kA), (4) x-ray/(voltage*current(anode)) (0.46 mV/(kV)(kA)), (5) x-ray/current (anode) (0.143V/kA), (6) sqrt(x-ray)/current(anode) (0.143√V/kA).

From top to bottom on the left: (1) voltage (kV), (2) x-ray signal (V), (3) sqrt(x-ray/current(diode)) (√0.022 V/kA), (4) x-ray/(voltage*current (diode)) (71μV/(kV)(kA)), (5) x-ray/current(diode) (0.022 V/kA), (6) sqrt(x-ray) /current(diode) (0.022√V/kA).

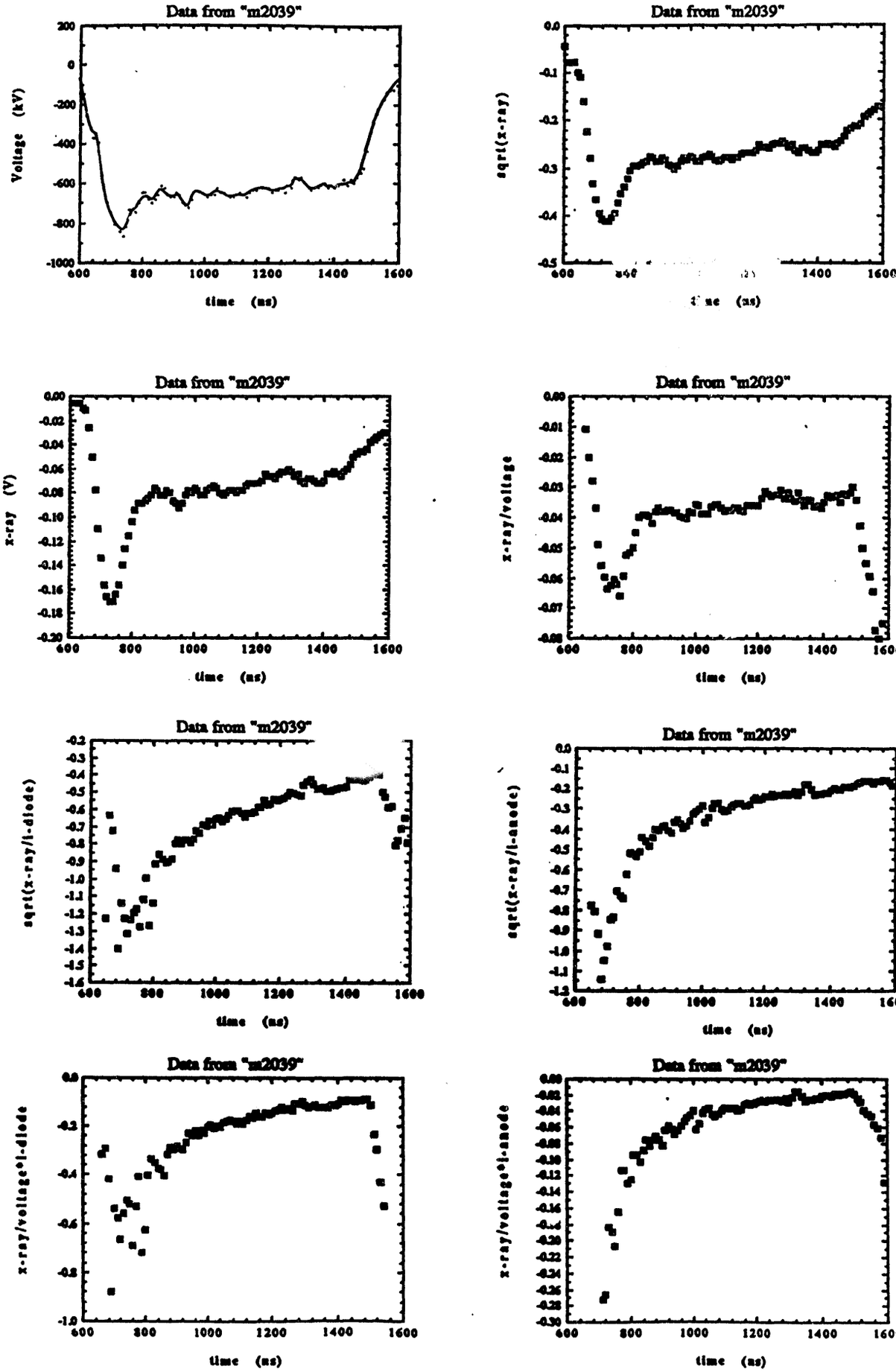
Data from "m2039"
Voltage (kV)
time (ns)
Data from "m2039"
sqrt(x-ray)
time (ns)
Data from "m2039"
x-ray (V)
time (ns)
Data from "m2039"
x-ray/voltage
time (ns)
Data from "m2039"
sqrt(x-ray/i-diode)
time (ns)
Data from "m2039"
sqrt(x-ray/i-anode)
time (ns)
Data from "m2039"
x-ray/voltage*i-diode
time (ns)
Data from "m2039"
x-ray/voltage*i-anode
time (ns)

Figure. 7-11

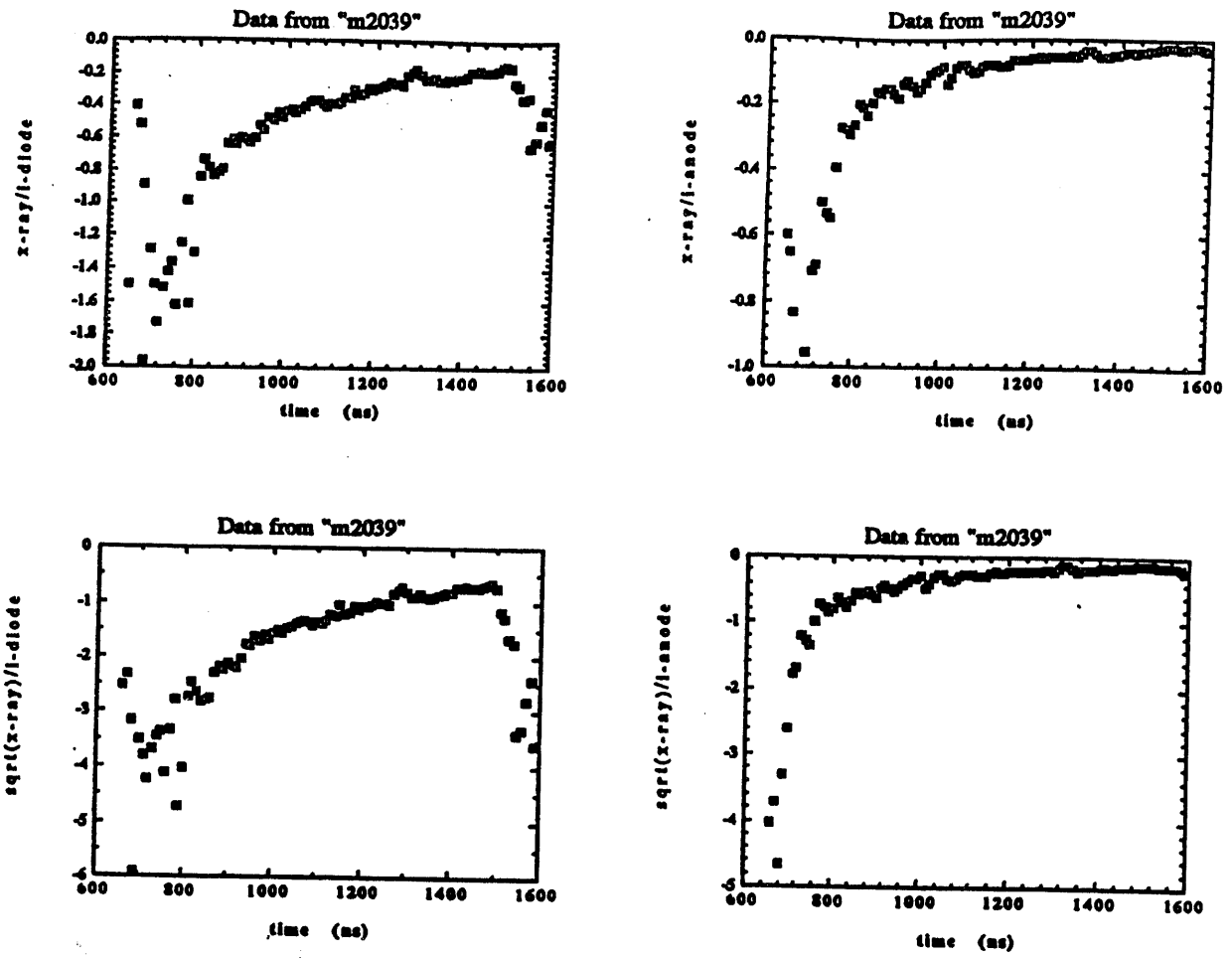

M2039 (in front of the diode covered with 4 sheets of lead)

From top to bottom on the right: (1) sqrt(x-ray) (√V), (2) x-ray signal/ voltage (V/310kV), (3) sqrt(x-ray/current(anode)) (0.38√V/kA), (4) x-ray/(voltage*current(anode)) (0.46 mV/(kV)(kA)), (5) x-ray/current (anode) (0.143V/kA), (6) sqrt(x-ray)/current(anode) (0.143√V/kA).

From top to bottom on the left: (1) voltage (kV), (2) x-ray signal (V), (3) sqrt(x-ray/current(diode)) (√0.022 V/kA), (4) x-ray/(voltage*current (diode)) (71μV/(kV)(kA)), (5) x-ray/current(diode) (0.022 V/kA), (6) sqrt(x-ray) /current(diode) (0.022√V/kA).

Figure.7-11

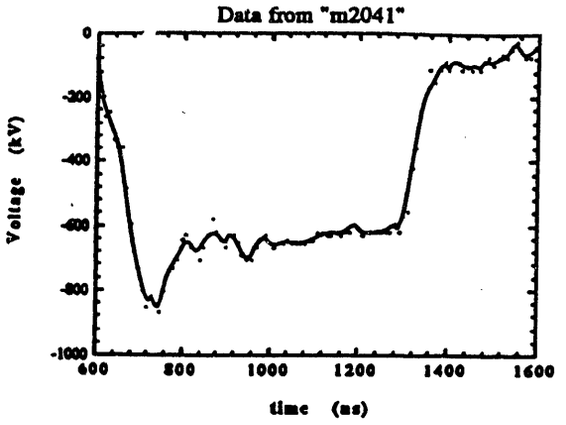
Data from "m2041"
Voltage (kV)
time (ns)

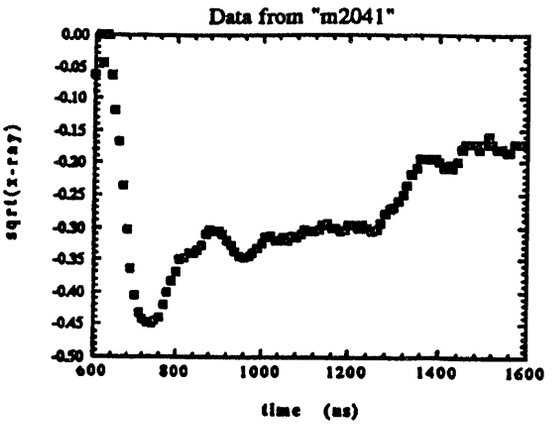
Data from "m2041"
sqrt(x-ray)
time (ns)

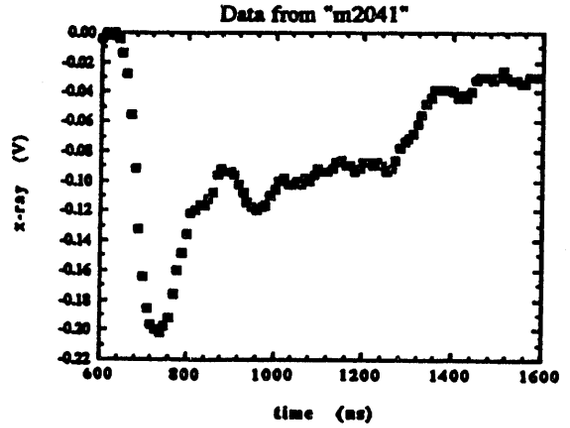
Data from "m2041"
x-ray (V)
time (ns)

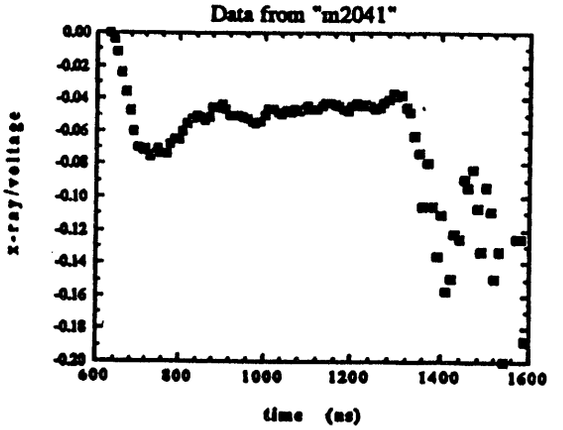
Data from "m2041"
x-ray/voltage
time (ns)

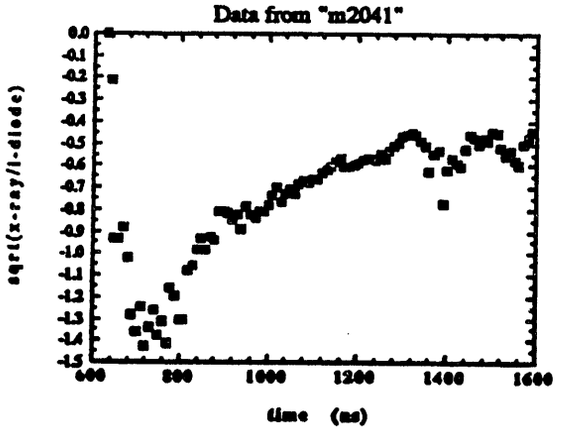
Data from "m2041"
sqrt(x-ray/i-diode)
time (ns)

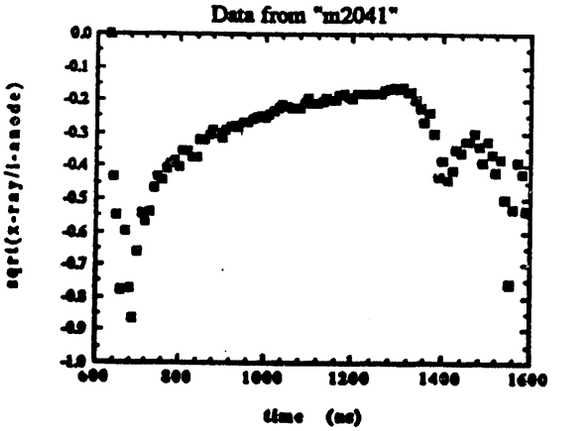
Data from "m2041"
sqrt(x-ray/i-anode)
time (ns)

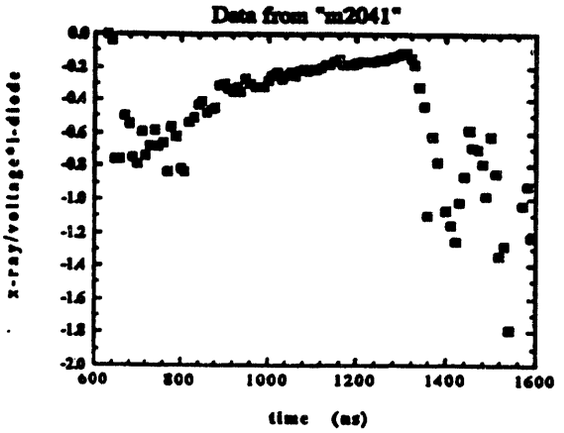
Data from "m2041"
x-ray/voltage*i-diode
time (ns)

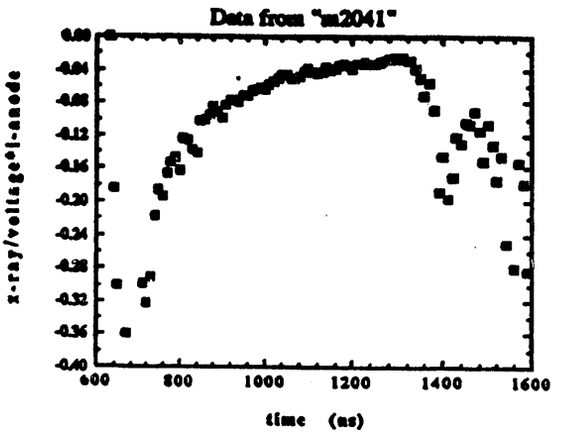
Data from "m2041"
x-ray/voltage*i-anode
time (ns)

Figure. 7-12

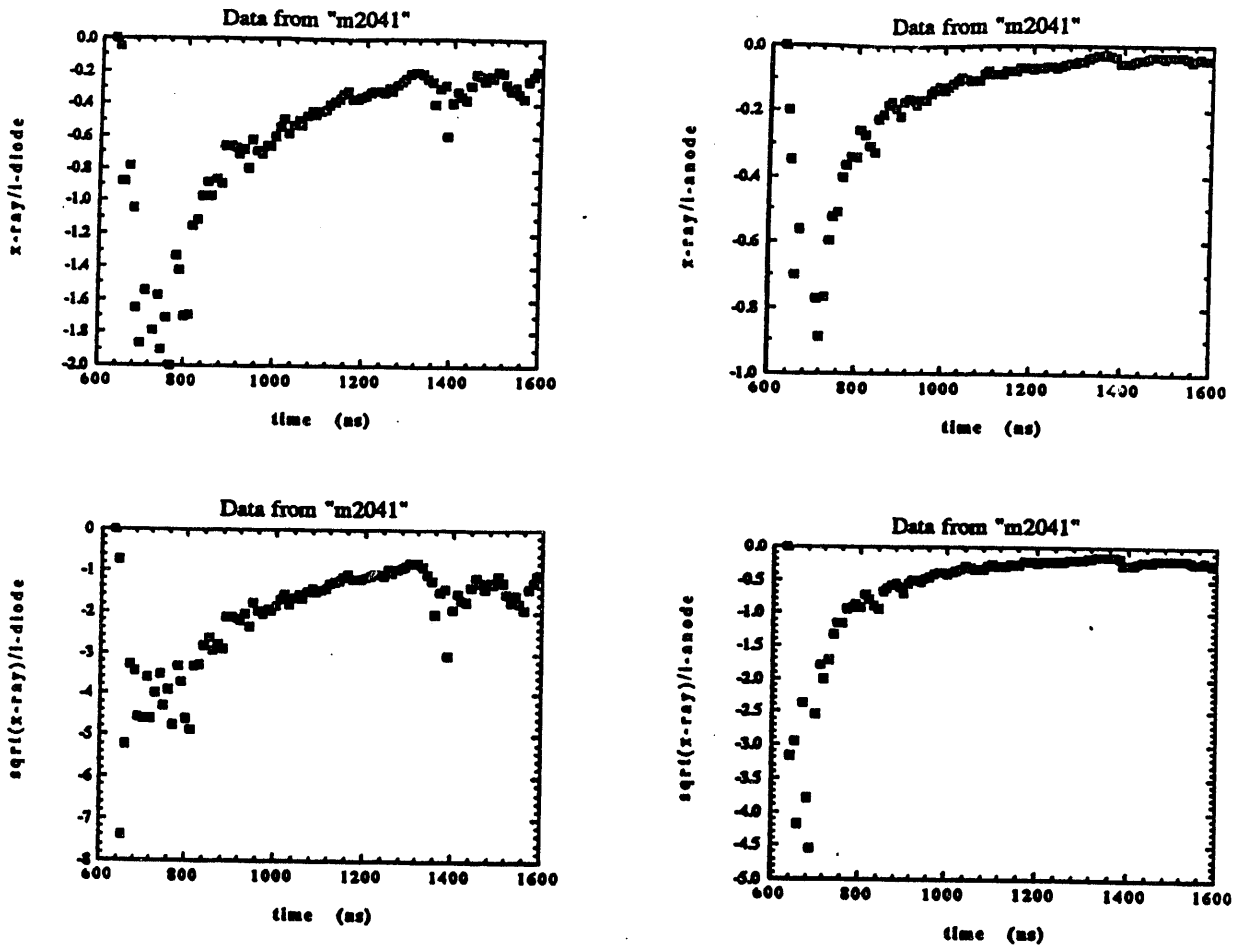

M2041 (In front of the diode covered with 5 sheets of lead)

From top to bottom on the right: (1) sqrt(x-ray) (√V), (2) x-ray signal/ voltage (V/310kV), (3) sqrt(x-ray/current(anode)) (0.38√V/kA), (4) x-ray/(voltage*current(anode)) (0.46 mV/(kV)(kA)), (5) x-ray/current (anode) (0.143V/kA), (6) sqrt(x-ray)/current(anode) (0.143√V/kA).

From top to bottom on the left: (1) voltage (kV), (2) x-ray signal (V), (3) sqrt(x-ray/current(diode)) (√0.022 V/kA), (4) x-ray/(voltage*current (diode)) (71μV/(kV)(kA)), (5) x-ray/current(diode) (0.022 V/kA), (6) sqrt(x-ray) /current(diode) (0.022√V/kA).

Figure. 7-12

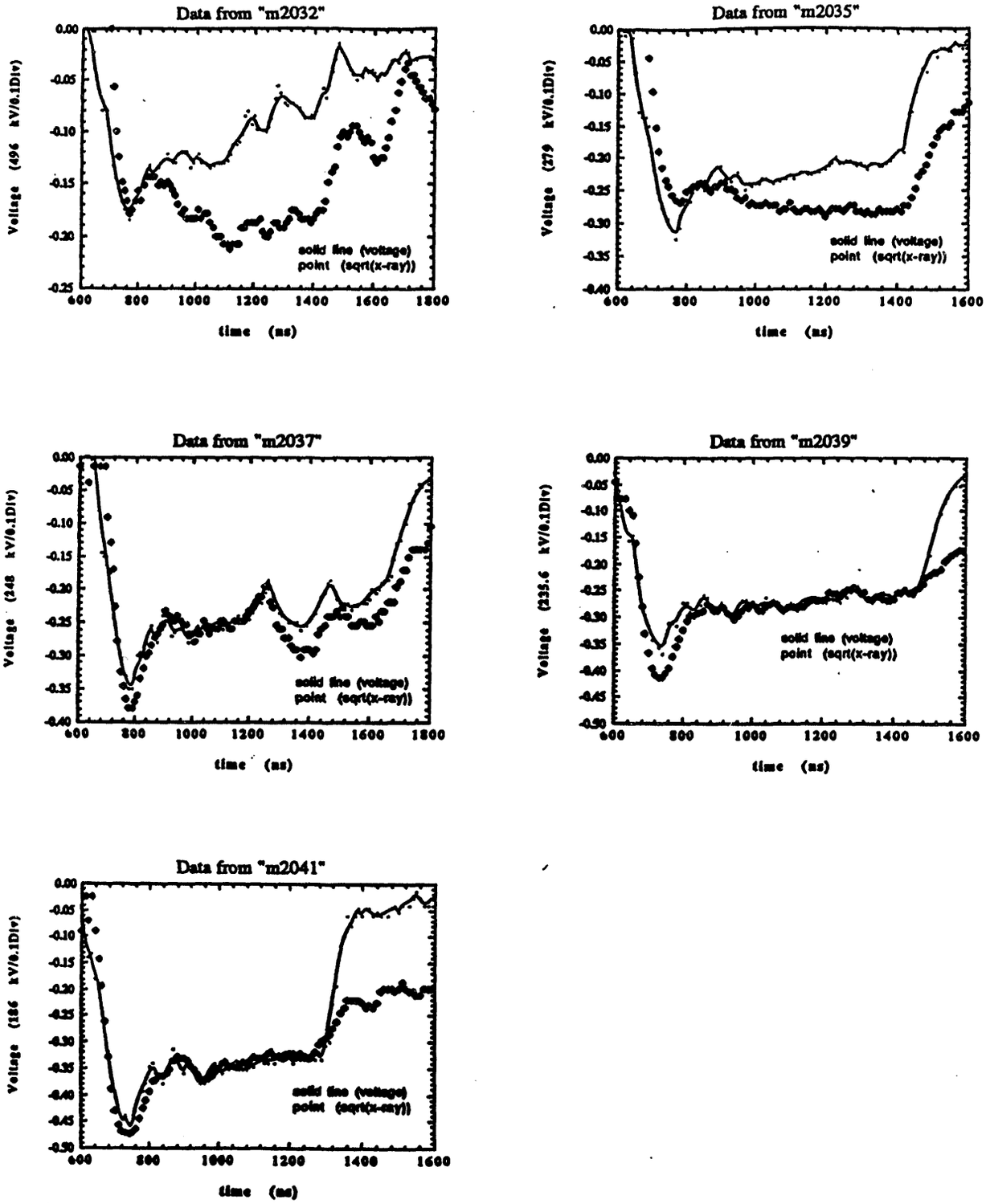

Comparison of voltage and sqrt(x-ray) at different x-ray probe conditions. From top to bottom on the left: (1) m2032 (top of the diode covered with 3 sheets of lead), (2) m2037 (in front of the diode covered with 3 sheets of lead), (3) m2041 (in front of diode covered with 5 sheets of lead). From top to bottom on the right: (1) m2035 (top of the diode covered with 3 sheets of lead), (2) m2039 (in front of diode covered with 4 sheets of lead).

Figure. 7-13

Average Electric Stress vs. Arcing Time

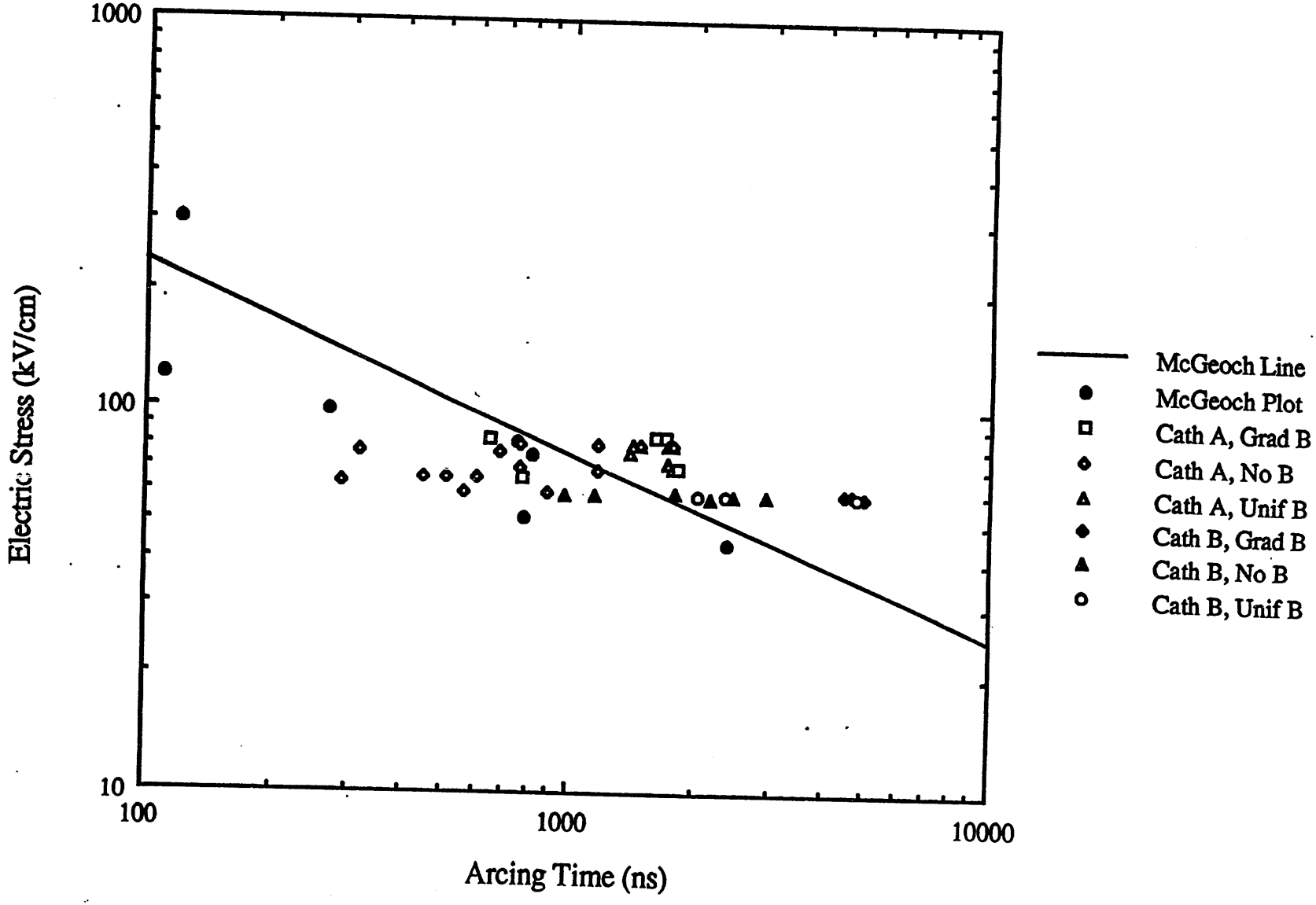

Figure 8-1

Average Electric Field vs. Shorting Time

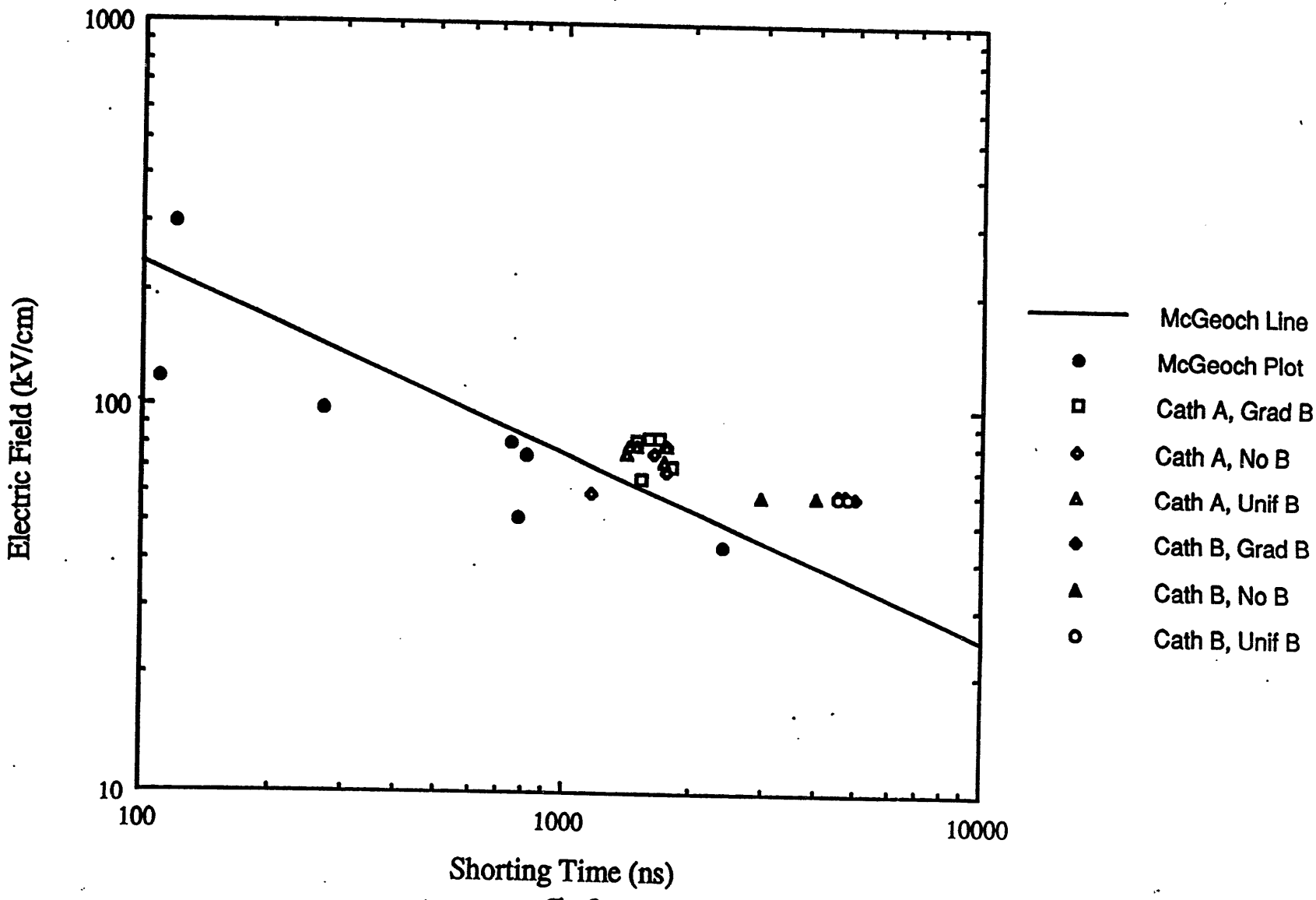

Figure 8-2

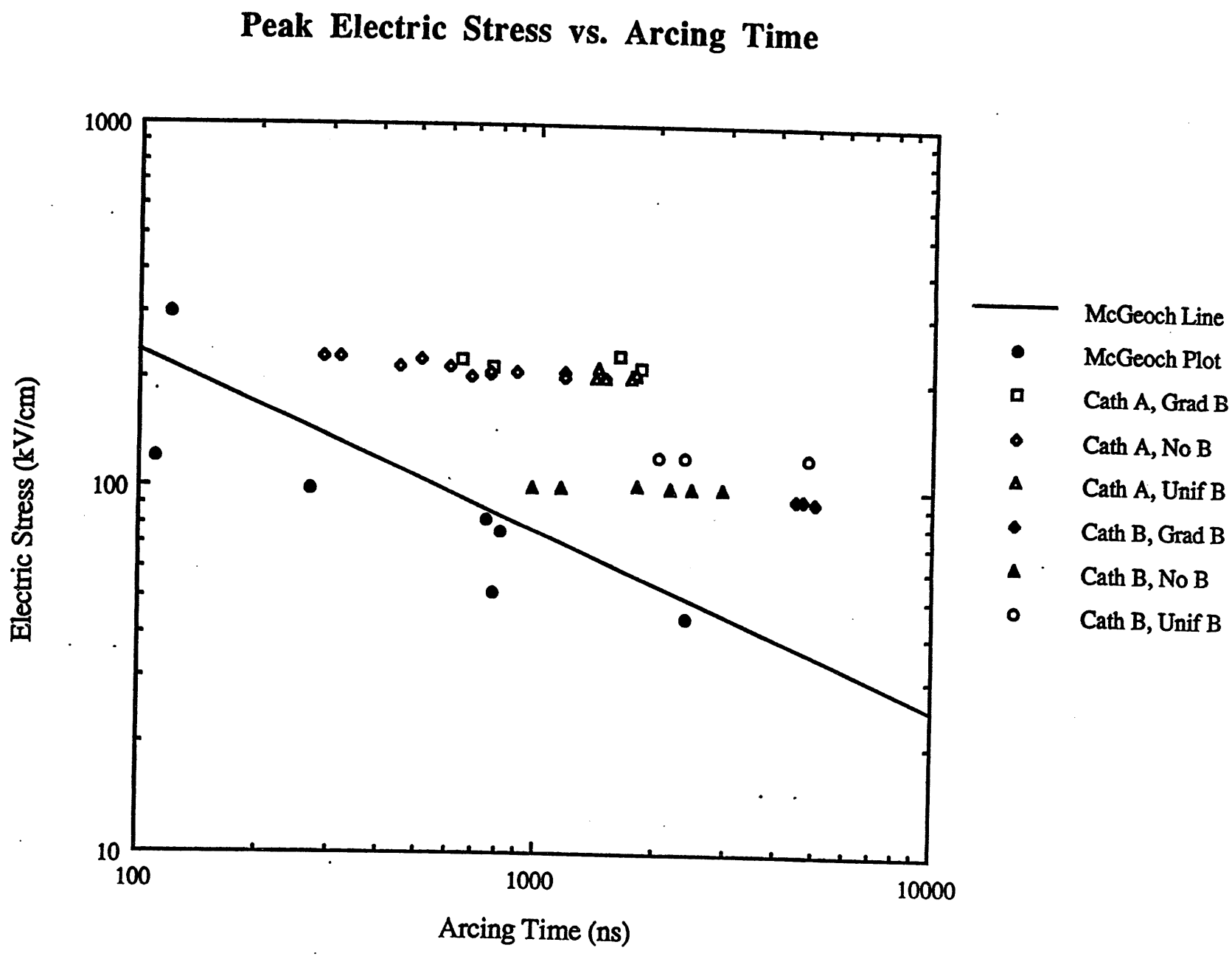
Peak Electric Stress vs. Arcing Time
1000
100
10
Electric Stress (kV/cm)
100
1000
10000
Arcing Time (ns)
McGeoch Line
McGeoch Plot
Cath A, Grad B
Cath A, No B
Cath A, Unif B
Cath B, Grad B
Cath B, No B
Cath B, Unif B

Figure 8-3

Peak Electric Stress vs. Shorting Time

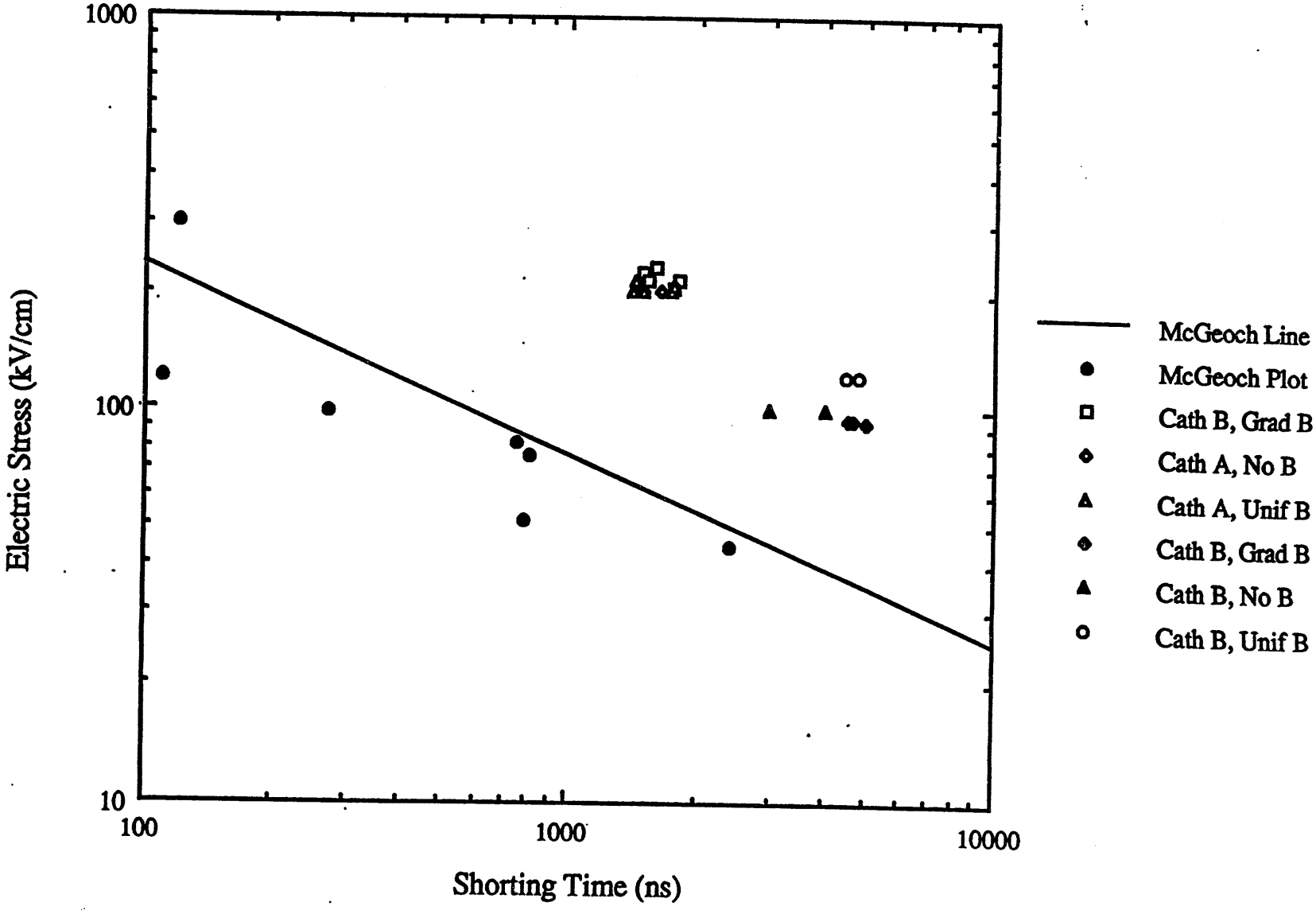

Figure 8-4

Appendix B. Personnel Involved in This Project

Principal Investigator: Professor Ronald M. Gilgenbach
(received LANL support)

Graduate students involved:
H. Ching (received LANL support)
J.J. Choi
P. Menge (received LANL support)
T.A. Spencer
P.L.G. Ventzek (received LANL support)

Senior Research Associate:
Dr. R. A. Bosch (received LANL support)

reprint + preprint removed. ds

END

DATE
FILMED
3/8/94